ALBERT-LUDWIGS-UNIVERSITÄT FREIBURG

First-principles investigation of hydrogen interaction with metals

by

DAVIDE DI STEFANO

Submitted to the Faculty of Mathematics and Physics
of the Albert-Ludwigs-Universität
Freiburg im Breisgau
in partial fulfillment of the requirements
for the degree of a
Doctor rerum naturalium

Dekan: Prof. Dr. Kröner
Erstgutacher: Prof. Dr. Elsässer
Zweitgutacher: Prof. Dr. Reiter
Datum der mündlichen Prüfung: 29.01.2016

For Emilia.
You will always be my source of pride.

Erklärung

Hiermit erkläre ich Folgendes:

1. Die vorliegende Arbeit wurde selbstständig und ohne die unzulässige Hilfe Dritter verfasst. Insbesondere habe ich hierfür nicht die entgeltliche Hilfe von Vermitlungs- beziehungsweise Beratungsdiensten (Promotionsberater/ -beraterinnen oder anderer Personen) in Anspruch genommen.

2. Es wurden keine anderen als die angegebenen Quellen und Hilfsmittel benutzt. Wenn immer Teile der hier dargestellten Ergebnisse durch die Mitarbeit anderer Personen entstanden sind, wird dies entsprechend gekennzeichnet.

3. Die Arbeit wurde bisher weder im In- noch im Ausland in gleicher oder ähnlicher Form einer Prüfungsbehörde vorgelegt.

4. Die Bestimmungen der Promotionsordnung der Universität Freiburg für die Fakultät für Mathematik und Physik sind mir bekannt; insbesondere weiß ich, dass ich vor der Aushändigung der Doktorurkunde zur Führung des Doktorgrades nicht berechtigt bin.

Freiburg, 02/12/2015

. . . .
(Davide Di Stefano)

Abstract

The presence of hydrogen (H) in metals has a deleterious effect on their mechanical properties. This phenomenon is called hydrogen embrittlement (HE). Since, the susceptibility of a metal to HE is strongly dependent on the rate and mode at which H can accumulate at a location of embrittlement, the transport of H is a critical aspect of HE.

This thesis aims to advance the understanding of H trapping and diffusion in the microstructure of materials by means of first-principles methods. As first step, we considered the diffusion of H in bulk metals. The diffusion coefficients of interstitial hydrogen in bulk Fe and Ni crystals have been calculated over a wide range of temperatures. Quantum-mechanical effects have been included using the semi-classical transition state theory (SC-TST) and the small-polaron model of Flynn and Stoneham. Our results show that it is crucial to include such effects for a quantitative simulation of diffusion of H in bcc Fe even at room temperature, while in case of H in fcc Ni this is less important.

Then we investigated the interaction of H interstitial with Ni grain boundaries and with TiC precipitates in Fe. In the former case two distinct types of GBs have been considered: the $\Sigma3(111)[\bar{1}10]$ with a close-packed atomic interface structure and the $\Sigma5(210)[001]$ with a less dense structure consisting of open structural units of atoms. Our calculations reveal that these two GBs have markedly different interaction behaviors with interstitial hydrogen atoms. The close-packed $\Sigma3$ GB neither traps H nor enhances its diffusion, but instead acts as a two-dimensional diffusion barrier. In contrast, the $\Sigma5$ GB provides numerous trapping sites for H within its open structural units as well as easy pathways for H migration along the GB plane that enhance the H diffusivity by about two orders of magnitude wot respect to bulk Ni. Additionally the maximum amount of H which can accumulate at the $\Sigma5$ GB at finite temperature has been estimated by coupling density functional theory results with the Langmuir-McLean model. Finally we investigated the effects of H on the cohesion of the $\Sigma5$ GB and observed two distinct effects. On one side the H lower the Ni-Ni bonds, but on the other side H forms H-Ni bonds which strengthen the GB cohesion.

In case of H interacting with a TiC precipitate in Fe we investigated the energetics associated with the trapping of H at various interfaces as well as at C vacancies inside the TiC particles. Our results show that the interfaces offer moderately strong traps. The C vacancies provide strong traps, but their population is possible at high temperatures only.

For all the cases studied, our results provide valuable insights into the understanding of H transport in metals and therefore into HE.

Zusammenfassung

Wasserstoff (H) in Metallen führt zu einer Beeinträchtigung von deren mechanischen Eigenschaften. Dieses Phänomen wird als Wasserstoffversprödung (HE) bezeichnet. Da die Anfälligkeit des Metalls auf HE stark von der Art abhängt, wie sich H am Ort einer Verspödung anlagert, spielt der H-Transport eine entscheidende Rolle.

Diese Arbeit zielt darauf, das Einfangen von H und dessen Diffusion im Gefüge von Materialien mithilfe von *first-principles*-Methoden besser zu verstehen. Als erstes betrachten wir die Diffusion von H im Inneren von Metall-Einkristallen. Die Diffusionskoeffizienten von interstitiellem H in Fe- und Ni-Kristallen wurden für einen großen Temperaturbereich berechnet. Dabei wurden quantenmechanische Effekte mit der semiklassischen *transition-state*-Theorie (SC-TST) und dem *small-polaron*-Modell von Flynn und Stoneham berücksichtigt. Unsere Ergebnisse zeigen, dass solche Effekte entscheidend sind, um die Diffusion von H in krz-Fe bei Raumtemperatur quantitativ zu berechnen, wohingegen sie für kfz-Ni keine große Rolle spielen.

Dann betrachteten wir die Wechselwirkung von H mit Ni-Korngrenzen (KG) und mit TiC-Ausscheidungen im Fe. Im ersten Fall, wurden zwei verschiedene Typen von KG betrachtet, die $\Sigma3(111)[\bar{1}10]$, welche eine dichtgepackte Grenzfläche besitzt, und die $\Sigma5(210)[001]$, deren Grenflächen aus offenen Struktureinheiten besteht. Unsere Ergebnisse zeigen, dass diese zwei KG ein signifikant unterschiedliches Verhalten mit interstitiellen H-Atomen zeigen. Die dichtgepackte $\Sigma3$ KG fängt H weder ein, noch erhöht sie dessen Diffusion. Stattdessen wirkt sie als zwei-dimensionale Diffusionsbarriere. Im Vergleich dazu besitzt die $\Sigma5$ KG eine Vielzahl von offenen Struktureinheiten, in denen H eingefangen werden kann. Diese Struktureinheiten enthalten günstige Migrationspfade für H-Atome entlang der KG, wodurch sich die H-Diffusion um bis zu zwei Größenordnungen im Vergleich zum Ni-Einkristall erhöhen kann. Zusätzlich wurde die maximale Menge von H an der $\Sigma5$ KG bei endlichen Temperaturen bestimmt, indem Ergebnisse der Dichtefunktional-Theorie mit dem Langmuir-McLean-Modell konbiniert wurden. Schließlich haben wir die Effekte von atomaren H auf die Kohäsion der $\Sigma5$ KG untersucht und dabei zwei verschiedene Effekte beobachtet. H führt sowohl zu einer Schwächung von Ni-Ni-Bindungen als auch zur Bildung von H-Ni-Bindungen, welche die Ni-Körner zusammen halten.

Für den Fall der Wechselwirkung von H mit TiC-Ausscheidungen in Fe haben wir die Energetik untersucht, wie H an den verschiedenen Grenzflächen und an C-Leerstellen innerhalb der TiC-Teilchen eingefangen wird. Unsere Ergebnisse zeigen, dass die Grenzflächen nur mäßig starke Fallen darstellen, wohingegen C-Leerstellen als starke Fallen wirken. Jedoch ist das dortige Einfangen von H nur bei hohen Temperaturen möglich.

In allen untersuchten Fällen tragen unsere Resultate zu einem besseren Verständnis vom H-Transport in Metallen und damit auch der HE bei.

Acknowledgments

Firstly, I would like to express my gratitude to my advisor Prof. Christian El-sässer for the continuous support during my PhD study and related research, patience, motivation, and for having always tried to share with me his vast knowledge.

On a par with my advisor, I would like to thank Dr. Matous Mrovec for all the time he has dedicated to me and the numerous discussions, comments, suggestions which have been essential for my studies.

The financial support by the European Union under the Seventh Framework Programme is gratefully acknowledged. I want also to express my gratitude to all the members of the MultiHy project for their contributions in creating such a stimulating research program.

It is a great pleasure to thank all colleagues and friends I met here at Fraunhofer IWM for having provided me with a great atmosphere in which to work, and often have fun. The list includes Benedikt (with whom I am in debt for the careful proofreading of this thesis), Sabine, Francesco, Natalia, Matous, Giulio, Gian, Georg, Wolfgang, Nedko, Jamel, Anke, Daniel, Dariush, Nick, Rahul, and all the present and past inhabitants of the M8.

A sincere thank goes to my oldest and best friends Juan (thanks also for not having missed any chance to visit me here), Mirco, Luca, Gian Marco, and Pietro for their special support and for making me feel at home each time I was back in Rome.

Un grande ringraziamento va alla mia famiglia. Ai miei genitori, Antonio e Rina, per aver sempre creduto in me e per i sacrifici fatti per permettermi di arrivare dove sono. Ai miei fratelli Paolo e Andrea per il loro supporto e pazienza. Я так же выражаю благодарность своей белорусской семье, Игорю, Наталье, Галине, Кириллу, Маше и Камилле, за их поддержку и за то, что они мне показали, что не всегда обязательно говорить на том же языке, чтобы понимать друг друга.

Finally I would like to thanks my wife Irina for her unconditional love and support, for her patient, and for looking after our wonderful daughter, Emilia, to whom this thesis is dedicated.

Contents

Chapter 1

Introduction

The study of hydrogen is currently attracting much interest [1–4] in the perspective of the so-called hydrogen economy. Hydrogen fuel has always been seen as a promising alternative to fossil fuels because it burns cleanly and in principle it has no negative impact on the environment. However on the route to the hydrogen economy there are several obstacles and challenges in each involved functional area, namely production, distribution, storage, and use of hydrogen. For instance in production the main issue is that most of the hydrogen currently produced for industrial uses (about 95%) comes from steam reforming of fossil fuels [5]. This method is the cheapest, but it has the disadvantage of producing also CO_2 which in most cases is released into the atmosphere. For the distribution, storage, and use the main issue is that H has a very low mass density and therefore a very low energy density. Indeed there is more hydrogen in a liter of gasoline (116 grams) than in a liter of pure liquid hydrogen (71 grams). The solutions to these problems are strongly related to material science [6–8]. For instance the production of H by water splitting appears to become a promising alternative to those consuming fossil fuels. But the possible processes (electrochemical or photochemical reactions) require relatively cheap materials, in order to keep the costs low, having very specific properties, such as the ability to work in extreme conditions, biocompatibility, long outdoor lifetime, etc.

Another important problem that material science must solve is that H can be absorbed into metals and may cause a degradation of their mechanical properties. This phenomenon is called hydrogen embrittlement (HE). For instance, HE is actually one of the main problems for distribution and storage of H. One of the most

efficient ways to transport H is to use steel pipelines. Although this is done successfully in the gas and petroleum industries since long time, for the hydrogen economy a higher H pressure in the pipelines is required which increases the risk of HE [9]. It is important to notice that HE does not concern just applications directly related to the hydrogen economy. It is a serious general issue for metallic materials used in structural applications. Most of these structural materials are susceptible to HE to some extent and the susceptibility usually increases with the mechanical strength of the material. Therefore, this phenomenon is critical in all industrial sectors where high-strength materials are used (for instance the nuclear-power, oil and gas, aerospace, and automobile industries [10, 11]) One example out of many is the manufacturing of steel. Today the susceptibility to HE limits the use of high strength steels to those with a tensile strength lower than 1000 MPa. The use of steels with higher strength across all industrial sectors can lead to a CO_2 reduction of at least 74 megatons per year, according to a study of the Boston Consulting Group in 2007 [12]. The main reason is due to the weight reduction. For instance, about 11 megatons of the potential CO_2 reduction can be achieved in the automobile industry. The use of novel steels will reduce the car chassis' thickness, weight, and, as consequence, fuel consumption, while maintaining the actual crashworthiness[1] [13]. The other main application where the introducing of novel high strength steels can have an enormous impact are related to the upgrading of fossil-fuel power plants to higher operating temperatures, and to the construction of wind turbines.

These examples clarify that a better understanding of the causes of H-related mechanical failure of metals is a critical step in the development of embrittlement-resistant materials, which can play a crucial role in achieving the EU's target of a 20% reduction in greenhouse gas emissions due to primary energy production by 2020.

1.1 Scientific background

More than 150 years ago, Deville and Troost discovered that iron and platinum are permeable for H gas [14]. In 1866, Graham discovered the ability of Pd to

---

[1]The crashworthiness of a car is the ability of the structure to protect the passengers during a car crash.

absorb large amounts of hydrogen and that H permeates a Pd membrane at an
appreciably high rate [15]. In 1875, Johnson [16] was probably the first to no-
tice the phenomenon of HE. By bending tests with iron samples prior immersed
in different acids, he observed a reversible "extraordinary decrease in toughness
and breaking-strain" of the samples. After these pioneering works, the metal-
hydrogen systems have attracted attention of many scientists. Hence an enor-
mous body of knowledge about H in metals has been accumulated meanwhile.
For extended reviews on the topic, we refer to the books edited by Alefeld and
Völkl [17, 18], Schlapbach [19, 20], Wipf [21], Fukai [22], and to the references
therein.

Although this strong effort has provided numerous insights into HE, a complete
understanding of its underlying mechanisms is still lacking. Several mechanisms
have been proposed based on experimental and theoretical investigations. The
main ones are:

- **H enhanced localized plasticity** (HELP) [23]: this mechanism is at-
  tributed to the enhancement of dislocation mobility due to the presence of H.
  H atoms in metals are attracted by the strain fields of dislocations and can
  form so-called Cottrell atmospheres around the dislocation cores. When the
  dislocations move these atmospheres can readjust rapidly to the variation
  of the strain fields and remain bound to the dislocation cores provided that
  the diffusion of H in the crystal is fast enough. The Cotrell atmospheres re-
  duce the dislocation-dislocation and dislocation-obstacles interactions with
  resulting changes in the dislocation mobility and concentration, and this
  affects the plastic properties of the metal.

- **H enhanced decohesion** (HEDE) [24]: this mechanism is attributed to the
  weakening of cohesive strength at internal interfaces due to segregated H.
  The HEDE mechanism requires that a critical H concentration is reached
  at the failure site and that H atoms diffuse fast enough to maintain this
  concentration during the crack propagation. It is important to mention that
  the HEDE is supported by indirect experimental evidences as well as by
  atomistic simulations and thermodynamic calculations [25–27]. However,
  it is not yet completely clear which is the critical H concentration, whether
  this can be realistically reached, and how much the cohesive strength of
  interfaces is reduced thereby.

- **H enhanced strain induced vacancy formation** (HESIV) [28]: in this
  case the role of hydrogen has been ascribed to the increase in vacancies
  under strain. This mechanism has been observed only for very high H con-
  centrations.

- **Delayed hydride cracking** (DHC) [29]: this mechanism involves the cleav-
  age of hydride phases, which can be formed in some metals. Metal hydrides
  are generally more brittle than the pure metals. As the HEDE mechanism,
  the DHC requires also a minimum H concentration.

- **Adsorption-induced dislocation emission** (AIDE) [30]: this is based on
  the fact that the nucleation energy of a dislocation at a crack tip is reduced
  by the absorption of H atoms on the crack surfaces. Although as in the
  HELP mechanism it is the resulting enhanced local plasticity that causes
  the HE, in this case dislocation dynamics is influenced by the external H on
  the crack surface, instead of the internal H in the bulk interior of the metal.

Detailed descriptions and discussions of these mechanisms can be found in Refs.
[22, 30–33] and references therein.

Still various concerns or doubts exist regarding the validity of the proposed mech-
anisms. The key reason for these doubts is the dependence of each mechanism
on a particular material, its specific microstructure, and on external conditions
such as H concentration, H charging condition, type of loading, strain rate, tem-
perature, etc. On top of all that it is important to consider that, although these
mechanisms have different origins, they are not mutually exclusive and are likely
to occur simultaneously in many situations. For these reasons, to tackle HE as a
whole is a formidable task. Hence, in this work we focus mainly on one aspect of
the problem, namely the transport of H in metals, which is a common factor for
all the above described mechanisms for HE.

1.2 Importance of diffusion and trapping of H in metals

In general terms, the susceptibility of a metal to HE depends strongly on the
transport of H in the system [34]. For all H-assisted damage mechanisms, a crit-
ical H concentration has to be reached at a critical location [35]. In addition, it

is required that the rate of H transport is sufficiently high to maintain this critical concentration, for example ahead of the crack tip in HEDE, or around the dislocation cores in HELP. However, the mode and rate of H transport in a crystalline material is strongly influenced by the material's microstructure, atomic and extended defects, because the H moving in a material can be trapped by crystal's defects, microvoids, or precipitates of foreign particles [31]. For example, it has been observed that crystal vacancies or transition-metal-carbides precipitates can provide deep traps for H [36–38]. On the other hand extended crystal defects, namely grain boundaries or dislocations, can also enhance the H diffusion by acting as shortcuts for the migration of H atoms [39, 40]. These effects of the crystal's (micro-)structure on H diffusion can be in principle tuned in order to suppress diffusible H. This prevents the H accumulation at critical locations, and hence it increases the resistance of the material to HE [41]. Because of that it is an important task to clarify and to quantify the effects of these types of defects on the transport of H.

The diffusion of H in metallic systems is not only important from the application point of view, but it is also interesting for fundamental research. Because H is the lightest and smallest element, its diffusion is very fast, actually closer to the typical diffusion of particles in liquids [22]. For example, at room temperature, the number of atomic jumps of an H atom in vanadium, about 10^{12} jumps per second, exceeds by 15-20 orders of magnitude those of O or N under the same conditions. This jump frequency of H is similar to the highest lattice-vibration frequency of the host metal [42]. Moreover the migration of H in metals is one example of quantum-mechanical manifestation at the macroscale. H migration has been observed even at very low temperatures: mobility of H in Ta has been observed at 11 K [43] and it has been hypothesized that H can may be mobile even a 0 K [44]. This is due to the possibility that the migration of H at very low temperatures becomes dominated by quantum tunneling instead of classical thermally activated jumping. This has been proposed in numerous studies [22, 45–48].

1.3   Objective of the thesis and theoretical approach

This work was conducted as a part of a large collaborative European project *MultiHy*[2]. The primary objective of this project was to develop an advanced multiscale modeling framework for the prediction of metal susceptibility to HE. To achieve that, the strategy adopted in Multihy [49, 50], illustrated in Fig. 1.1, was to use information obtained at the atomic scale in mesoscale descriptions of H diffusion, which then allow to parameterize continuum models for simulation of macroscopic components with finite element methods [51, 52].

The ambitious goal of a multiscale description of H transport in metals is particularly important since the existing numerical continuum models are not yet able to incorporate the influence of microstructural features while atomistic simulations are limited to small system sizes and short time scales.
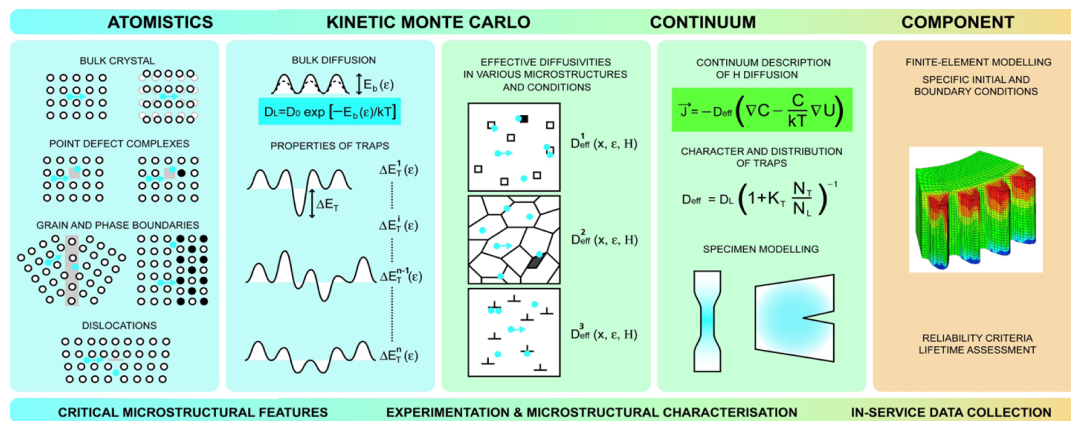
FIGURE 1.1: A schematic diagram showing the coarse–graining strategy used in the MultiHy project for the multiscale modeling of H transport.

The objective of this thesis was to focus on the atomic scale. The obtained results, apart of being used as a microscopic basis for meso- and macroscale simulations, are self-reliant and give an important insight into the interaction between H and metals with a realistic microstructure.

We have investigated the H diffusion and trapping in two prominent transition metals: iron and nickel. These two metals were chosen because their wide use as structural materials and because both of them are sensitive to HE [53–55]. Fe and Ni have different crystal structures, Fe is body-centered cubic (bcc), while Ni is a face-centered cubic (fcc), and it is known that the H diffusion in these two crystal

---

[2]Multiscale modeling of hydrogen embrittlement in crystalline materials (www.multihy.eu)

structures is markedly different [22]. For both models we have first considered the diffusion of H in ideal crystals and investigated the role of quantum-mechanical effects. Then we have considered the interaction of H with different internal interfaces, namely grain boundaries in Ni and heterophase boundaries between a titanium carbide precipitate and the iron metal matrix that, as said above, can have a great influence in the migration of H.

Most of the results reported in this thesis were obtained using atomistic simulations based on density functional theory (DFT). This method is nowadays commonly used for predictive calculations of material properties and can reach high accuracy, since it contains no material-specific empirical assumptions or model parameters. Here only a brief introduction of DFT is given. For a more detailed descriptions we refer to the book by Martin [56] or the review by Payne et al. [57] and the references therein.

Density functional theory

The density functional theory is a computational approach for calculating the electronic structure of systems such as atoms, molecules, and condensed phases of matter. The DFT is theoretically based on two theorems of Hohenberg and Kohn [58], which state that the ground state properties of a many-electron system, in an external potential, are uniquely determined by a ground-state electron density, $\rho(\mathbf{r})$. Hence the electron density is promoted to the key quantity. To understand the advantages of that we consider the problem of solving a system composed of many electrons and nuclei. In principle all information about this kind of system is contained in the total (nucleus + electronic) wavefunction, Ψ. Using the Born–Oppenheimer approximation [59], all nuclear degrees of freedom are cast into an external potential, V_{ext}. The electronic wavefunction ψ can be calculated in non-relativistic approximation from the Schrödinger equation, which for a system of N electrons in an external potential reads:

$$\left[\sum_i^N \left(\frac{\hbar^2 \nabla_i^2}{2m} + V_{ext}(\mathbf{r_i}) \right) + \sum_{i<j}^N V_{ee}(\mathbf{r_i},\mathbf{r_j}) \right] \psi(\mathbf{r_1},\mathbf{r_2},\ldots,\mathbf{r_N}) = E\psi(\mathbf{r_1},\mathbf{r_2},\ldots,\mathbf{r_N}) \quad (1.1)$$

where m is the electron mass, and $V_{ee}(\mathbf{r_i}, \mathbf{r_j})$ is the electron–electron Coulomb interaction. This equation is extremely difficult to solve numerically due to the curse of dimensionality, i.e. it depends on $3N$ variables ($3N + N$ if the spin is also considered) and it cannot be separated into a simpler single–particle equation because of the interaction term $V_{ee}(\mathbf{r_i}, \mathbf{r_j})$. Several sophisticated methods to solve this problem have been developed [60–62], however because the huge computational cost, they are inefficiently for large and complex systems like crystalline materials. The DFT provides a valid alternative, since the key quantity is the electron density which depends only on three spatial coordinates (plus one if the spin is considered), instead of the 3N of the original many-particles problem.

Although the Hohenberg and Kohn theorems are promising and very general, it is *a priori* not clear how to extract from the density any general sets of properties. The first practically useful formulation of DFT was provided by Kohn and Sham [63]. They propose the idea of replacing the kinetic energy of the interacting electrons with that of a fictitious non–interacting system having the same density and moving in an effective potential, $V_{KS}[\rho]$, which itself is a functional of the density. For such system the solution can be written in terms of single-particle orbitals, ϕ_i, that satisfy a Schödinger-like equation of the form:

$$(T_e[\rho] + V_{KS}[\rho])\phi_i = \epsilon_i \phi_i \tag{1.2}$$

For this system of non-interacting electrons in an effective potential the density can be expressed as:

$$\rho(\mathbf{r}) = \sum_i^N |\phi_i(\mathbf{r})|^2, \tag{1.3}$$

and the total energy reads:

$$E[\rho] = T[(\rho)] + E_H[(\rho)] + E_{ext}[\rho)] + E_{xc}[\rho)] + E_{II}[\rho] \tag{1.4}$$

where the kinetic energy can be written as $T[\mathbf{r}] = \sum_{i=1}^N \int |\nabla\phi_i(\mathbf{r})|^2$, the Hartree energy can be written as $E_H[\rho] = \frac{1}{2}\int d\mathbf{r}\int d\mathbf{r}'\frac{\rho(\mathbf{r}')}{\mathbf{r}'-\mathbf{r}}$, the energy contribution from the external potential can be written as $E_{ext} = \int d\mathbf{r}V_{ext}(\mathbf{r})\rho(\mathbf{r})$, and E_{II} is the energy contribution from the classical Coulomb interaction between nuclei. By

variation of the total energy expression with respect to the density, the Kohn-Sham potential is obtained as:

$$V_{KS}[\rho] = V_{ext}[\rho] + V_H[\rho] + V_{xc}[\rho] \qquad (1.5)$$

Eqs. 1.2, 1.3, 1.4, and 1.5 are called the Kohn-Sham equations. At this stage the DFT provides a formally exact method for solving the electronic problem, and the Kohn–Sham equations can be solved by iterative techniques. Unfortunately the analytical form of the so-called exchange-correlation potential V_{xc} in unknown and needs to be approximated. However, many efforts have been done to obtain good approximations for the V_{xc}, and the most widely used ones are the local density approximation (LDA) and the generalized–gradient approximation (GGA). For detailed reviews we refer to [56, 63–65].

1.4 Structure of the thesis

In Chapter 2 we introduce the basic theory of atomic diffusion, and we describe two methods to include quantum-mechanical effects on diffusion. The presented approach is then applied to the diffusion of H in bulk Fe and Ni. Finally, our approach is validated by means of comparison with available experimental data.

In Chapter 3 we investigate the interaction between H and grain boundaries in Ni. In particular we focus on the distribution and migration of H in the vicinity of grain boundaries, an estimation of the H concentration at grain boundaries, and the effects of H on the grain-boundary cohesion.

In Chapter 4 we study the interaction of H with titanium carbide precipitates in Fe. Such precipitates are considered to be efficient traps for H and therefore a possible means to lower the HE susceptibility of Fe-based metallic materials. We characterize in detail the trapping properties of TiC precipitates and correlate our theoretical results with experimental observations.

In Chapter 5 the main findings and the conclusions of our work are summarized.

Chapter 2

Diffusion of H in bulk metals

The content of this chapter, with the exception of Sec. 2.2, has been published in [66]. The results presented in Sec. 2.5.2 have been partially published in [50].

2.1 Introduction

Atomic diffusion refers to the transport of atoms through crystalline or amorphous materials. It plays an important role in many fields of material science. Just a few examples are: phase transformation, oxidation, nucleation and growth precipitates, intermixing of phases. The knowledge of diffusion phenomena is essential for direct technological tasks such as the development of solid electrolytes for all solid-state batteries and fuel cells, doping of semi-conductors, steel hardening through carburization, and many more. For these reasons atomic diffusion has been intensively studied from both experimental and theoretical points of view [67–70].

In this chapter we focus on this particular topic: interstitial H diffusion in iron and nickel. In this cases, as we already stated in the previous chapter, quantum-mechanical effects on the diffusion of H should not simply be neglected. We will show how these effects can be included in a first-principles description of H diffusion based on DFT by means of two different methods. The first one is the semi-classical transition state theory (SC-TST)[71, 72], the second one is based on the small-polaron theory (PS)[73, 74].

The structure of the chapter is the following: in section 2.2 we introduce the basic concepts of diffusion. In Sec. 2.3 we present the commonly used method

to investigate the diffusion in classical approximation: the transition state theory. In Sec. 2.4 we elaborate the two methods used in this work to account for quantum-mechanical effects on H diffusion in metals. In Sec. 2.5, we apply the two approaches to the specific cases of the diffusion of H in bulk Fe and Ni single crystals.

2.2 Fick's laws and diffusion coefficient

Diffusion processes are governed by Fick's laws, which are two empirical laws deduced by Adolf Fick in 1855 [75]. Even if these laws are purely phenomenological, better fundamental understanding of diffusion in solids has not affected their validity.

The Fick's first law describe the flux of diffusing particles which can be atoms, molecules, or ions. For an isotropic material it can be written as:

$$\boldsymbol{J} = -D\nabla C \tag{2.1}$$

where $\mathbf{J}$ is the vector of the diffusion flux, ∇C is concentration gradient vector, and the factor of proportionality, D, is called diffusion coefficient or diffusivity.

Fick's second law describes how the diffusion causes the concentration to change with time. If the diffusion coefficient depends on concentration it can be written as:

$$\frac{\partial C}{\partial t} = \nabla \cdot (D\nabla C) \tag{2.2}$$

If D is independent from concentration Fick's second law can be simplified to:

$$\frac{\partial C}{\partial t} = D\Delta C \tag{2.3}$$

where Δ denotes the Laplace operator.

Eq. 2.2 is a non-linear second-order partial differential equation which usually cannot be solved analytically. Eq. 2.3 is a linear equation and, provided that boundary and initial conditions are formulated, analytical solutions can be found in principle. For reviews on the mathematics of diffusion we refer to the textbooks

of Crank [76] and Glincksman [77].

In Fick's two laws, all information regarding the specific physical system are contained in the diffusion coefficient, D. Experimentally the diffusion coefficient can be obtained by numerous methods based either on the laws of Fick or considering phenomena which are influenced by the diffusion, for instance nuclear magnetic resonance (NMR) [78]. For extended reviews of such experimental methods we refer to the books of Fukai [22] and Mehrer [67] and to the references therein. From theoretical point of view, the diffusion coefficient can be defined in a rigorous way considering the problem at the atomic scale. There, the diffusion in solids is the result of many individual atomic jumps of migrating particles inside the host crystal. Hence the diffusivity can be expressed in terms of quantities like jump rates, jump distances, and correlation factors. Based on the description of the diffusion in terms of a random walk, it is possible [67] to write the variation of the concentration of the diffusing particles, C, in a small time interval τ as:

$$\frac{\partial C}{\partial t} = -\frac{\langle R \rangle}{\tau} \nabla C + \frac{\langle R^2 \rangle}{6\tau} \Delta C \qquad (2.4)$$

where $\langle R \rangle$ is the mean displacement of the migrating particles and $\langle R^2 \rangle$ is the mean square displacement. Without a driving force, $\langle R \rangle = 0$ and Eq. 2.4 reduces to Fick's second law 2.3 and the diffusion coefficient being:

$$D = \frac{\langle R^2 \rangle}{6\tau} \qquad (2.5)$$

The above equation was developed at the same time by Einstein [79] and Smoluchowski [80], and it is commonly called the Einstein or Einstein-Smoluchowski relation.

In equation 2.5 the diffusivity depends on the mean square displacement, $\langle R^2 \rangle$, of the migrating particles. In order to calculate this quantity on a lattice, it is useful to introduce the jump rate, Γ, of a particle to its z neighboring sites. Assuming an uncorrelated random walk, Γ can be expressed as:

$$\Gamma = \frac{\langle n \rangle}{zt} \qquad (2.6)$$

where $\langle n \rangle$ is the average number of jumps in the time t. With this definition the diffusion coefficient reads:

$$D = \frac{1}{6}d^2 z \Gamma \qquad (2.7)$$

where d is the jump length. At this stage we have replaced the problem of calculating the diffusivity with the problem of calculating the jump rate, Γ. This can be done employing the so-called transition state theory (TST).

2.3 Classical transition state theory

([66], Sec. II)

The TST explains the reaction rates in terms of elementary chemical reaction steps. Therefore it can be employed to calculate the jump rate between two stable sites separated by a migration energy barrier. The TST was developed in 1935 simultaneously by Eyring [81], and by Evans and Polanyi [82]. Following Eyring's work, the jump rate can be written as:

$$\Gamma_{TST} = \frac{kT}{h}e^{-\Delta F/kT} \qquad (2.8)$$

where k is the Boltzmann constant, h is the Plank constant, and ΔF is the difference in free energy between the metastable transition state (top of the barrier) and the ground state (local equilibrium position). For better readability, in the following, when we speak about energy difference we always implicitly means the difference between the transition state and the ground state, unless otherwise stated.

The free energy difference can be written as:

$$\Delta F = \Delta U - T\Delta S \qquad (2.9)$$

where ΔU and ΔS are the internal energy difference and entropy difference, respectively. These quantities can be calculated according to the usual thermodynamic expressions:

$$\Delta F = -kT \ln\left(\frac{Z^0}{Z^S}\right)$$

$$\Delta S = -\frac{\partial \Delta F}{\partial T} \tag{2.10}$$

$$\Delta U = \Delta F + T\Delta S$$

where Z^S and Z^0 are the partition functions of the transition and ground states, respectively. If we consider the classical expression of the partition functions in harmonic approximation [83], the entropy difference reads:

$$\Delta S = -k \ln\left[\frac{kT}{h} \frac{\prod_{i=1}^{f-1} \nu_i^S}{\prod_{i=1}^{f} \nu_i^0}\right] - k. \tag{2.11}$$

where f is the number of degrees of freedom in the stable site and $(f-1)$ is the number of degrees of freedom in the transition state (note that in the transition state the frequency associated with the transition path is imaginary), ν_i^0 and ν_i^S are the vibrational frequencies at the stable site and at the saddle point, respectively. The total energy difference is:

$$\Delta U = \Delta E - kT \tag{2.12}$$

where ΔE is the potential energy difference at $T = 0$ K.

By substituting Eqs. 2.12 and 2.11 into Eq. 2.8, we obtain the typically used expression for the jump rate:

$$\Gamma_{TST} = \frac{\prod_{i=1}^{f} \nu_i^0}{\prod_{i=1}^{f-1} \nu_i^S} e^{-\Delta E/kT} \tag{2.13}$$

Substituting Eq. 2.13 into Eq. 2.7, the diffusivity obtained by means of the TST can be written as:

$$D_{TST} = \frac{1}{6} z R^2 \frac{\prod_{i=1}^{f} \nu_i^0}{\prod_{i=1}^{f-1} \nu_i^S} e^{-\Delta E/kT}. \tag{2.14}$$

Before the development of the transition state theory the diffusivity was described by the Arrhenius equation which is represented mathematically as:

$$D_A = A e^{-\Delta E_m / kT}.$$ (2.15)

where A was called pre-exponential factor (in the following simply prefactor) and ΔE_m is the migration energy. Since Eq. 2.15 was found empirically, the physical interpretation of A and ΔE_m remained rather vague. The physical meaning of these two parameters is clarified by the TST. According to Eqs. 2.15, 2.14, 2.11, and 2.12, the prefactor A reads:

$$A = \frac{1}{6} z R^2 \frac{kT}{h} e^{(\Delta S + k)/k} = \frac{1}{6} z R^2 \frac{\prod_{i=1}^{f} \nu_i^0}{\prod_{i=1}^{f-1} \nu_i^S}$$ (2.16)

and the migration energy barrier reads:

$$\Delta E_m = \Delta U + kT = \Delta E$$ (2.17)

Because the prefactor A and the migration energy barrier ΔE_m are temperature independent parameters in Eq. 2.15 the natural logarithm of the diffusion coefficient is linear in $1/T$. This is the so-called Arrhenius behavior.

All the parameters needed in Eq. 2.14 (ΔE and the vibrational frequencies) can be obtained using DFT-based simulations. To calculate ΔE it is necessary to calculate the minimum energy path (MEP) between the stable sites through which the atomic migration occurs. This can be done using the nudge elastic band (NEB) method [84]. For provided initial and final configurations this method finds the MEP by optimizing (i.e. minimizing the energy of) an arbitrary number of intermediate images along the reaction path. Equal spacing between the images is maintained by adding spring forces along the band between images, and by projecting out the component of the force tangential to the migration path direction.

Because the number of employed images is normally not very large and those images are evenly spaced, there is no warranty that the NEB method will find the exact saddle point. To overcome this difficulty it is possible to introduce a small modification to the method [85], namely to invert the true force tangential to the migration path for the highest energy image and cancel the spring forces acting on it. In this way the selected image climbs the potential energy barrier to maximize its energy along the migration path, while relaxing in the other directions. Because of that, this method is called climbing-image nudge elastic band (CI-NEB) method.

The vibrational frequencies can be calculated using DFT in several ways and with different levels of approximations. for complete reviews we refer to Refs. [86, 87].

The described classical theory of diffusion is general and can be applied to any diffusing atom in any crystal structure. In the next section we go into the details of interstitial H atoms diffusing in a metal. In particular we consider the problem of how to include quantum-mechanical effects on the H diffusion, which are taken into account neither in the TST nor in the DFT.

2.4 Quantum mechanical effects in TST

([66], Sec. II)

As we already mentioned, the diffusion coefficient based on TST, Eq. 2.14, has an Arrhenius-like behavior. But experimental studies [78, 88] reveal for several metals, for instance Fe, Ta, and Nb, that when the natural logarithm of the diffusivity of H in some metals is plotted versus $1/T$ the curves often bend upwards for low temperature. This deviation from the Arrhenius behavior is due to quantum-mechanical effects. At low temperature the diffusion of H is influenced by quantum tunneling, the presence of discrete vibrational energy levels, and the zero point energy (ZPE). At high temperature these effects become less important and a classical over-barrier jump migration is the dominating mechanism [22, 74, 89, 90]. The presence of two different diffusion regimes naturally leads to a non-Arrhenius-like behavior [78, 91].

Actually there are three possible temperature regimes [22, 92] in which the dominating diffusion mechanisms are different, Fig 2.1:
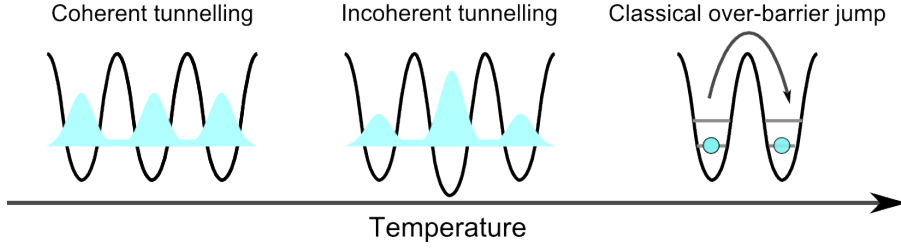
FIGURE 2.1: Illustration of the three possible diffusion regimes for diffusion of H in metals.

- **Coherent tunneling**: In this case the migration of H is barrier-free and can be considered as a propagation of Bloch-like proton states. Since at experimentally reachable temperatures this has never been observed for H isotopes, in the following we did not considered it. Note that coherent tunneling was indeed observed for muons diffusing in metals [93].

- **Incoherent tunneling**, or thermally activated tunneling: In this case the diffusion is not barrier-free. Therefore the tunneling is a thermally activated process. A detailed description of this mechanism is given in the following (where we refer to it simply as tunneling).

- **Classical over-barrier jumping**: This occurs at relatively high temperatures. The H atoms diffuse by thermally activated over-barrier jumps. In this case the diffusion is well described by Eq. 2.14.

Even though the diffusion mechanisms themselves are well known, there is no way to predict the active ones for a material at a given temperature regime. This has to be find out case by case. [46, 94, 95]

In order to include quantum-mechanical effects, the TST can be extended in various ways. The simplest and most common extension [96–100] is to add the difference in zero point energies, ΔZPE, to the energy barrier in Eq. 2.14, so that the diffusivity can be written as:

$$D_{zpe} = \frac{1}{6} z d^2 \frac{\prod_{i=1}^{3} \nu_i^0}{\prod_{i=1}^{2} \nu_i^S} e^{-(\Delta E - \Delta ZPE)/kT} \tag{2.18}$$

where $\Delta ZPE = \sum_{i=1}^{3} \nu_i^0 - \sum_{i=1}^{2} \nu_i^S$. Note that in Eq. 2.18 we have implicitly used the so-called frozen-lattice approximation, i.e. we neglect the contributions from

the vibrational frequencies of the host-crystal atoms, which can be considered immobile because they are much heavier than H atoms.

Despite the ΔZPE correction, the prefactor and the migration barrier in Eq. 2.18 remain independent from temperature so that both Eq. 2.14 and Eqs. 2.18 can describe only a classical Arrhenius behavior. Another problem with Eq. 2.18 is that quantum-mechanical effects should disappear for high temperature, but Eq. 2.18 does not converge to Eq. 2.14 with increasing temperature.

Various more accurate methodologies have been developed to capture the non-classical treatment of the diffusion, for instance, based on the path-integral (PI) method [45, 48, 101–103] or the small-polaron (SP) theory [73, 74, 89, 90]. Both approaches yield very accurate results, but they typically require a very large amount of accurate and reliable input data. Since this is rather time consuming for first-principles calculations, more approximate methods (e.g. tight binding or empirical potentials) are often employed to reduce the computational cost [45, 48, 103]. Unfortunately, these approximated methods usually do not reach the accuracy and reliability of the first-principles methods which makes the validity of the obtained results more uncertain.

As we mentioned above, in this work, we considered two alternative approaches to obtain a non-classical description of diffusion. The first is the SC-TST [71, 72, 104, 105] which has the great advantage of requiring a small amount of input data only and can have the same accuracy as the above-mentioned accurate methods. But unfortunately, it has the limitation that it can be applied to the case of a symmetric barrier only, i.e. to migration paths for which the initial and final sites have the same energy. The second used method is based on a simplified version of the SP theory [73, 74] that allows us to keep the computational cost as low as for the SC-TST. This method has the additional advantage that it can be applied to asymmetric migration paths as well.

2.4.1 Semi-classical corrected transition state theory

Quantum-mechanical effects on the diffusion of interstitial atoms in crystals can be divided into two contributions. The first is due to the zero-point energy of a vibrating proton or, more generally, to the presence of discrete vibrational energy levels and their occupations at finite temperature. The second contribution is due

to quantum-mechanical tunneling.

To take the quantized vibrations (QV) of H into account (including the zero-point energy corrections), it is sufficient to calculate the free energy in Eq. 2.8 using the quantum-mechanical expression, instead of the classical one, for the partition functions. The jump rate then reads [83, 106]:

$$\Gamma_{QV} = \frac{kT}{h} \frac{\prod_{i=1}^{3} 2\sinh(\frac{h\nu_i^0}{2kT})}{\prod_{i=1}^{2} 2\sinh(\frac{h\nu_i^S}{2kT})} e^{-\Delta E/kT} \tag{2.19}$$

consequentially the diffusion coefficient reads:

$$D_{QV} = \frac{1}{6} z d^2 \frac{kT}{h} \frac{\prod_i^3 2\sinh(\frac{h\nu_i^0}{2kT})}{\prod_i^2 2\sinh(\frac{h\nu_i^S}{2kT})} e^{-\Delta E/kT} \tag{2.20}$$

The above expression has the correct limits approaching Eqs. 2.14 and 2.18 for high and low temperatures, respectively. It is useful for the following analysis to rearrange Eq. 2.20 into an Arrhenius-like form in which both prefactor and exponential term converge to their classical values for high temperature. This can be done using Eqs. 2.16 and 2.17. The result is:

$$D_{QV} = D_{QV}^*(T) e^{-\Delta E_{QV}(T)/kT} \tag{2.21}$$

where the prefactor is:

$$D_{QV}^*(T) = \frac{1}{6} z R^2 \frac{\prod_{i=1}^{3} \sinh\left(\frac{1}{2}u_i^0\right)}{\prod_{i=1}^{2} \sinh\left(\frac{1}{2}u_i^S\right)} \frac{e^{\sum_{i=1}^{2} \frac{1}{2}u_i^S \coth(\frac{1}{2}u_i^S)}}{e^{\sum_{i=1}^{3} \frac{1}{2}u_i^0 \coth(\frac{1}{2}u_i^0)}} \tag{2.22}$$

with $u_i^x = h\nu_i^x/kT$, and the migration barrier, $\Delta E_{QV}(T)$, is:

$$\Delta E_{QV}(T) = -kT \sum_{i=i}^{3} \frac{1}{2} u_i^0 \coth\left(\frac{1}{2} u_i^0\right) + kT \sum_{i=i}^{2} \frac{1}{2} u_i^S \coth\left(\frac{1}{2} u_i^S\right) + kT \tag{2.23}$$

Note that $\Delta E_{QV}(T)$ approaches to $\Delta E + \Delta ZPE$ (see Eq. 2.18) as $T \to 0$ while for high temperature it approaches the classical migration energy, ΔE. [105, 106].

While the treatment of the quantized H vibrations via Eq.2.20 in the same in both SC-TST and SP theory, the quantum tunneling is described differently in the two approaches. In the SC-TST, the tunneling is considered to be a correction to the jump rate, Eq. 2.8 and therefore to the diffusion coefficient in Eq. 2.20. Following Fermann and Auerbach [71], the diffusion coefficient in SC-TST can therefore be written as:

$$D_{SC-TST} = D_{QV}Q \tag{2.24}$$

where the tunneling correction factor, Q is expressed as[71]:

$$Q = \frac{exp\left(\frac{\Delta E_{QV}}{kT}\right)}{1 + exp\left(2\theta_0\right)} + \frac{1}{2}\int_{-\infty}^{\theta_0} d\theta \, \text{sech}^2(\theta) exp\left(\frac{h\nu_3^S \theta}{\pi kT}\right) \tag{2.25}$$

with $\theta_0 = \left(\pi\Delta E_{QV}\right)/\left(h\nu_3^S\right)$, $\nu_3^S = i\tilde{\nu}$ with $\tilde{\nu}$ being the imaginary vibrational frequency at the saddle point associated with the migration direction. It should be noticed that in the original work [71], ΔE_{QV} is approximated as the zero-point-energy corrected migration energy barrier ($\Delta E + \Delta ZPE$) while in our work the physically correct temperature-dependent expression according to Eq. 2.23 is used. The integral in Eq. 2.25 can be evaluated numerically.

In an analogous way as for Eq. 2.20, i.e. using Eqs. 2.16 and 2.17, it is possible to rewrite Eq. 2.24 in an Arrhenius-like form, as:

$$D_{SC-TST} = D_{eff}^* e^{-\Delta E_{eff}/kT} \tag{2.26}$$

with the effective migration energy, ΔE_{eff}, and the effective prefactor, D_{eff}^*, having the proper low and high limits.

2.4.2   Small polaron model: Flynn and Stoneham method

In the small polaron model developed by Flynn and Stoneham (FS) [74], the tunneling contribution is not included as a correction to the diffusion coefficient in Eq.
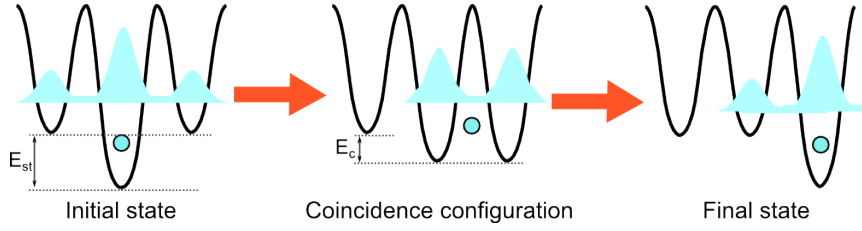
FIGURE 2.2: Schematic representation of the incoherent tunneling diffusion according to the FS model.

2.20, but it is considered as a distinct diffusion mechanism with its own diffusion coefficient. The FS method is based on the concept of coincidence configurations. At very low temperature, approaching the absolute zero, all similar interstitial sites in a crystal have the same energy, as illustrated in Fig. 2.1, and the H atoms can be considered to be in a Bloch-like state, in which diffusion occurs by coherent tunneling. As the temperature raises, the phonons tend to destroy the coherence and therefore the diffusion becomes slower. Because of that the H atom has enough time to equilibrate with its surrounding. This causes a local distortion of the host crystal lattice which makes the state more stable and causes the H to localize there, Fig. 2.2. The energy gained by the lattice distortion is called self-trapping energy, E_{st}. By thermal vibrations eventually two neighboring sites can become energetically equivalent and the H atom delocalizes between them. This configuration is called coincidence configuration and the energy that the localized H needs to gain in order to reach this configuration is called coincidence energy, E_c. Because just in this configuration tunneling can occur, it is called thermal activated (or incoherent) tunneling.

In the FS method, the rate, Γ^{FS} for incoherent tunneling of a proton between ground states at two neighboring sites, p and p', is expressed as:

$$\Gamma^{FS} = \left(\frac{\pi}{4\hbar^2 E_c kT}\right)^{\frac{1}{2}} J_{pp'}^2 e^{-\frac{E_c}{kT}} \tag{2.27}$$

where $J_{pp'}$ is the tunneling matrix element and E_c is the coincidence energy.

To obtain properly these two quantities several first-principles calculations are required to map out the potential energy landscape of the migrating proton in the crystalline material. The Schrödinger equation for a proton in this potential can then be solved [89, 90, 95].

In order to keep the computational cost low, we do not follow this route but instead make several approximations. The matrix element, $J_{pp'}$, for a proton tunneling between two neighboring sites, p and p', can be calculated starting from the Hamiltonian of a crystal containing an interstitial atom [74]:

$$\mathscr{H} = \mathscr{H}_I + \mathscr{H}_{int} + \mathscr{H}_L \tag{2.28}$$

where $\mathscr{H}_I = -(\hbar^2/2m)\nabla^2$ is the kinetic energy of the interstitial, $\mathscr{H}_L$ is the perfect lattice Hamiltonian of the host crystal, and $\mathscr{H}_{int}$ in the interaction energy between the interstitial and the host lattice. This last term can be written as the sum of the contributions from different interstitial sites, p:

$$\mathscr{H}_{int} = \sum_p \mathscr{H}_{int}^p \tag{2.29}$$

Applying the Born-Oppenheimer approximation twice, first between the electrons and the nuclei and second between the lighter interstitial proton and the heavier lattice nuclei, it is possible to separate the eigenfunctions of $\mathscr{H}$ into products of the eigenstates of $\mathscr{H}_L$ and the eigenstates, $\tilde{\phi}_p$, of the Hamiltonian terms that act on a proton:

$$\left(\mathscr{H}_{int}^p + \mathscr{H}_I\right)\tilde{\phi}_p = E_p\tilde{\phi}_p \tag{2.30}$$

where E_p is the energy of the proton at the site p. Within the harmonic approximation, the eigenfunction $\tilde{\phi}_p$ is the ground-state wavefunction for the harmonic oscillator centered at the site p which can be written as:

$$\tilde{\phi}_p = \left(\frac{\alpha_x\alpha_y\alpha_z}{\pi^3}\right)^{(1/4)} e^{-\frac{\alpha_x}{2}x^2 - \frac{\alpha_y}{2}y^2 - \frac{\alpha_z}{2}z^2} \tag{2.31}$$

For a second harmonic oscillator centered at the neighboring site p', the ground-state wavefunction is:

$$\tilde{\phi}_p = \left(\frac{\alpha_x\alpha_y\alpha_z}{\pi^3}\right)^{(1/4)} e^{-\frac{\alpha_x}{2}(x+R)^2 - \frac{\alpha_y}{2}y^2 - \frac{\alpha_z}{2}z^2} \tag{2.32}$$

where $\hat{x}$ is the direction connecting the sites p and p' separated by the distance R, $\alpha_j = \frac{m\omega_j}{\hbar}$, ω_j is the angular frequency of the proton associated with the vibration direction $\hat{j}$, and m is the H mass.

If we consider the tunneling between two states only, the tunneling matrix element, $J_{pp'}$, can be calculated as the matrix element between the ground state of the two harmonic oscillators centered at two neighboring interstitial sites, as:

$$J_{pp'} = \langle \tilde{\phi}_p | \mathcal{H}_{int} + \mathcal{H}_I | \tilde{\phi}_{p'} \rangle \tag{2.33}$$

By adding and subtracting $\langle \tilde{\phi}_p | \mathcal{H}_I | \tilde{\phi}_{p'} \rangle$, we obtain:

$$J_{pp'} = \langle \tilde{\phi}_p | \mathcal{H}_{int}^p + \mathcal{H}_I | \tilde{\phi}_{p'} \rangle + \langle \tilde{\phi}_p | \mathcal{H}_{int}^{p'} + \mathcal{H}_I) | \tilde{\phi}_{p'} \rangle - \langle \tilde{\phi}_p | \mathcal{H}_I | \tilde{\phi}_{p'} \rangle \tag{2.34}$$

Using Eqs. 2.30, 2.31, and 2.32, and recognizing that the energies E_p are the zero-point energies of the H at the sites p and p', ZPE_p and ZPE_p', from Eq. 2.34 it is possible to obtain the equation for the tunneling matrix element, which results to be:

$$J_{pp'} = S\left(ZPE_{p'} + ZPE_p\right) - K \tag{2.35}$$

where ZPE_x is the zero point energy at site x, and

$$S = \langle \tilde{\phi}_p | \tilde{\phi}_{p'} \rangle \text{ and } K = -\frac{\hbar^2}{2m} \langle \tilde{\phi}_p | \frac{d^2}{dx^2} | \tilde{\phi}_{p'} \rangle \tag{2.36}$$

are the overlap and kinetic energy integrals.

The coincidence energy, E_c, can be approximated, in case of migration between equivalent sites, by one quarter of the self-trapping energy, E_{st} [89, 90, 92]. In case of hopping between two non-equivalent sites the difference between their ground-state energies needs to be added to the self-trapping energy of the proton in the initial position, as illustrated in Fig 2.3.
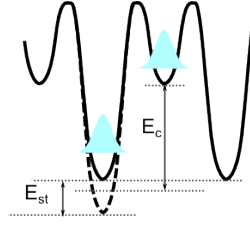
FIGURE 2.3: Schematic representation of energies needed in the FS model equation in case of hopping between two non-equivalent jump.

Equation 2.27 is valid only for a temperature range low enough to assume that only the hydrogen ground state is occupied and that migration is by incoherent tunneling only, but high enough to treat the host-lattice phonon modes classically [89, 90]. In order to extend the model to the range of temperatures which we are interested in, we consider a superposition of the tunneling diffusivity, Eq. 2.27, and the over-barrier jumping diffusivity, Eq. 2.20 [78], so that the overall diffusivity within the FS model is:

$$D_{FS} = D_{QV} + \frac{1}{6} z R^2 \Gamma_{FS} \tag{2.37}$$

Note that both the SC-TST and FS expressions (Eqs. 2.24 and 2.37) for the diffusion coefficient take into account all quantum mechanical effects for any temperature while requiring the same amount of information from DFT calculations as the simple ZPE-corrected expression of TST, Eq. 2.18.

2.5 Application of SC-TST and FS model

([66], Sec. II, III, and IV)

The two above described approaches to include quantum mechanical effects in the description of H diffusion are applied in this section to the specific cases of H migration in bcc Fe and in fcc Ni. This two systems have been chosen both because of their high relevance for technical applications, and because in experimental investigations they show a rather different diffusion behavior. The diffusivity of H in Fe breaks the classical Arrhenius-like behavior, whereas it is apparently followed well by the diffusivity of H in Ni (see experimental data in Figures 2.4 and 2.6 for H in Fe and Ni, respectively). We show that our results agree very well

with those of the computationally more demanding PI methods [45, 48, 103], and provide a consistent interpretation of the available experimental data [47, 107–111].

2.5.1   Computational details

The SC-TST and FS method, Eqs. 2.24 and 2.37 have been parameterized with data from DFT calculations. All needed input data (energy barriers, and vibrational frequencies) were obtained by means of DFT calculations performed using the mixed-basis pseudopotential (MBPP) method [112–115]. A generalized gradient approximation (GGA) was employed for exchange-correlation, and spin polarization was taken into account. For the Brillouin-zone integration in the calculation of total energies and forces, Monkhorst-Pack k-point meshes of 4x4x4 were used for both the cubic supercells containing 16 Fe atoms or 32 Ni atoms.

2.5.2   Case study I: Fe-H system

The most stable interstitial position for dilute hydrogen in bcc iron is in the tetrahedral site (T-site) [96, 97, 116]. The optimized lattice parameter of our 16-atom Fe supercell with a single H atom is 2.91 Å, which corresponds to about 1% volume expansion with respect to pure Fe. The MEP connecting two neighboring T-sites has been determined by a CI-NEB calculation with the corresponding classical energy barrier ΔE =90 meV. This value agrees very well with the results of previous computational studies [45, 48, 96, 97] that used larger supercells containing up to 128 Fe atoms. This comparison also verifies that the 16-atom supercell is sufficiently large to avoid any serious finite-size errors in ΔE.

The vibrational energies of H in the tetrahedral site and at the saddle-point position were calculated within the harmonic approximation and are listed in Table 2.1. Using these values, we computed the ZPE correction, ΔZPE=0.044 eV, which is again consistent with values obtained in other theoretical investigations. [96, 97]

The vibrational energies are used to calculate the diffusion coefficient for H in bcc Fe within the SC-TST according to Eq. 2.24 and within the FS model according to Eq. 2.37. The jump distance R was chosen to be the geometrical distance between

ΔE	$h\nu_1^0$	$h\nu_2^0$	$h\nu_3^0$	$h\nu_1^S$	$h\nu_2^S$	$h\nu_3^S$	$J_{pp'}$	E_c
0.090	0.251	0.178	0.087	0.210	0.210	0.101	0.0022	0.0035

TABLE 2.1: Classical over-barrier migration energy, ΔE, vibrational energies, $h\nu_i^x$, tunneling matrix element, $J_{pp'}$, and coincidence energy E_c (all energies are in eV) for H in Fe. The vibrational energies are calculated from the curvatures of the energy-displacement curves of an H atom in the Fe crystal (frozen-lattice approximation). There are three distinct energies at the tetrahedral site. The reference frame is such that the $h\nu_3^0$ is the energy of vibrations parallel to the $\langle 110 \rangle$ migration path while $h\nu_1^0$ and $h\nu_2^0$ are related to vibrations in two perpendicular directions.

two neighboring tetrahedral sites along $\langle 110 \rangle$, i.e., $R = \frac{\sqrt{2}}{4}a$, where $a = 2.91$ Å is the corresponding lattice parameter for the $Fe_{16}H$ supercell.

The resulting temperature dependencies of the H diffusion coefficient are plotted in Fig. 2.4 together with those obtained from the classical TST with (Eq. 2.18) and without (Eq. 2.13) the ZPE correction. Both TST dependencies have the expected Arrhenius-like behavior ($ln(D) \propto 1/T$), albeit with different slopes. The dependencies obtained using the SC-TST and the FS model are clearly non-Arrhenius-like, both showing a strong convex bending. A good agreement between the two approaches can be seen in Fig. 2.4, with small differences becoming apparent only at low temperatures.

Both models are in good agreement and predict a clear non-Arhenius-like behavior with a strong enhancement of diffusivity at low temperatures due to quantum effects. For low temperatures, the curve obtained by means of the SC-TST is somewhat lower than the outcome of the FS model, but the absolute differences remain rather small. For high temperatures, both curves coincide and converge to the result of classical TST.

Our results, in particular the one obtained by means of the FS model, are in a remarkably good agreement with theoretical results of Kimizuka et al. [48] and Yoshikawa et al. [103] who employed variants of the PI method. A similar study by Katzarov et al.[45] also confirms the non-Arhenius behavior, but the obtained enhancement of diffusivity at low temperatures is less pronounced.

Apart from these theoretical results, there exist many experimental investigations on H diffusion in bcc Fe [47, 107–111]. In Fig. 2.4, we included most recent
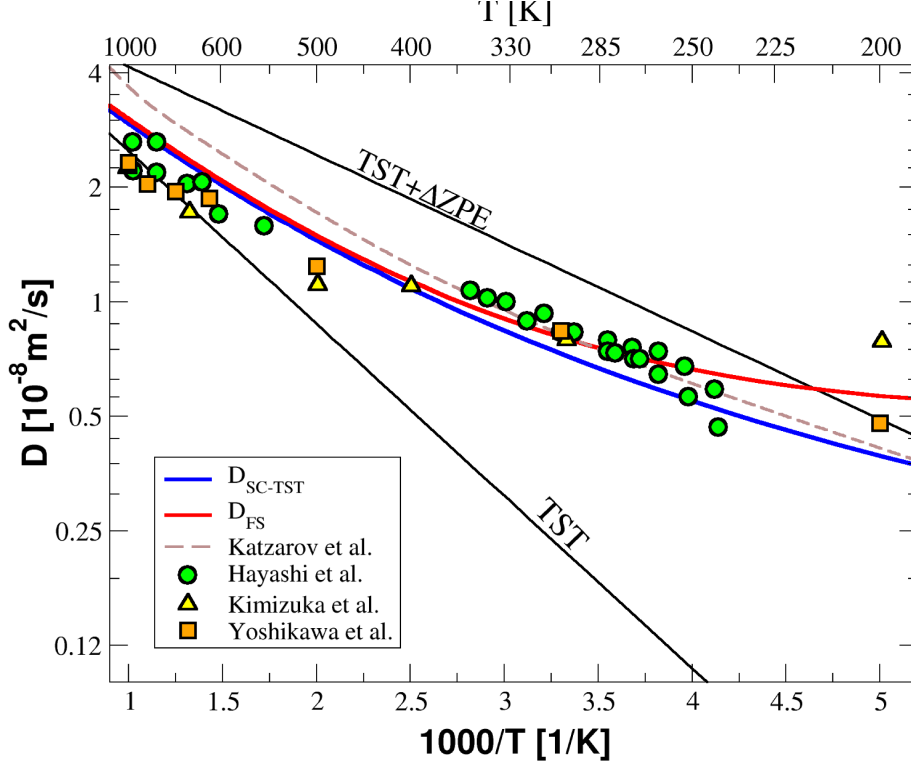
FIGURE 2.4: Temperature dependencies of diffusion coefficients for the Fe-H system. The solid blue and red curves represent our results obtained by means of the SC-TST and FS model, respectively. The dashed brown curve corresponds to theoretical PI-method results of Katzarov et al. [45] while the triangles and the squares mark results of similar calculations obtained by Kimizuka et al. [48] and Yoshikawa et al. [103], respectively. Recent experimental data of Hayashi et al. [107] are shown by green circles. For completeness the results obtained with classical TST with and without ΔZPE correction are shown as thin black lines.

experimental data of Hayashi et al. [107] who provided results of individual measurements. This allows a direct comparison with the theoretical results and shows again a very good agreement between theory and experiment. Unfortunately, such a direct comparison with other experimental results is not straightforward since Arrhenius-like behavior of the diffusivity is usually anticipated in experimental analyses and only temperature independent migration energy barriers and prefactors are reported after analyzing the measurements. We refer further to these quantities as 'apparent' migration energy ΔE_{app} and 'apparent' prefactor D^*_{app}. These quantities can be compared to the effective energy barrier and prefactor, ΔE_{eff} and D^*_{eff} (see Eq. 2.26).

The results of such an analysis for bcc Fe are presented in Fig. 2.5. The temperature-dependent effective energy barrier obtained from our D_{SC-TST} curve is drawn as a thick blue line. Corresponding effective energy barriers reported by Katzarov

et al. [45] and by Kimizuka et al. [48] are also shown. The figure also contains apparent energy barriers reported by various experimental investigations, and the temperature-independent classical (dashed line labeled as TST) and ZPE-corrected (dotted line labeled as TST+ΔZPE) TST migration energies.
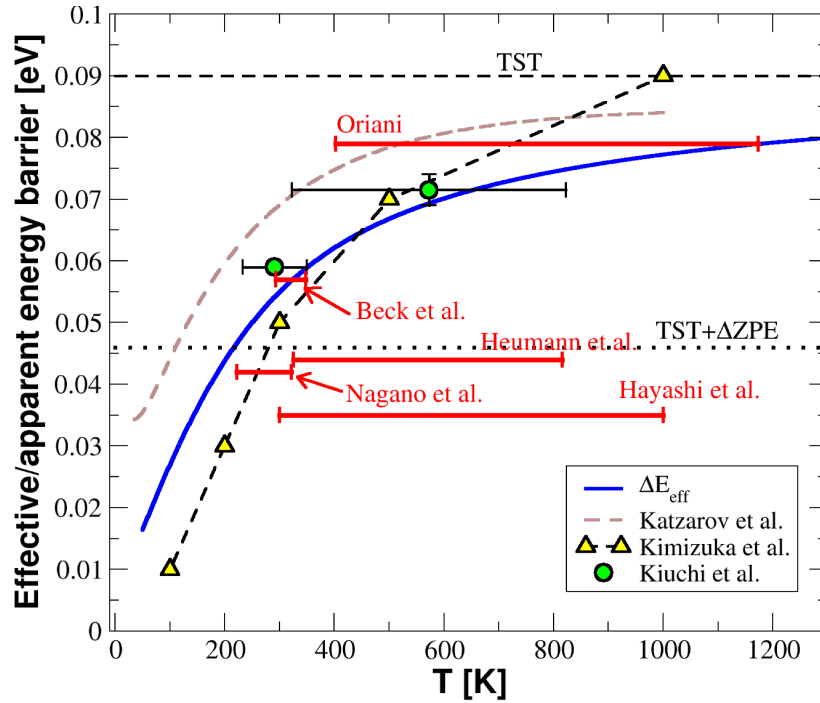

FIGURE 2.5: Comparison of effective and apparent activation energies for migration of H in bcc Fe. Experimental results from Kiuchi and McLellan [47] are reported as green circles with error bars; apparent activation energies obtained by Oriani [110], Heumann et al. [111], Beck et al. [108], Nagano et al. [109], and Hayashi et al. [107] are displayed as red bars spanning the temperature ranges in which the diffusivities have been measured.

The effective migration energies from all theoretical studies shown in Fig. 2.5 exhibit the expected behavior. At high temperature they converge to the classical value of 0.09 eV, but the rate of convergence depends on the method. In the case of the SC-TST, the convergence is rather slow which is probably due to the harmonic approximation used to calculate the vibrational frequencies of the interstitial H atom. To improve the convergence, these frequency parameters perhaps need to be evaluated in a more sophisticated way [46, 94, 117, 118].

The experimental results in Fig. 2.5 extracted from small temperature ranges show an overall good agreement with the results obtained by theory. However, this is not the case for the apparent activation energies derived from fitting over large temperature ranges. The disagreement is particularly surprising for the

study by Hayashi et al. [107] since their individually measured diffusivity values agree very well with our theoretical curve of $\ln D$ vs. $1/T$ (see Fig. 2.4). This means that the discrepancy for the migration barrier is mainly due to the linear approximation assumed when interpreting the measured diffusivity values. This is supported by Kiuchi and McLellan [47] who carried out an extensive statistical analysis of various experimental results available from more than 40 published studies by the year 1983. Based on this analysis, they isolated two distinct temperature regimes associated with two apparent energy barriers. As shown in Fig. 2.5, these energy barriers are in good quantitative agreement with our result.

Interestingly, the ZPE-corrected energy barrier, $\Delta E + \Delta ZPE = 0.046$ eV, is within the range of values derived from the experimental data [107, 109, 111]. This agreement is only accidental and rather unfortunate since the ZPE correction is used widely [96–100] as the simplest way to include the quantum corrections. The ZPE correction is strictly correct only at $T = 0$ K and vanishes for high temperatures. As shown in Fig. 2.5, the ZPE-corrected migration energy barrier overestimates the effective energy barrier at low temperatures (below 200 K) and underestimates it for temperatures above 400 K. The agreement with the effective energy barrier and some of the experimental estimates around room temperature is only fortuitous since the overestimated ZPE-contribution at room temperature is in fact compensated by the missing tunneling contribution. Hence, these two strong approximations apparently result in a value for the energy barrier which appears to be reasonable around room temperature.

2.5.3   Case studied II: Ni-H system

In bulk fcc Ni, H atoms migrate between the most stable octahedral interstitial sites (O-sites) through metastable tetrahedral sites (T-sites). Consequently, the MEP consists of two jumps, one from the initial O-site to a neigboring T-site and another from this T-site to the final O-site. The first O-T jump is characterized by a much higher classical energy barrier ($\Delta E^{O-T} = 0.37$ eV) than the second T-O jump ($\Delta E^{T-O} = 0.10$ eV). Since the O-T transition governs the H diffusion in fcc Ni, it is sufficient to consider only the ΔE^{O-T} barrier as the overall diffusion barrier. This approximation means that once the proton has overcome the first barrier to the T-site, it proceeds immediately to the final O-site. In this case,

the overall jump distance corresponds to the distance between two neighboring O-sites along $\langle 110 \rangle$, i.e., $R = \frac{\sqrt{2}}{2}a$ with $a = 3.54$ Å for our $Ni_{32}H$ supercell.

A complication associated with the two-step MEP is that there exist, in principle, also two possible tunneling mechanisms. The first one is from an O-site to a T-site while the second one is directly between two neighboring O-sites. Unfortunately, in neither of these two cases it is possible to employ the SC-TST to estimate the diffusion coefficient. In the first case, the initial O-site and the final T-site are not equivalent and hence the transition cannot be treated with the SC-TST. In the second case, the direct O-O tunneling along $\langle 110 \rangle$ direction cannot be seen as a correction to the classical O-T-O over-barrier jumps along $\langle 111 \rangle$ directions since the geometrical paths are different.

The FS method is not affected by the two-step MEP and can be applied to investigate both tunneling processes independently. However, we found that both tunneling contributions are negligible (the tunneling matrix elements are less than 10^{-6}) so that the H diffusivity in fcc Ni is described accurately by Eq. 2.21 only. This result is shown in Fig. 2.6 together with the diffusivities obtained from the classical TST with and without the ZPE corrections, and experimental data. All the calculated quantities used as input data to evaluate the H diffusion coefficient in fcc Ni are listed in Table 2.2. Note that the frequencies at the O-site and T-site are three-fold degenerate while at the saddle point they are twofold degenerate.

ΔE^{O-T}	ΔE^{O-O}	$h\nu^O_{1,2,3}$	$h\nu^T_{1,2,3}$	$h\nu^S_{1,2}$	$h\nu^S_3$	$J_{pp'}$	E^{O-O}_c	E^{O-T}_c
0.37	0.84 [106]	0.10	0.15	0.21	0.10	$< 10^{-6}$	0.0015	$\Delta E^{O-T}_{qv}(T)$

TABLE 2.2: Classical migration energies ΔE^x, vibrational energies $h\nu^x$, tunneling matrix element $J_{pp'}$, and coincidence energies E^x_c for H in fcc Ni (all energies are in eV).

In this case, the quantum effects do not alter the Arrhenius-like diffusion behavior over the entire temperature range considered here (see Fig. 2.6). The reasons are two-fold. First, the energy barrier for H migration is much higher in fcc Ni than in bcc Fe and, hence, the relative contribution of quantum corrections is much smaller. Second, the tunneling effects calculated from the FS model give no significant contribution. The transmission rates of the two possible tunneling mechanisms in Ni, the one connecting directly two neighboring octahedral sites and the other connecting the octahedral sites via an intermediate tetrahedral site, are negligibly low. For the former mechanism, this is because of the large distance
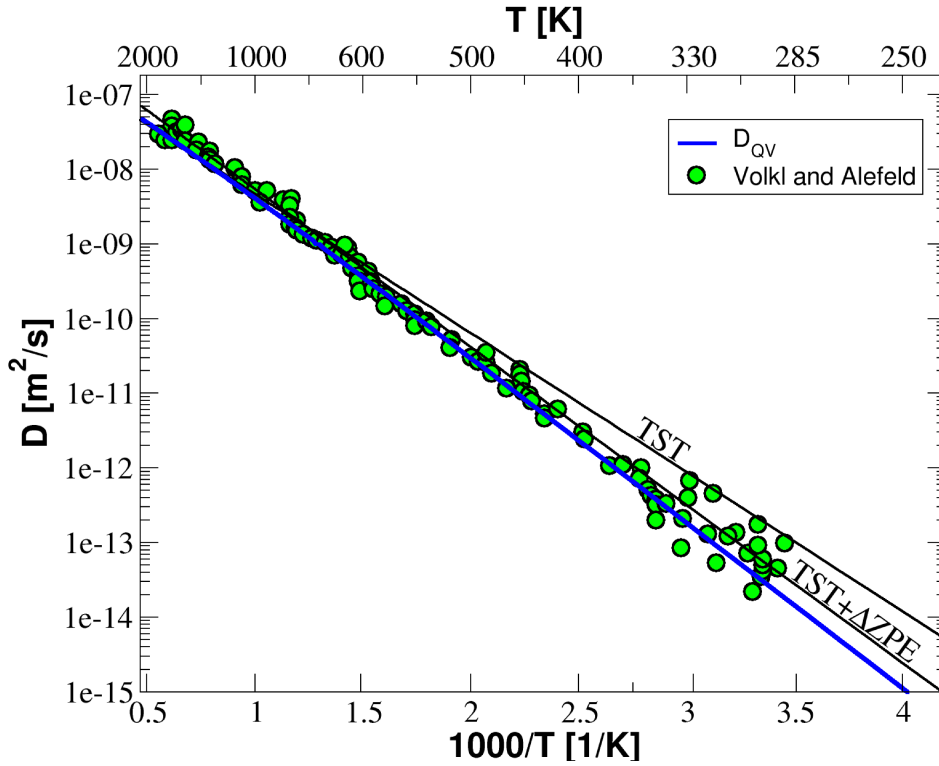
FIGURE 2.6: Temperature dependencies of diffusion coefficients for the Ni-H system. The solid blue line represents results obtained in this study using the FS model while the results obtained using classical TST with and without ΔZPE correction are shown as thin black lines; experimental data from Ref. [119] are marked by green circles.

between the involved sites in fcc Ni, more than two times larger than in bcc Fe. In the latter mechanism, the distance is smaller (still 50% larger than in Fe), but the tunneling probability is nullified by a too high coincidence energy in Ni, which is two orders of magnitude higher than in Fe.

In Fig. 2.6, the obtained diffusion coefficients (both classical and with quantum-mechanical corrections) are compared with a large number of experimental results [119]. Both classical and quantum-mechanical results show a good agreement with experimental data, but the quantum corrections do seem to provide a better agreement at low temperatures. This is corroborated by some experimental investigations [104, 120] which have reported isotope effects that can be explained only by considering quantum-mechanical effects.

It is interesting to notice that in the case of fcc Ni, the ΔZPE contribution increases the effective energy barrier, i.e., the diffusivity curve becomes steeper. This is in accordance with some experimental data [22] where the reported apparent migration energies tend to increase as the considered temperature increases.

Similarly to the Fe-H system, we analyzed the effective migration energy according to Eq. 2.23 also for the Ni-H system. As shown in Fig. 2.7, the effective migration energy shows a very different behavior than for bcc Fe. It converges to the classical migration energy for high temperatures, but it approaches the ZPE-corrected migration energy as temperature approaches 0 K. Nevertheless, it is important to keep in mind that the obtained effective energy barrier should not be taken as exact for very low temperatures because in this case other tunneling mechanisms, such as coherent tunneling [78, 90, 93] may become relevant. However, this low temperature regime is less relevant for practical applications.
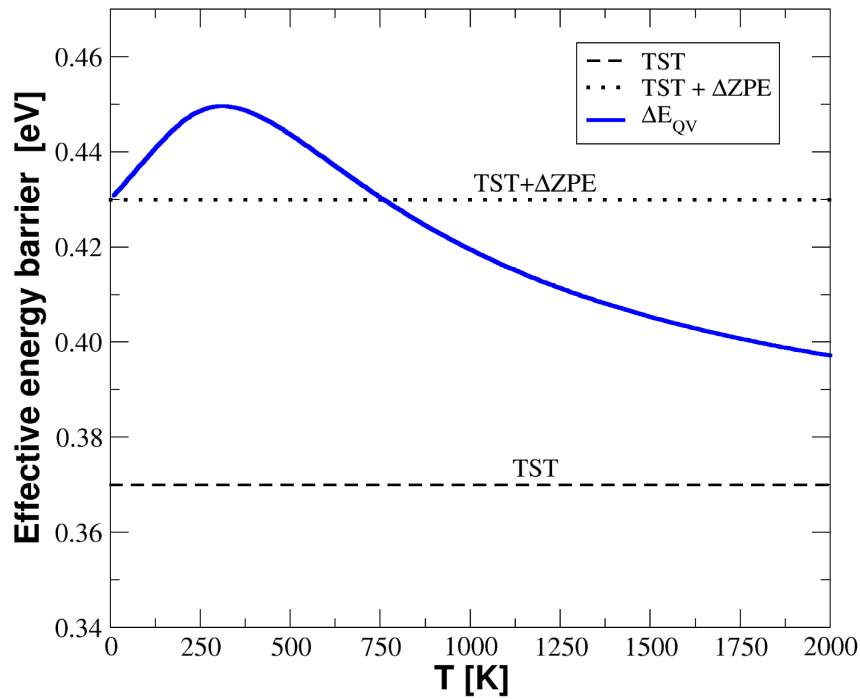
FIGURE 2.7: Effective migration energy for H in Ni. The result is compared with the classical migration energies with (dashed line) and without (dotted line) ΔZPE correction.

2.6 Conclusion

([66], Sec. V)

In this chapter we investigated the H diffusion in bulk materials. The diffusion coefficients for the migration of H in two illustrative systems, namely bcc Fe and fcc Ni, were precisely calculated over a wide range of temperatures. Quantum-mechanical effects were included by means of the semi-classical transition-state

theory and the small-polaron model of Flynn and Stoneham. The obtained diffusion coefficients agree well with other theoretical and experimental studies. Moreover the comparison with experimental results reveals that the large scatter in the reported data for H diffusion in bcc Fe is related to the Arrhenius-type analysis which is usually applied for the interpretation of the measured diffusion data.

The two approaches used to include quantum-mechanical effects have two strong advantages over the other theoretical methods used in literature. First they are simple to apply and require only a small number of theoretical input data. This makes them potentially applicable to more complex situations such as H diffusion at extended defects in the microstructures of materials. The second advantage is that both the semi-classical transition-state theory and Flynn-Stoneham model allow to relate easily the weight of quantum of quantum-mechanical effects to basic physical properties of the investigated system. This feature can be used to predict whether a quantum-mechanical description of diffusion of H in a given system is essential or not. For instance, we showed that in case of Ni the difference in energy between the octahedral and tetrahedral sites is one of the reasons for the negligible tunneling contribution to the H diffusion. Therefore one can expect that in systems with similar diffusion paths, the tunneling effect is negligible as well. As we will show in the next two chapters, this is important to simplify the study of the interaction of H with microstructural features of materials.

Chapter 3

Interaction of H with grain boundaries in nickel

In the previous chapter we investigated the diffusion of H in single crystals. In this chapter as well as in the next one, we make a step forward and focus on the interaction between structural defects and hydrogen in materials. In this chapter in particular we investigate the interaction of H with grain boundaries in Ni. In this case in addition to investigating the transport of H in polycrystalline Ni, we address the H effects on the material integrity.

The Secs. 3.2 and 3.3 of this chapter has been published in [121].

3.1   Introduction

For metals like Ni that do not form hydrides, the list of possible mechanisms proposed to explain H-induced failures, see Sec. 1.1, reduces to HELP/AIDE, HEDE, and HESIV. Nevertheless it is still under debate which mechanism dominates. Experimental investigations clearly observe effects of the presence of H on the fracture mode of many metals. However the interpretation and the underlying physical mechanisms are still controversial [33, 35, 122, 123]. For example, Bechtle et al. [124] have observed that the fracture mode of polycrystalline Ni changes sharply from intragranular and ductile to intergranular and brittle

when the material is charged with H. However, the transition depends sensitively on the microstructure of the metals and the abundance of special grain boundaries (GBs), as defined in the following. These observations clearly indicate that hydrogen affects the cohesion of grain boundaries, as proposed in the HEDE mechanism, and that the sensitivity of a GB to HE likely depends on its interface structure [124, 125]. Nevertheless, in a follow-up work, Martin et al. [126] concluded that plasticity always plays an important role in hydrogen-induced embrittlement of Ni, even when the macroscopic fracture appears to be brittle. The HELP mechanism, considering the variation of dislocation mobility due to hydrogen, can therefore be a contributing factor as well. The reason for this controversy is probably due to the fact that the hydrogen-induced failure mechanisms are not mutually exclusive and are likely to contribute simultaneously to the failure. For instance, a recently proposed mechanism [33, 122, 123] predicts that HELP/HEDE mechanisms create the conditions for the onset of failures (i.e. establishing a critical hydrogen content at grain boundaries and increasing local stresses), but the failure process itself is due to the HEDE (or HESIV) mechanism. This can explain most of the experimental observations, but several key questions remain open. In particular it is necessary to quantify the synergy or competition between plasticity-mediated and decohesion mechanisms and to evaluate for all failure mechanisms, the conditions under which they are likely to occur.

In this work we aim to shed some light on this topic focusing on the investigation of the HEDE mechanism at grain boundaries in Ni using first-principles calculations. We focus on three key questions, namely:

- How is the transport of hydrogen is influenced by GBs?

- How much hydrogen can be accumulates at GBs?

- How does hydrogen influence the cohesion properties of GBs?

Our theoretical approach is described in Sec. 3.2 followed by a detailed discussion of each of the three key questions in Secs. 3.3, 3.4, and 3.5. Special emphasis will be given to the description of H transport in the presence of GBs.

3.2 Theoretical approach: GB models

Grains in a polycrystalline material without texture are oriented randomly, therefore many grain misorientations and interface inclinations are possible. This variety leads to a virtually infinite number of GB types [127]. Nevertheless it is possible to identify two main GB classes [127]: *low–angle* and *high–angle* GBs. In this study, we did not consider low-angle GBs, which can be well described by dislocation networks, we focused only on high-angle GBs with characteristic atomic structural units. This class of GB can be divided into two subsets, namely, singular (often also called special) and general GBs [127]. In singular GBs, most of the interfacial atoms fit very well with the crystal structures of both adjoining grains and attain also a favorable configuration at the interface. Because of the weak distortions and a favorable atomic structure, these GBs are at a local minimum in the energy with respect to geometrical and microscopic degrees of freedom. On the contrary, in general GBs the interfacial atomic structure is strongly distorted and contains large regions of poor structural match of interfacial atoms and/or significant excess volumes.

Since it is practically impossible to investigate the interaction of H with all the possible GBs, in this work we have selected two symmetric tilt grain boundaries (STGBs), the $\Sigma5(210)[001]$ STGB and the $\Sigma3(111)[\bar{1}10]$ STGB, as representatives of the singular and general GB sets, respectively. These GBs (denoted briefly as $\Sigma5$ and $\Sigma3$ in the following) have very distinct interface structures and, as discussed in detail in the following, can be considered also as representative cases for a broader variety of GB types.

Structure of the $\Sigma3(111)[\bar{1}10]$ GB
([121], Sec. 3.2)

The supercell used to model the $\Sigma3$ GB supercell consists of an orthorhombic cell with 24 Ni atoms and contains two GBs separated by five atomic (111) layers. The relaxed GB structure is shown in Fig. 3.1, the corresponding supercell dimensions and the GB energy are given in Table 3.1. The first-nearest-neighbor distances between Ni atoms in the vicinity of the GB deviate less than a half percent from the bulk value of 2.50 Å indicating that the atomic arrangement at the interface is only slightly distorted. This is not surprising, since the presence of this twin

interface only alters the stacking of the close-packed (111) planes. As a result, the $\Sigma3$ GB has a negligible excess volume (see Table 3.1), and the calculated GB energy of 0.18 J/m^2 is very small in comparison to typical GB-energy values [128].
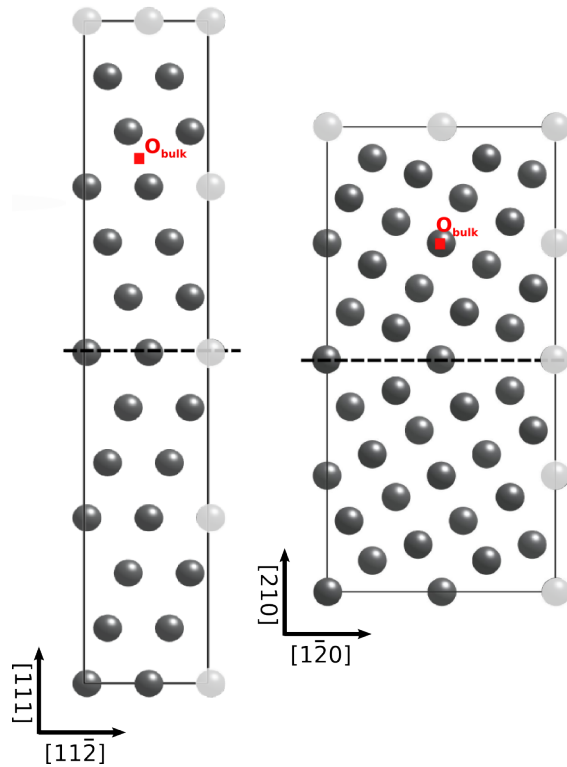

FIGURE 3.1: Relaxed supercells for the $\Sigma3$ GB (left) and for the $\Sigma5$ GB (right) containing 24 and 40 Ni atoms, respectively. The dashed lines mark the GB interface planes; the repeated atoms due to the periodic boundary conditions are shown in light grey; bulk octahedral sites are marked by red squares.

STGB	a [Å]	b [Å]	c [Å]	γ_{GB} [J/m^2]	ΔV [Å^3]
$\Sigma3(111)[\bar{1}10]$	4.320	2.502	24.51	0.18	0.8
$\Sigma5(210)[001]$	7.928	3.545	16.41	1.29	11.1

TABLE 3.1: Supercell dimensions, GB energy, γ_{GB}, and excess volume, ΔV, for the relaxed supercells of the two investigated GBs.

Structure of the $\Sigma5(210)[001]$ GB

([121], Sec. 3.3)

The $\Sigma5$ GB can be described by an orthorhombic supercell containing 40 Ni atoms distributed on 10 atomic (210) layers. Previous studies [26, 129, 130] have shown that this supercell is sufficiently large to avoid spurious interactions between the

two GBs and their periodic images. The relaxed GB structure is shown in Fig. 3.1, characteristic data are listed in Table 3.1. Note that it is possible to define an equivalent base-centered orthorhombic supercell with non-rectangular axes in the ab plane and half of the number of atoms containing the same number of atomic (210) planes, but each one containing one Ni atom only, as sketched in Fig. 3.2.
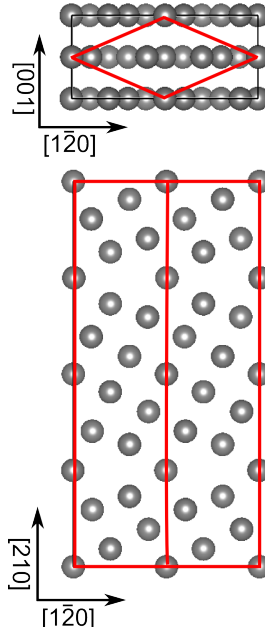

FIGURE 3.2: Illustrative representation of the size of the two supercells with which is possible to model the Σ5 GB. The black and red borders are for the larger and smaller supercell, respectively.

The larger supercell has been used for the work in Sec. 3.3, where we want a dilute H concentration, while the smaller supercell has been used for the studies in Secs. 3.4 and 3.5, where high H density at GBs is considered.

In contrast to the Σ3 GB, the local atomic and electronic structures of the Σ5 GB are significantly different with respect to the bulk interior. In order to visualize these differences, in Fig. 3.3 we plot several cross sections displaying the valence electron densities in the Σ5 supercell. In the central (bulk) part of the supercell (see the cross section in Fig. 3.3b), the regions of the lowest electron density are located at the regular octahedral interstitial sites in bulk Ni. In contrast, much larger regions of low electron density are present along the GB plane (see Figs. 3.3a and 3.3c). We refer to these regions further as cavities and analyze their role in the segregation and diffusion of H in detail below. The presence of the cavities along the GB plane reflects the more open structure of the Σ5 GB, which is also characterized by much larger excess volume than that for the Σ3 GB (cf.

Table 3.1). In addition, the distorted atomic structure also leads to a significantly higher GB energy, comparable to energies of most GBs in Ni [128].
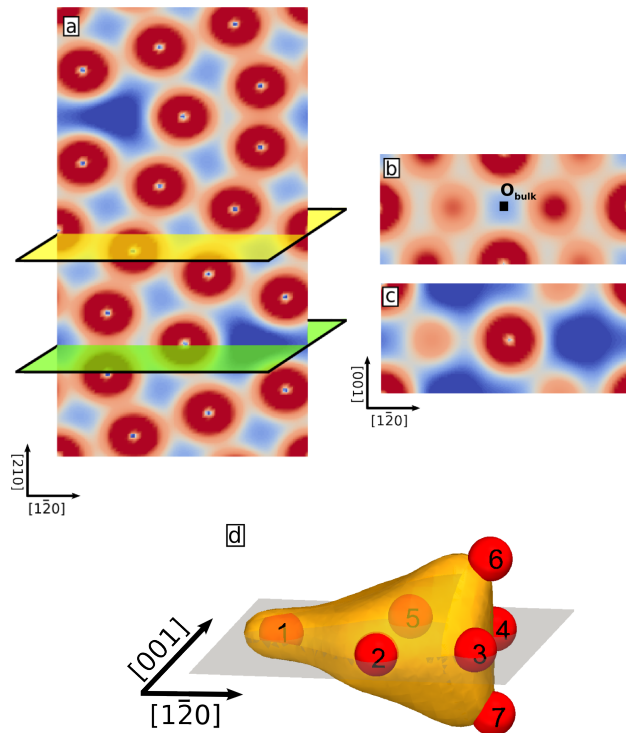

FIGURE 3.3: Valence electron density plots for the $\Sigma 5$ GB: panel (a) shows a cross section along the (001) plane, panels (b) and (c) depict cross sections along two (210) planes in the bulk-like region (highlighted in yellow in (a)) and at the GB plane (highlighted in green in (a)). The red and blue colors correspond to areas of high and low electron densities, respectively. The region of the lowest electron density in the bulk cross section corresponds to an ordinary octahedral site. On the (a) and (c) cross sections, the GB cavities with low electron density are clearly visible in blue. (d) A 3D depiction of the GB cavity as an isosurface corresponding to electron density of 0.14 Å^{-1}); the superimposed red spheres mark the metastable segregation sites for hydrogen atoms.

3.3   Trapping and diffusion of H at grain boundaries

As already stated, the diffusion of H is a key factor common to all HE mechanisms. For the HEDE mechanism, in particular, it is necessary to reach a critical H concentration in the vicinity of the failing GBs. Additionally it should be reached at an accumulation rate comparable with the propagation rate of a crack [35, 123]. It becomes immediately clear that in order to fulfill this requirement, it is necessary

for the H atoms to be both able to diffuse fast towards the GBs and become efficiently trapped there. Whereas most reports in the literature [26, 39, 129, 131–133] agree on favorable trapping properties of GBs, it is still rather controversial whether the GBs can also enhance H diffusion [32, 39, 131, 132, 134–136]. This controversy originates from a complicated interplay between intrinsic crystal properties, the microstructure of the material, and external conditions, but it is also partly due to a lack of systematic atomic-scale information regarding the diffusion of H along GBs. So far, only a few experimental studies [39, 137, 138] have considered, for example, the dependence of the H diffusivity at GBs on their interface character. Moreover, in experimental studies it is often difficult to exclude effects of other structural imperfections, such as vacancies, dislocations, or impurities, which can all influence the diffusion measurements. In computational studies, the major difficulty lies in the massive amount of work required to identify and investigate representative cases from the virtually infinite variety of possible GBs in materials. We are confident that in this study this issue is qualitatively captured well by considering the two selected GBs, the $\Sigma 5$ STGB and the $\Sigma 3$ STGB, which have, as shown in the previous section, markedly different structures: the $\Sigma 3$ twin boundary is closer to the perfect crystal while the $\Sigma 5$ is more akin to a general GB.

H in bulk Ni

As a reference for this chapter we have used the results for H diffusion in bulk Ni presented in the previous chapter. Here we recall the most relevant results. Neglecting any quantum mechanical effects, the calculated energy barrier associated with the jump of a H atom was found to be 0.37 eV. We have seen that in case of H in Ni, quantum corrections to this value are relatively small. In addition, as it is discussed in the following, to take into account quantum-mechanical effects for H diffusion along or to GBs is a complex task which does not critically influence the conclusions and findings reported in this chapter. For these reasons, we limited the investigation of the interaction of H with GBs to the classical TST treatment.

An additional important quantity for characterizing the H-Ni systems is the solution energy for an isolated H occupying an octahedral interstitial site in pure Ni,

which is calculated according to Eq. 3.4. The obtained value of 0.084 eV is similar to values obtained in other computational studies [139–141].

3.3.1   Computational details

([121], Sec. 2)

The two GB models were investigated by means of density functional theory simulations using the Vienna ab-initio simulation package (VASP) [142, 143]. A generalized gradient approximation (GGA) in the form given by Perdew, Burke and Ernzerhof [64] was employed for exchange–correlation and ultrasoft pseudopotentials [144] were used for the core-valence interactions. All calculations were carried out as spin-polarized. For the Brillouin-zone integrations, Monkhorst-Pack k-point meshes of 6x10x1 for the Σ3 and 4x8x2 for the Σ5 were used. For supercells without H, both ionic positions and cell vectors were relaxed. In supercells containing H atom, the dimensions were kept fixed (identical to the corresponding supercells without H) and only the ionic positions were relaxed. The DFT calculations for this section were done at the computer center of the Karlsruher Institut für Technologie together with Dr. Matous Mrovec.

The investigated GBs are characterized by the GB energy calculated as

$$\gamma_{GB} = \frac{E_{GB} - E_{bulk}}{2A},\tag{3.1}$$

where E_{GB} is the total energy of the supercell containing the GB, E_{bulk} is the total energy of bulk Ni crystal with the same number of atoms, and A is the interface area of one GB in the supercell (the factor of two in the denominator takes into account that there are two identical GBs in the supercell). Lower values of γ_{GB} generally indicate a stronger cohesive bonding between the two grains in contact. Another useful parameter characterizing the GBs is the associated excess volume per one GB in the supercell defined as

$$\Delta V = \frac{V_{GB} - N V_{Ni}}{2},\tag{3.2}$$

where V_{GB} is the total volume of the supercell containing the GB, N is the number of atoms in the supercell, and V_{Ni} is the volume per atom of bulk Ni. Larger

values of ΔV indicate a more open GB structure, while smaller values indicate a more compact GB structure. The factor of two in the denominator indicates that ΔV in the excess volume of one of the two GBs in the supercell.

The efficiency of a GB to trap H atoms is quantified by the segregation energy, E^{seg}, defined as

$$E^{seg} = E^{sol}_{GB} - E^{sol}_{bulk},\qquad(3.3)$$

where the E^{sol}_{GB} and E^{sol}_{bulk} are the solution energies of H segregated at the GB and in the middle of a grain remote from the GBs (in the same supercell), respectively. The solution energy for an H atom at a site x is defined as

$$E^{sol}_x = E_{x+H} - E_x - \frac{1}{2}E_{H_2},\qquad(3.4)$$

where E_{x+H} is the total energy of supercell containing H, E_x is the total energy of the same supercell without H, and E_{H_2} is the total energy of an isolated H_2 molecule. With these definitions, negative values of the solution energies indicate that it is energetically more favorable for H to be dissociated and absorbed in Ni, while negative values of the segregation energies imply a preferable segregation of H at the GB.

3.3.2 Results

H segregation at the GBs
([121], Sec. 3.4)

In order to quantify H segregation, an H atom was inserted at various interstitial positions in the two GB supercells, and the structures were subsequently relaxed. For the $\Sigma 3$ GB, two sites were selected: (i) a bulk-like octahedral site in the middle of one grain in the supercell (further referred to as $O^{\Sigma 3}_{bulk}$ site), and (ii) an octahedral site located in between the GB plane and its immediately neighboring (111) plane (further referred to as $O^{\Sigma 3}_{GB}$ site). The reason why the H atom was not placed directly at the GB plane is that due to the local A-B-A stacking of the (111)

planes, there are no octahedral interstitial sites at the GB plane (see Fig. 3.5b and discussion below). The segregation and solution energies, calculated according to Eqs. 3.3 and 3.4, are listed in Table 3.2.

The solution energy of 0.08 eV in the bulk region of the GB supercell is the same as the value for the reference bulk configuration mentioned above. In case of the $O_{GB}^{\Sigma 3}$ site, the solution and segregation energies are only marginally lower than those in the bulk. The small segregation energy of only -0.01 eV indicates that the trapping of H at the $\Sigma 3$ GB is almost negligible.

Site	E_x^{sol} [eV]	E^{seg} [eV]	ρ_{el} [Å^{-3}]
$O_{bulk}^{\Sigma 3}$	0.08	0.00	0.18
$O_{GB}^{\Sigma 3}$	0.07	-0.01	0.18
$O_{bulk}^{\Sigma 5}$	0.09	0.00	0.18
$O_{GB+1}^{\Sigma 5}$	0.10	0.01	0.18
$T_{GB}^{\Sigma 5}$	0.06	0.03	0.23
$S_1^{\Sigma 5}$	-0.14	-0.23	0.13
$S_2^{\Sigma 5}, S_5^{\Sigma 5}$	-0.13	-0.22	0.13
$S_3^{\Sigma 5}, S_4^{\Sigma 5}$	0.00	-0.09	0.15
$S_6^{\Sigma 5}, S_7^{\Sigma 5}$	-0.08	-0.17	0.15

TABLE 3.2: Solution and segregation energies for various bulk-like (marked with subscript *bulk*) and interface (marked with subscript *GB*) sites in the two investigated GB supercells. The O labels correspond to sites with octahedral symmetry, the S and T labels correspond to the metastable sites within the $\Sigma 5$ GB shown in Figs. 3.4(a) and 3.6.

In the case of the $\Sigma 5$ GB, the number and variability of possible segregation sites is much larger. For the bulk octahedral site (further referred to as $O_{bulk}^{\Sigma 5}$) in the middle of a grain (see Figs. 3.1 and 3.3b), we again obtain the solution energy that is very similar to the reference solution energy for H in bulk Ni. Within the GB cavity, we were able to identify seven metastable sites where H can segregate (further referred to as $S_1^{\Sigma 5}$ to $S_7^{\Sigma 5}$), as illustrated in Fig. 3.3d. Most of the sites ($S_1^{\Sigma 5}$ to $S_5^{\Sigma 5}$) lie on the GB plane, while the sites $S_6^{\Sigma 5}$ and $S_7^{\Sigma 5}$ are located approximately at the level of the (210) Ni planes adjacent to the GB plane. Due to the mirror symmetry of the GB cavity with respect to the (001) and (210) planes, the sites 2 and 5, 3 and 4, and 6 and 7 are equivalent. For all these sites, the computed segregation energies are negative (cf. Table 3.2), but the values for the most and

least trapping site differ by more than 0.1 eV. In addition, we also explored several interstitial sites surrounding the GB cavity and identified two sites, one with tetrahedral ($T_{GB}^{\Sigma 5}$) symmetry and one with octahedral ($O_{GB+1}^{\Sigma 5}$) symmetry, that are most relevant for the H migration into and out of the GB cavity (see Fig. 3.5c and discussion in the next section).

In order to relate the calculated segregation energies to the underlying local electronic structure at the GBs, we also analyzed the electron density, ρ_{el}, at all sites before inserting the H atom. The obtained values are listed in the last column of Table 3.2. The reference electron densities at octahedral and tetrahedral sites in the bulk Ni supercell amounting to 0.18 and 0.25 Å^{-3}, respectively, are fully consistent with the values found in the GB supercells. In contrast, the electron densities at the most favorable segregation sites within the $\Sigma 5$ cavity are significantly lower. The lowest electron density of only 0.07 Å^{-3} was found in the middle of the GB cavity.

H migration to, across and along the GBs
([121], Sec. 3.5)

The distorted atomic structure of GB is expected to alter also the local migration pathways and associated energy barriers for H jumps. We investigated the H migration in the vicinity of both GBs using either the NEB method or, in a few cases, just a linear interpolation between the initial and final states without relaxing the intermediate atomic configurations (i.e., effectively unrelaxed NEB calculations).

In the case of the $\Sigma 3$ GB, we used NEB to calculate the minimum energy paths (MEPs) for H jumps in three distinct cases: (i) a jump between two bulk-like octahedral sites remote from the GB, (ii) a jump between two neighboring octahedral sites parallel to the GB, and (iii) a jump between two octahedral sites across the GB plane. It turned out that in the first two cases the MEP is equal to that in the perfect crystal, where the migration takes place through a metastable tetrahedral site (see Fig. 3.5a), with a calculated migration energy barrier of 0.37 eV. In the third case, the migration path differs from the bulk case since the neighboring octahedra across the GB plane share their faces instead of edges as in bulk (compare panels a and b of Fig. 3.5). As a result, the neighboring octahedral sites across the GB plane are connected without the intermediate tetrahedral site. This path is characterized by a calculated migration energy barrier of 0.55 eV, which is almost
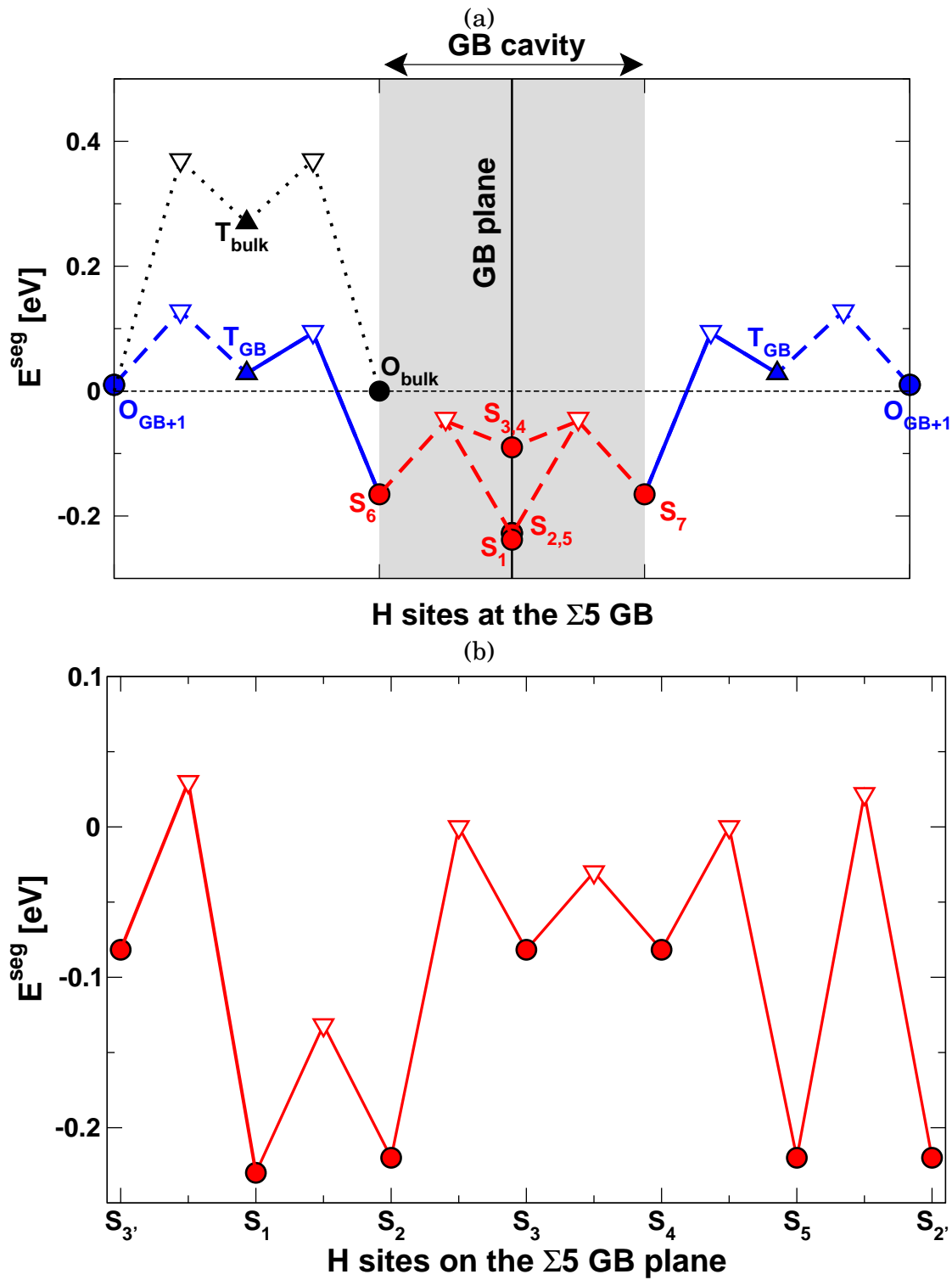
FIGURE 3.4: Segregation energies for metastable H sites (full symbols) and associated transition states (empty symbols) for H migration across (a) and along (b) the Σ5 GB. The full and dashed lines correspond to relaxed and unrelaxed NEB calculations, respectively. The black symbols connected by the dotted black line represent the minimum energy path for H migration in bulk Ni.

50% higher than the barrier in bulk Ni. This indicates that the Σ3 GB acts as a two-dimensional barrier for H diffusion.
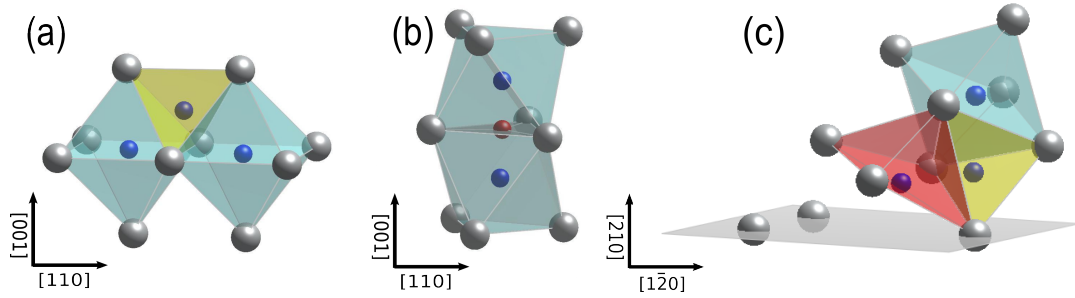

FIGURE 3.5: (a) Atomic arrangement of bulk fcc Ni showing two octahedra connected by their edges. The MEP for H diffusing between the neighboring octahedral interstitial sites (blue spheres) goes via the metastable tetrahedral position (black sphere in the center of the yellow tetrahedron). (b) In the Σ3 GB, the octahedra share their faces parallel to the GB plane with a saddle-point position (red sphere) in the center of the shared triangle. (c) Local atomic structure around the $S_6^{\Sigma5}$ (blue sphere in red pyramid, tetrahedral site $T_{GB}^{\Sigma5}$ (blue sphere in the yellow tetrahedron), and octahedral site $O_{GB+1}^{\Sigma5}$ (blue sphere in the blue octahedron) relevant for the migration to/from the Σ5 GB.

In the case of the Σ5 GB, the migration pathways are much more complex, and we therefore analyzed separately the H jumps along and across the GB. For H migration along the GB plane, we employed the NEB method to calculate the minimum energy paths connecting the sites $S_1^{\Sigma5}$ to $S_5^{\Sigma5}$, both within one single cavity and between two neighboring cavities. The results of these NEB calculations were interpolated to obtain the whole potential energy surface (PES) for H migration along the Σ5 GB plane (see Fig. 3.6). The migration barriers for the most relevant transition states are displayed in Fig. 3.4b. The five locally stable positions inside the cavity are connected by saddle points of relatively low migration barriers, not exceeding 0.22 eV, so that H can move rather freely inside the cavity. Transitions between neighboring cavities can occur via two distinct paths, namely, between either sites $S_1^{\Sigma5}$ and $S_{3'}^{\Sigma5}$ or sites $S_5^{\Sigma5}$ and $S_{2'}^{\Sigma5}$ (see Fig. 3.6). These transitions are characterized by migration barriers which are somewhat higher than those inside the cavities but still significantly lower than the barrier of 0.37 eV between two octahedral sites in bulk Ni. The highest barrier within the GB corresponds to the jump from $S_1^{\Sigma5}$ to $S_{3'}^{\Sigma5}$ with an energy of 0.27 eV. This energy barrier can therefore be considered as the determining barrier for the diffusion of H atoms along the GB plane. Furthermore, since the migration barrier for $S_5^{\Sigma5}$ to $S_{2'}^{\Sigma5}$ and $S_2^{\Sigma5}$ to $S_3^{\Sigma5}$ are only marginally lower (0.24 and 0.22 eV), the diffusion within the Σ5 GB plane can be considered as rather isotropic.
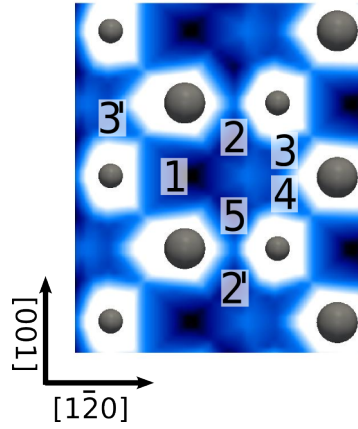
FIGURE 3.6: Potential energy surface for H along the Σ5 GB plane obtained by interpolation of several NEB calculations. Dark blue and black colors indicate the energy minima, light blue colors indicate regions of intermediate energies, and the white color corresponds to high-energy regions of H repulsion very close to Ni atoms (grey balls) that have not been sampled. The labels $1-5$ correspond to the metastable positions, $S_x^{\Sigma 5}$, listed in Table 3.2; note that the sites 3, 4 and 3', as well as 2, 5 and 2', are equivalent.

For H diffusion across the Σ5 GB, the crucial events are jumps into or out of the most favorable segregation sites inside the GB cavity. We identified a MEP joining the $S_6^{\Sigma 5}$ site via the adjacent tetrahedral site $T_{GB}^{\Sigma 5}$ to a bulk-like octahedral site $O_{GB+1}^{\Sigma 5}$. The local atomic configuration around these sites is displayed in Fig. 3.5c. In addition, we also investigated the transitions between the cavity sites lying directly on the GB plane (i.e., $S_1^{\Sigma 5}$ to $S_5^{\Sigma 5}$) and the $S_6^{\Sigma 5}$ and $S_7^{\Sigma 5}$ sites located in two cavity lobes extending away from the GB plane (cf. Fig 3.3c). Due to the high computational cost, only the $S_6^{\Sigma 5}$ to $T_{GB}^{\Sigma 5}$ jump was calculated using NEB. The remaining barriers (marked by dashed lines in Fig. 3.4a) were obtained from linear interpolations between the metastable configurations without relaxing the NEB. They therefore are upper limits for the barriers. The results in Fig. 3.4a show that the barriers for H migration from the bulk interior towards the GB plane are very low. The rate-controlling event for H to escape from the GB is the jump from the cavity to the $T_{GB}^{\Sigma 5}$ site with migration energy of 0.27 eV. This barrier is higher than those for H migration along the GB plane, but it is still significantly lower than the barrier for H diffusion inside bulk Ni.

3.3.3 Discussion

([121], Sec. 4)

The results reported for the H trapping and diffusion in the presence of the two selected GBs indicate that their different interfacial structures result in different interaction behaviors with H atoms. The first difference is with regard to H segregation. While the segregation energy for the $\Sigma 3$ GB is negligibly small, the $\Sigma 5$ GB possesses multiple trapping sites with moderate segregation energies ranging from -0.09 to -0.23 eV. This indicates that the $\Sigma 3$ does not attract H atoms, whereas the $\Sigma 5$ acts as an efficient two-dimensional sink for H. These results agree with those of earlier computational studies on polycrystalline Ni. Geng et al. [26] and Yamaguchi et al. [129] have investigated the H segregation at the $\Sigma 5$ GB and reported segregation energies of about the same value for the most stable site. It is also interesting to note that the segregation energy found for the interstitial H atoms at the cavity of the $\Sigma 5$ GB agrees surprising well with the value of -0.27 eV reported by other investigators [140, 141] for H trapped at a vacancy in bulk Ni. This result may be surprising at first, since it does not correlate with the excess volume, which is about twice as large for the vacancy ($V_{vac} = 11.0$ Å^3) than for the GB cavity ($V_{cav} = 5.5$ Å^3). However, it becomes clear when taking into consideration that the most stable H sites in both cases are not at the locations of the lowest electron density, but instead H atoms prefer to attach to internal surfaces of the two defects where the electron density is higher. The existence of an optimum electron density for H binding (chemisorption) to a metal has been predicted within the effective medium theory (EMT) [31, 145, 146]. Our calculations confirm the correlation between the electron density and the segregation energy (cf. Table 3.2) with the optimum electron density ranging between 0.13-0.15 Å^{-3} at the internal surfaces of the GB cavity. For electron densities higher than 0.15 Å^{-3} (e.g., in the bulk interstitial sites or transition states) or lower than 0.13 Å^{-3} (e.g., in the middle of a vacancy or the GB cavity) the segregation energies become smaller.

The second difference between the two investigated GBs concerns the diffusion of H. The migration of an H atom in the vicinity of the $\Sigma 3$ GB parallel to the GB plane is essentially equal to its migration in the bulk interior of Ni. However, the diffusion across the GB plane is associated with a significantly higher barrier of 0.55 eV, compared to 0.37 eV in the bulk. Hence, this GB acts as a two-dimensional barrier for diffusing H atoms.

In contrast, the migration of H towards the Σ5 GB is characterized by energy barriers that are much lower than the bulk barrier. The diffusing H atoms can easily reach the favorable segregation sites inside the GB cavities, but the escape rates are much lower due to significantly higher migration barriers for the reverse jumps (cf. Fig. 3.4a). As a result, the Σ5 GB can also behave as a barrier for H diffusion, not because of higher migration barriers but due to effective trapping.

Since the migration along the Σ5 GB (i.e., within and between the cavities) is characterized by a mean migration barrier which is lower than that in the bulk by almost 30%, the diffusion along the GB is much faster than the bulk diffusion. To estimate the enhancement of the H diffusion along the Σ5 GB, we recall from Chapter 2 that the diffusion coefficient, D, is proportional to the jump rate, $\Gamma \propto e^{-\frac{\Delta E_{mig}}{kT}}$, Eq. 2.7, and we assume similar prefactors for the diffusivities in the bulk and at the GB. We can then estimate the ratio between GB and bulk diffusivities at room temperature as:

$$\frac{D_{\Sigma5}}{D_{bulk}} \sim e^{-\frac{\Delta E_{mig}^{\Sigma5} - \Delta E_{mig}^{bulk}}{kT}} \sim 10^2. \tag{3.5}$$

This estimated value suggests that the H diffusivity at the atomic scale along the Σ5 GB is about two orders of magnitude greater than that in the perfect single crystal. For a more accurate treatment, it would be necessary to employ mesoscopic approaches, such as kinetic Monte Carlo simulations, to capture the influence of H trapping and concentration [133, 141]. Furthermore, it is important to bear in mind that the results obtained here are strictly valid just for local H migration around the GBs at the atomic scale. To describe properly the macroscopic diffusion of H in polycrystalline materials, it is necessary to calculate an effective diffusivity that depends strongly on microstructural aspects such as grain size, distribution of GB types, and GB connectivity [51, 52, 54, 147, 148]. A more detailed description of this issue is given in the next section.

All the results presented so far are obtained by neglecting quantum mechanical effects. Based on the results of Chapter 2, it is reasonable to state that in bulk Ni an inclusion of these effects is not really crucial. The reason is that the initial and final configurations are not equivalent in energy and/or separated to far. Based on that considering the MEP for diffusion along the Σ5 GB, Fig. 3.4b, the only energy

barrier which could be effectively influenced by quantum tunneling is the one between the sites S_5 and $S_{2'}$. But eventual corrections to this barrier will not effect significantly the overall diffusivity. A H atom migrating along the Σ5 GB needs to cross always the energy barrier between the sites S_5 and S_4 (or S_2 and S_3 when moving in the opposite directions) which is similar to the barrier between S_5 and $S_{2'}$ but asymmetric and therefore marginally changed by quantum-mechanical corrections. This can be seen from Fig. 3.6.

As mentioned above, we assume that the specific properties of these two GBs are applicable to and characteristic for a wider variety of GBs. Additionally, we have provided support for this assumption based on geometrical considerations which agree well with our results. The "perfect" structure of the Σ3 twin boundary makes it the most coherent GB (in fcc metals), while the Σ5 has features that are more akin to a general GB, i.e., a more open structure composed of characteristic structural units (cf. Fig. 3.3), and a rather high GB energy (cf. Table 3.1). In order to further validate the hypothesis that this GBs can be considered as representative for other GBs, we performed a detailed comparison of experimental and other computational results, not only for Ni but also for other metals.

The comparison with experimental results is not easy because in most studies an effective diffusion in polycrystals is reported only. Because of that, we focus first on the recent studies of Oudriss et al. [39, 138], who carried out a systematic investigation of diffusion coefficients and migration energies for H in various Ni microstructures. The reported migration energy of 0.25 eV for general GBs is quantitatively consistent with the range of values obtained in our study for the H migration along the Σ5 GB. Even though it is not possible to identify the exact GB types from the reported experimental studies, this agreement gives weight to our hypothesis that Σ5 GB can be cautiously considered as a representative for general GBs. In addition, Oudriss et al. [39, 138] reported that the effective H diffusivity gradually increases by up to two orders of magnitude when the grain size is reduced, but for nanocrystalline Ni with grain diameters below 0.1 μm it decreases again. This enhancement of diffusivity with increasing fraction of GBs is again consistent with our results. However, the comparison is in this case not trivial due to additional effects of H concentration, trap filling, GB connectivity, and the presence of other crystal defects such as dislocations, which all likely affect the measured diffusivities. Also earlier experimental studies [137, 149, 150] consistently report an accelerated H diffusion with GB diffusivities being 1-2 orders of magnitude faster than the bulk diffusivity. Nevertheless, as already pointed

out, it is difficult to make quantitative comparisons.

A very limited number of atomistic simulation studies on H diffusion at Ni GBs are available in the literature. Molecular dynamics studies [135, 151] based on an embedded-atom method potential of Angelo and Baskes [152] showed a significant enhancement of H diffusion at various Ni GBs. To our knowledge, no first-principles calculations exist for Ni, but Du et al. [131] investigated recently the interaction of H with GBs in fcc Fe using DFT. Similar to our study, they considered two different GB types, $\Sigma 3(111)[1\bar{1}0]$ and $\Sigma 11(113)[1\bar{1}0]$ STGBs, as representatives of dense and open GB structures. In neither of these two GBs H trapping or diffusion enhancement was found. While these results are consistent with ours for the $\Sigma 3$ GB, they appear contradictory for the open $\Sigma 11$ GB, which might be expected to behave similarly to our open $\Sigma 5$ GB. However, the $\Sigma 11(113)[1\bar{1}0]$ is known to be an atypical GB with not only a very low GB energy but also very small excess volume [127, 128, 153]. This GB is therefore more akin to the $\Sigma 3$ than to the $\Sigma 5$ GB.

In another study, Pedersen et al. [132] used an EMT potential fitted to DFT data to investigate the H interaction with different GBs in Al. According to their kinetic Monte Carlo simulations, none of the inspected GBs showed an enhanced H diffusivity. Even though these results have to be taken with caution due to the empirical nature of the EMT potential, this result may be related to a faster H diffusion in bulk Al. Because Al has a larger lattice parameter than Ni, H prefers to occupy tetrahedral interstitial sites in Al, and the migration barrier for H in Al is only half of that in Ni [98]. The migration energies within the GB plane reported by Pedersen et al. [132] are similar to our values for the $\Sigma 5$ GB, but due to faster bulk diffusion the H diffusivities at the GBs are not enhanced but rather impeded.

This outcome may be common to other fcc metals with high bulk diffusivities as well as to bcc metals, where the H diffusion is generally very fast. In order to corroborate this hypothesis, additional investigations are necessary, but a partial confirmation can be given considering the cases of fcc Pd and bcc Fe. Pd has a low bulk migration energy of about 0.2 eV [22], and GBs were found to impede H diffusion [154] as in the case of Al. H in bcc Fe has a very low energy barrier for bulk migration, and also in this case no diffusion enhancement was observed [134].

3.3.4   Diffusivity in a polycrystalline microstructure

The diffusivities of H at the two GBs as estimated in the previous section are only valid locally. Although they give a clear picture of how GBs influence the H transport, this is not equivalent to a description of H transport in polycrystalline materials. To this end the approach based on TST used in Chapter 2 is not applicable since the system is not homogeneous, i.e. the diffusion coefficient depends on the position in the system: it is bulk-like for the interior of the grains, and it changes in the vicinity of the GBs. Nevertheless the diffusion can be described as usual by an effective diffusion coefficient that "averages" all the different local diffusivities.

In this section we want to discuss briefly the issue of calculating an effective diffusivity in a polycrystalline material and the influences of GB connectivity and GB distribution. For this purpose a widely used approach [134, 155] is the KMC method [156]. The KMC is an efficient method to carry out dynamical simulation of stochastic and thermally-activated processes at the atomic scale. This method does not consider any details of atomic interactions but instead explores the dynamic between well defined states, which correspond to particular atomic arrangement. The direct treatment of the state-to-state transitions allows to cover much longer time than molecular-dynamic simulations. In the investigated physical systems, typically there is a large separation of time scales between the thermal vibrations of the atoms and the microscopic migration processes (jumps), which can be termed as rare event. For this reason atomistic methods that simulate directly thermally activated process, such as molecular dynamic simulations, are inefficient for studying diffusion. The KMC method integrates out the effect of the fast thermal vibrations of the atoms on microscopic rates and considers only the processes which change the atomic configuration. From this point of view the KMC can be seen as a coarse-graining in time. The crucial input for KMC is the knowledge of all possible events along with their transition probabilities. In case of interstitial diffusion, this means that it is necessary to find *a priori* all possible jumps mechanisms, i, with the relative probabilities to occur, Γ_i. This input can be extracted from atomistic calculations.

The main steps of a KMC algorithm are the following:

- The cumulative function is calculated as: $R_i = \sum_{j=1}^{i} \Gamma_j$ for $i = 1, \ldots, N$, where N is the total number of processes.

- A particular process, i, is selected according to: $R_{i-1} < \rho_1 R_N \leq R_i$, where ρ_1 is a random number between 0 and 1.

- The selected process is executed, i.e. the configuration of the system is changed.

- The time, t, is updated according to $t = t - \Gamma_N \ln(\rho_2)$, where ρ_2 is a second random number between 0 and 1.

The diffusivity can be then computed according to Eq. 2.5 and these steps are repeated until it converges.

To illustrate how the effective diffusion coefficient depends on the material characteristics, we have applied the KMC to a toy model representing a polycrystalline microstructure which is shown in Fig. 3.7. This is a simple 2-D square lattice with periodic boundary conditions where the diffusing H atoms are non-interacting, i.e. in the dilute limit. Each lattice site can be one of three types: bulk-like (in white), $\Sigma 5$-like (in black) and $\Sigma 3$-like (in red). All jump rate between those sites are equal to an arbitrary unit (arb. unit), with the exceptions of the black-black jump rate which is hundred time faster (100 arb. units), and the rate of jumps from and to any black site which is two time slower (0.01 arb. unit). These definitions mimic a polycrystalline Ni samples with fast and slow diffusion GBs according with the results obtained for the $\Sigma 3$ and the $\Sigma 5$ GBs. We considered three cases with different distributions of the GB-like sites, but with the same grain size. The first, in Fig. 3.7a, is the case where there are only fast diffusion GBs. The effective diffusion coefficient in this case is 10 arb. units, which is lower than that for diffusion along the GBs, but faster than the bulk diffusion. This means that in this case the overall diffusion is enhanced by the presence of the GBs. The second and third cases are illustrated in Fig. 3.7b and 3.7c. In both models 33% of the GBs are of the slow-diffusion type. In case two, the fast diffusion paths are not long-range connected and, hence, the effective diffusivity drops to the bulk value. The case three represents the other extreme situation in which the fast diffusion paths are all connected. In this case the obtained effective diffusivity is similar to that obtained in the case one where were only fast GBs are present.

This toy model is clearly oversimplified. But it illustrates the feature that the effective macroscopic diffusion in a polycrystalline material depends strongly on the microstructure.
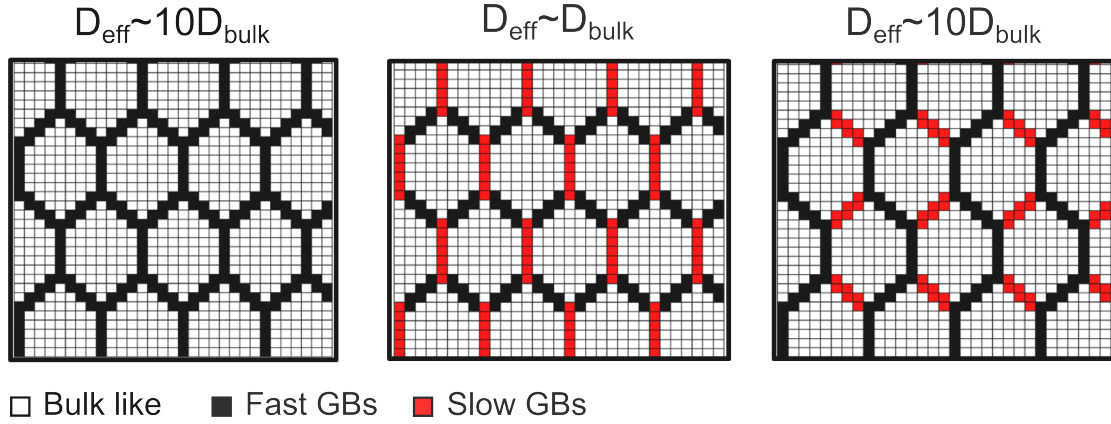
FIGURE 3.7: Toy model of a polycrystalline material.

To perform quantitative calculations of effective diffusion coefficients for realistic models of polycrystalline microstructure is a very challenging task which is hard to complete even with KMC. In this case, the main advantages of KMC, the coarse-graining of time, is lost. When atomic diffusion in defective systems, like polycrystals, is considered, the presence of multiple migration mechanisms with different occurrence rates introduces additional time-scale separations, due to the different jump rates in the bulk grains or at GBs. If these separations are large the KMC will spend most of the time sampling the faster processes, like molecular dynamics. Moreover to model materials with extended defects, larger lattice sizes are necessary. But KMC simulations in 2-D are limited to about 500x500 nm^2 [157], while the typical grain diameters in polycrystalline nickel can be of the order of hundreds of μm [39, 124].

A possible solution to the problem is to employ a multiscale approach, as proposed in the MultiHy project, cf. Sec. 1.3, where the KMC method is used to link the diffusion rates calculated by means of DFT with a continuum description of H diffusion in macroscopic systems, where Fick's two laws, cf. Sec. 2.2, are solved by means of finite element methods (FEMs). This approach is illustrated in Fig. 3.8. In FEM the computational domain is subdivided into smaller subdomains, called finite elements. Each of them contains the proper local physical characteristics which describes the problem (in case of diffusion essentially it is needed to specify the diffusion coefficient). The diffusion coefficient for the bulk-like elements (in light blue in Fig. 3.8) is straightforwardly that for bulk Ni calculated using, for instance, TST or the other methods presented in Chapter 2. The diffusion coefficient for the GB-like elements needs to be calculated as an effective properties. In FEM the region which describes the GB, has always a finite thickness d, cf. Fig. 3.8, of the order of few nanometers. In atomistic models the GB thickness

can be approximated as d_{GB}, see Fig. 3.8. Therefore it is necessary to calculate an effective diffusion coefficient for a supercell of size d containing an array of parallel planar GBs, so that the obtained diffusing value can be used in the FEM for the GB elements (for instance those in dark blue in Fig. 3.8). In this case the atomistic system to consider is relatively small and the effective coefficient can be calculated easily with KMC simulations, but, because of the simplicity of the geometry (parallel straight grain boundaries) the problem can even be solved analytically. It has been shown [158, 159] that a bulk containing parallel grain boundaries behaves as a homogeneous system with an effective diffusivity given by the simple rule-of-mixture formula:

$$D_{eff} = (1 - f_{GB})D_{bulk} + f_{GB}D_{GB} \tag{3.6}$$

where D_{bulk} and D_{GB} are the diffusion coefficients in the bulk and in the GB respectively, and f_{GB} is the volume fraction of GBs, which can be calculate from the parameter d_{GB}, see Fig. 3.8.
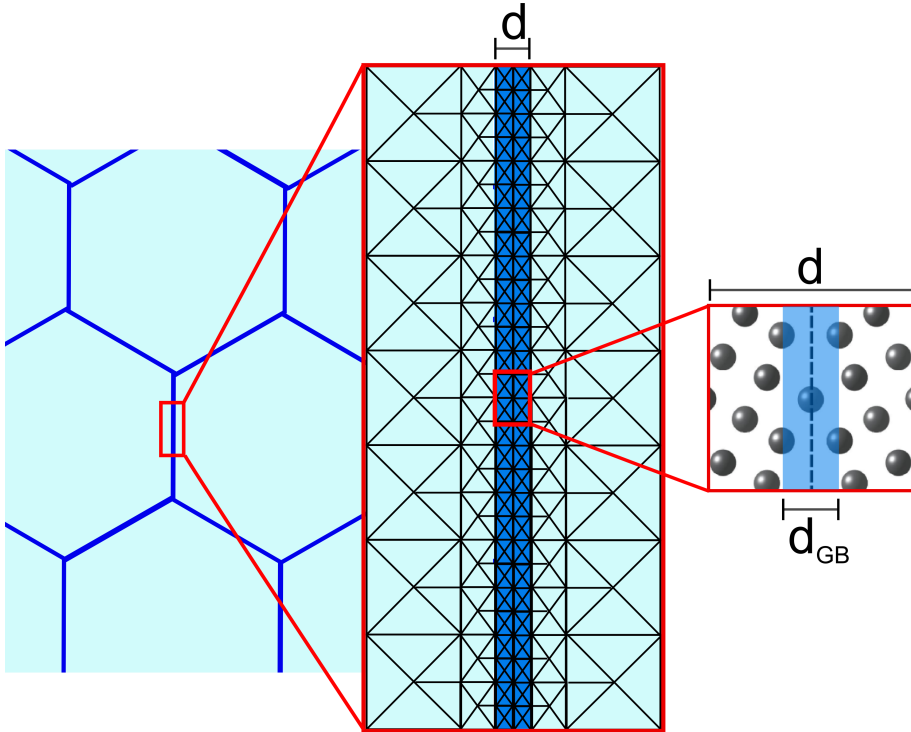

FIGURE 3.8: Illustrative representation of the proposed multiscale approach to describe H diffusion in polycrystalline materials from the atomic scale to the continuum level.

3.4 Concentration of H at GBs

In this section we discuss the problem to determine the local concentrations of H that can be reached at GBs in Ni for experimentally found concentrations for bulk Ni. The results presented in the previous section indicate that the $\Sigma 3$ STGB does not act as a trap for H, and therefore it is not considered in this section.

3.4.1 Computational details

All calculations were carried out using the Quantum Espresso PWscf code [160] which uses a plane-wave basis to represent the wave functions of the valence electrons. Interactions of ionic cores and valence electrons were described by ultrasoft pseudopotentials. The PBE generalized gradient approximation was used for exchange-correlation [64, 144]. All calculations were carried out as spin-polarized. This time we used the smaller, not rectangular supercell shown in Fig. 3.2 and a Monkhorst-Pack k-point mesh of $8 \times 8 \times 2$.

In this supercell we have gradually increased the H content at the GB. We started with a H atom at the most stable position, see Sec. 3.3, and then introduced additional H atoms subsequently. In order to find the most stable configuration for each H content, several arrangements of the interstitial atoms were considered. Due to computational resources, only a rather small number of configurations were explored. The capability of the GB to trap H atoms can be quantified by the GB interface excess energy calculated as:

$$E_N^{ex} = \frac{E_{N_H} - E_0 - N_H \frac{1}{2} E_{H_2}}{A} \tag{3.7}$$

where E_{N_H} is the total energy of supercell containing N_H H atoms, E_0 is the total energy of the same supercell without H, and E_{H_2} is the energy of an isolated H_2 molecule. Note that the GB interface excess energy is essentially the solution energy of H, Eq. 3.4, normalized by the interfacial area of the interface. Another important quantity to consider is the incremental segregation energy, which is defined as:

$$E_{N_H}^{seg} = E_{N_H} - E_{(N_H-1)} - E_{bulk}^{seg} \tag{3.8}$$

where E^{seg}_{bulk} is the segregation energy of a dilute H atom in bulk Ni. Negative values of $E^{seg}_{N_H}$ indicate that it is energetically favorable for the N_H-th atom to segregate at the GB where $N_H - 1$ atoms were already trapped, than to be in the bulk interior of a grain.

To estimate the concentration of H at the GB as function of the bulk concentration at finite temperature, it is important to take the entropy into account. For simplicity, we only include configurational entropy, which is the most important contribution [133, 161]. To this end, we followed the thermodynamic Langmuir-McLean model [162]. In this model the mean H concentration at the grain boundary, c_{GB} can be expressed as function of the bulk H concentration, c_{bulk}, as:

$$\frac{c_{GB}}{1 - c_{GB}} = \frac{c_{bulk}}{1 - c_{bulk}} e^{-E^{seg}(c_{GB})/kT} \tag{3.9}$$

where $E^{seg}(c_{GB})$ is the segregation energy as function of the H concentration at the GB, which can be defined as $c_{GB} = N_H/N_H^{max}$ with N_H^{max} is the maximum number of H that can be trapped efficiently. By definition c_{GB} takes continuum values from 0 (no H atoms trapped) to 1 (N_H^{max} H atoms trapped). Note that Eq. 3.9 slightly differs from the original Langmuir-McLean model where the segregation energy is assumed to be constant.

3.4.2   Results

The obtained set of GB structures with different numbers of H atoms is shown in Fig. 3.9. One can see that with increasing number of H atoms the excess of volume increases in the direction orthogonal to the interface. The lateral dimensions are only slightly distorted (by at most 1 %).

In Fig. 3.10, the calculated GB interface excess energy (left panel) and the incremental segregation energy (right panel) indicate that the maximum number of H atoms that can be accommodated at the considered GB is five.

By interpolating the incremental segregation energy in the range from zero to five segregated H atoms, it is possible to obtain $E^{seg}(c_{GB})$, which is needed to evaluate Eq. 3.9. This interpolation has been carried out using a cubic spline method with special care that for $N_H < 1$ the $E^{seg}(c_{GB})$ takes the constant value of -0.23 eV, which has been obtained for dilute H at this GB, cf. Table 3.2.
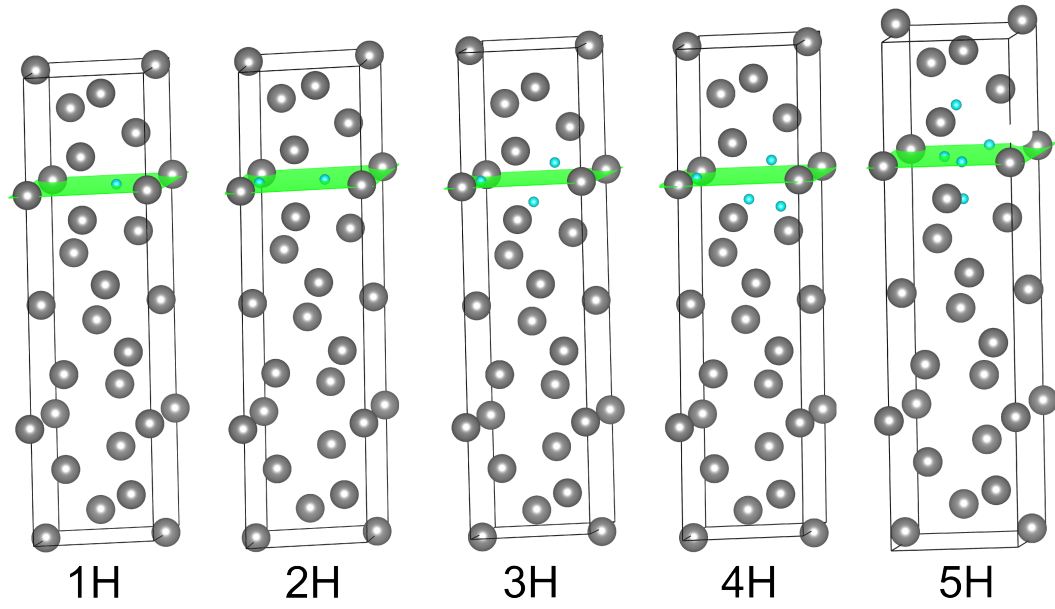
FIGURE 3.9: Relaxed supercells of Σ5 GBs with different H occupations of the cavity. Grey and light blue spheres are Ni and H atoms, respectively. The GB plane is highlighted in green.
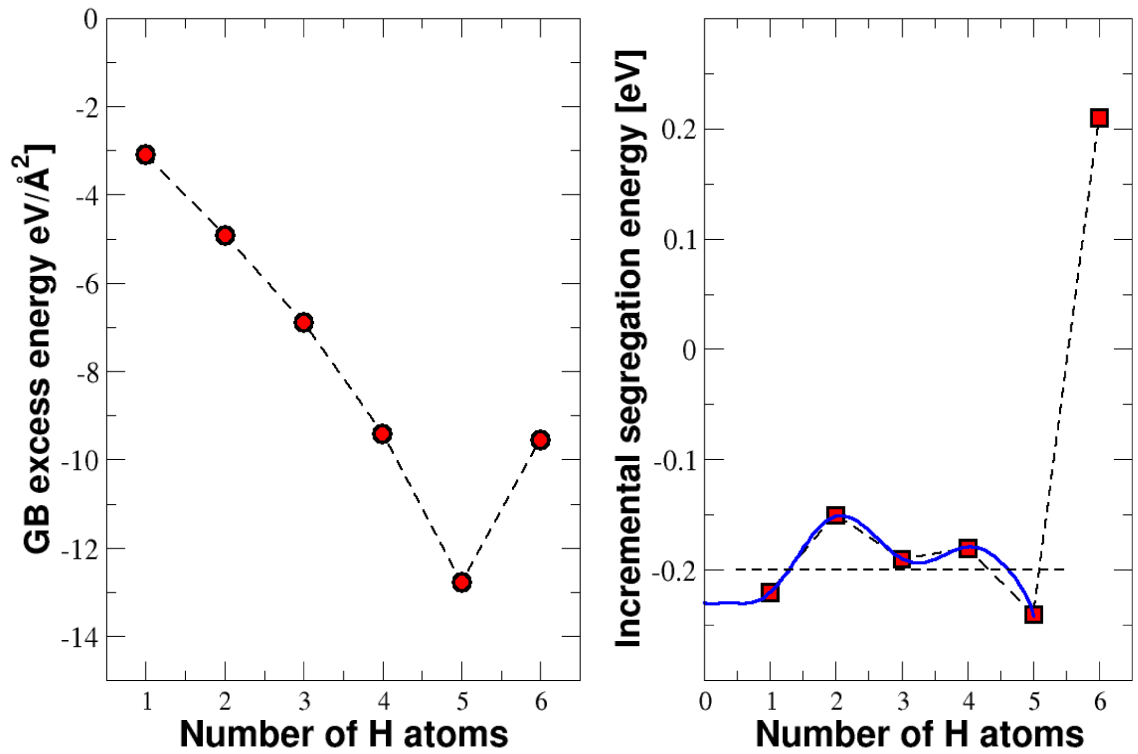

FIGURE 3.10: GB excess energy (left panel) and segregation energy (right panel) as function of the number of H atoms in the Σ5 GB cavity obtained according to Eqs. 3.7 and 3.8, respectively.

Eq. 3.9 can be solved numerically using the spline interpolation for $E^{seg}(c_{GB})$. The H concentration at the GB as function of the H concentration in the bulk interior at room temperature is shown in Fig. 3.11 as the solid blue curve. The c_{gb} becomes discontinuous for $N_H = 2$. This behavior of the c_{gb} is not due to the spline interpolation but rather to the feature that $E^{seg}(c_{GB})$ is not monotonic with a maximum at $N_H = 2$. In a similar computational study Yamaguchi et al. [163] have used the average incremental segregation energy in Eq. 3.9. For comparison the value obtained with this approach is reported as well in Fig. 3.11. The two curves are not dramatically different, therefore the following discussion of the results is not strongly influenced by which curve one considers.
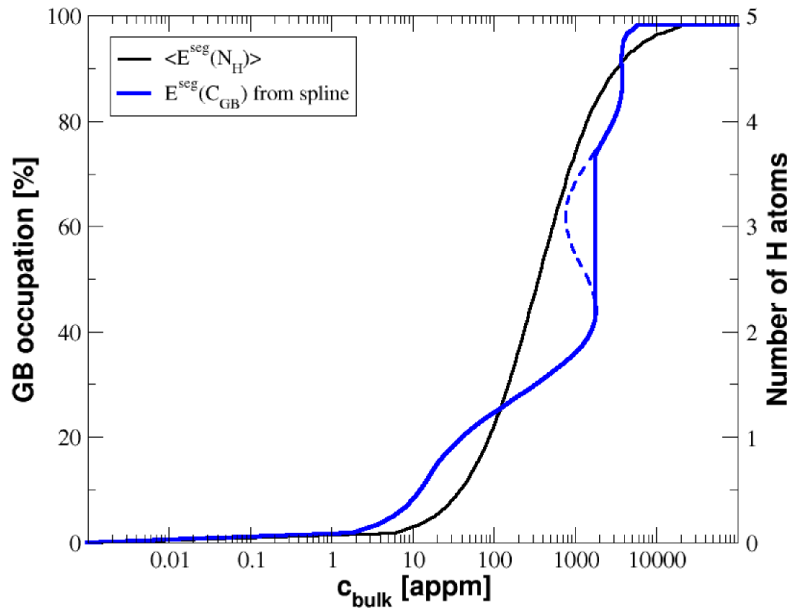

FIGURE 3.11: H occupancy of the $\Sigma 5$ STGB at room temperature as function of H bulk concentration. The black and blue curves are obtained according to Eq. 3.9 parametrized with the interpolation of the incremental segregation energy and the mean incremental segregation energy, see Fig. 3.10, respectively.

3.4.3 Discussion

The knowledge of the amount of H that can segregate at GBs as function of the bulk concentration is a crucial information for modeling H-induced intergranular fracture. Moreover one should bear in mind that the bulk H concentration is a macroscopically quantity which can be quantitatively measured, whereas the intergranular one calls for microscopic measurements.

In order to answer the question of how much H can be segregated at GBs at finite

temperature, we linked ab-initio results with a thermodynamic model based on the the Langmuir-McLean one.

By means of ab-initio simulations, we calculated the GB excess energy and the incremental segregation energy as function of the number of segregated H atoms, Fig. 3.10. These two quantities indicate that a maximum of 5 H atoms can be trapped simultaneously inside the cavity at the $\Sigma 5$ STGB. The obtained results are in qualitatively good agreement with what found for Ni vacancies [164], where it is energetically favorable to trap up to six H atoms, and with similar calculation performed for an Al GB, which can trap six H atoms as well [163].

Whereas the obtained maximum number of H atoms at the GB as obtained from ab-initio calculations is only valid at $T = 0$ K, a thermodynamical model is needed to estimate the H concentration at finite temperature. The Langmuir-McLean model, Eq. 3.9, allows us to estimate the relation between bulk and GB concentrations of H. The isotherm for a temperature of $T = 300$ K is shown in Fig. 3.11. It suggests that for experimentally reasonable bulk concentrations (up to 3000 atomic ppm [124]), a maximum content of about four H atoms per cavity can be established for the considered $\Sigma 5$ GB. This content corresponds to a homogeneous GB coverage of about 0.3 H atoms per Å^2. This value is remarkably high with respect to the density of Ni at this GB which is 0.07 atoms per Å^2. One is tempted to think that the H concentration is overestimated because of the approximations employed to obtain it, but it is rather the opposite. First, the obtained excess and the segregation energies should be considered cautiously as upper limits of the "true" ones since only a limited number of configurations were taken into account. This means that improvements of the modeling of the trapping behavior of the GB can only lower the obtained segregation energies and therefore increase the concentration of H at the GB. Second, and most important, an approximation was to neglect any effects due to the kinetics of migrating H atoms. Fast diffusion of H along certain GBs or H transport by dislocation can strongly affect the H distribution. However also these further mechanisms can only increase the H concentration at the GB [33].

As last point we want to discuss the discontinuity of the c_{GB} when a non-constant incremental segregation energy is considered. This discontinuous behavior is due to the non-monotonicity of the incremental segregation energy and indicates a phase separation [165]. Note that a similar behavior was observed [166] for Nb segregation at stacking faults in a Co-0.96 at.% Nb alloy and was associated with

the observation of formation of 2-D Nb-enriched structures at the stacking faults. Since recently it was proposed [139, 167] that Ni nanohydride phases may be stable in the vicinity of crack tips and dislocations, this issue is worth to be further investigated.

Recalling the analysis done in the previous section, regarding the structure and the interaction with dilute H of the Σ5 GB we expect that the results obtained here for the Σ5 GB model are qualitatively valid also for other open-structure GBs.

3.5   Effects of H on the cohesion of GBs

In this section we investigate the effects of H atoms trapped at the Σ5 GB on the its cohesion.
Although, there is a general consensus [23, 26, 33, 133, 168] that the presence of H atom can lower the cohesion of GBs, several doubts exist about the magnitude of this reduction as function of the hydrogen concentration in a particular type of grain boundaries. In this section we investigate the effects of segregated H on the Σ5 GB. As in the Sec. 3.4 we do not consider the Σ3 GB because it does not act as a trap for H.

3.5.1   Computational details

We used the same supercell size and computational setup as in Sec. 3.4. Additionally, in order to investigate size effects a second GB supercell containing twice as many atomic (210) planes has been build, see inset of Fig 3.14. The Brillouin-zone integrals were calculated on $8 \times 8 \times 2$ and $8 \times 8 \times 1$ Monkhorst-Pack grids, for the small and larger supercells, respectively. Atom positions were relaxed until the residual forces acting on the atoms were less than 10^{-3} eV/Å. The supercell sizes were relaxed as well.
In order to investigate the effects of segregated H at GBs on the cohesion, it is common procedure [23, 26, 133, 168] to calculate the ideal work of separation, W_{sep}. The W_{sep} as function of the number of H atoms segregated at the GB is defined as:

$$W_{sep} = \frac{E_{N_H}^{GB} - E_{N_H}^{2FS}}{2A} \tag{3.10}$$

where $E_{N_H}^{GB}$ is the total energy of the GB supercell containing N_H atoms and $E_{N_H}^{2FS}$ is the total energy of the fractured state with the N_H H atoms distributed on the two created free surfaces.

The calculation of the work of separation is straightforward, but it requires *a priori* the knowledge of the fracture plane. Moreover it gives information only about the thermodynamic of the decohesion (Griffith criterion) which is not sufficient alone to describe properly fracture processes [169, 170].

In order to obtain more information about the dynamic of the fracture process, we performed so-called computational tensile tests (CTTs) [168, 170–172]. In this type of calculations, tensile strain is slowly introduced by elongating the supercell lengths normal to the GB, which is assigned in the following as z, until the system fractures.

At each step, z was elongated incrementally by 2% of the initial length, z_0. The atomic configuration was uniformly scaled from the fully relaxed configuration obtained in the preceding step and then relaxed again. For simplicity the lateral dimensions x and y of the supercell were kept fixed to the values in the unstrained condition, i.e. any Poisson's contraction was neglected. The response of the system to the applied strain, $s = z/z_0$, is characterized by the strain energy, $E_{strain}(s)$, which is defined as:

$$E_{strain}(s) = E_{tot}(s) - E_{tot}(0) \tag{3.11}$$

where $E_{tot}(s)$ and $E_{tot}(0)$ are the total energies of the elongated and initial supercells. An illustrative example of such a strain energy curve is shown as full black line in Fig. 3.12. By definition, at zero strain the strain energy is minimum. As the strain increases E_{strain} increases as well. At strain level S_1, the corresponding energy is two times the work of separation multiplied by the interface area, A. This implies that for this strain the "cleaved" and the elongated states are energetically equivalent. For larger strain, the "cleaved" state becomes more favorable, but an energy barrier still separates it from the elongated state. The critical strain S_2 corresponds to the maximum elongation that the system can withstand before any infinitesimal fluctuations would lead to spontaneous decohesion. The energy at this strain level, $E_{strain}(S_2)$, is the maximum amount of

elastic energy which can be stored in the system before failure and therefore is also indicated as ideal toughness (when divided by the interface area) and can be related to crack initiation [170]. Unfortunately, this quantity is size dependent, in particular it decreases as the number of atomic planes along the z direction increases, i.e. the obtained value depends on the choice of the supercell. Nevertheless, it is possible to calculate the reduction of the ideal toughness induced by the presence of atomic H. When the same supercell containing H atoms at the GB is considered, the strain energy will change, for instance as the red solid curve in Fig. 3.12. From this one and the black curve is it possible to calculate the reduction of ideal toughness as the ratio between the maximum energies of the GB containing H, $E_{strain}(S_2')$, and of the clean GB, $E_{strain}(S_2)$. This quantity is not effected by the choice of the supercell as it is shown in the next section.
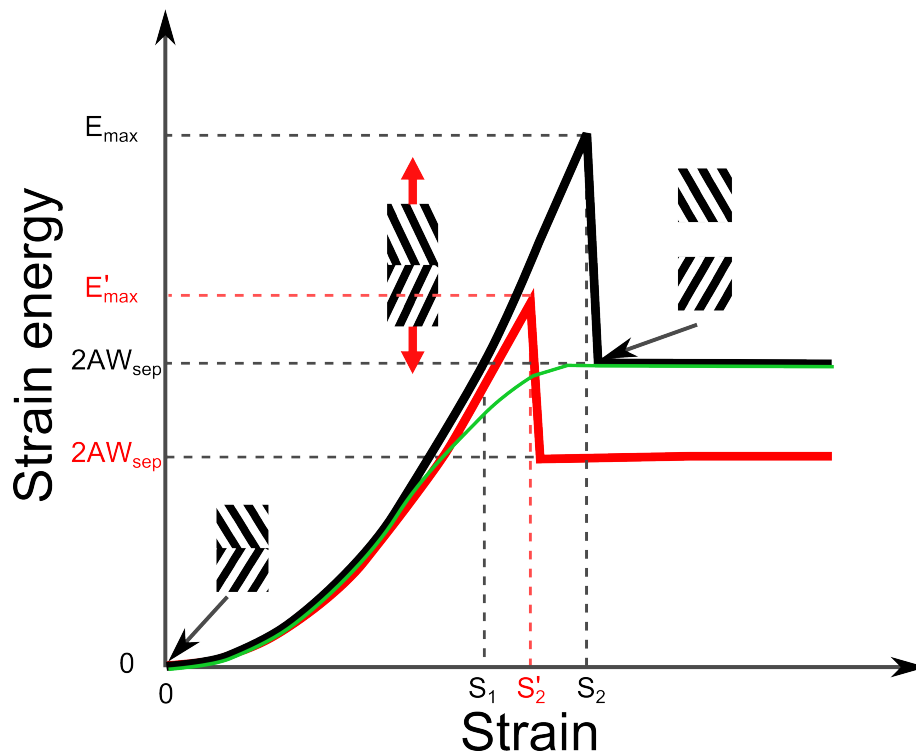
FIGURE 3.12: Schematic representation of typical strain energy curves as function of the applied strain. The solid black and red curve represent the results when atomic relaxation at each elongation step is allowed, while the green thin curve is the tipical results if atomic relaxation is neglected.

Another important information that can be extracted from the CTTs is the ideal tensile strength, which correspond to the maximum stress before fracture occurs, $\sigma(S_2)$.

Note that in several studies [169, 173, 174], because of the high computational

cost, the CTT is performed neglecting atomic relaxation. In this case the typical strain energy curve resembles the thin green line shown in Fig. 3.12, and it is called "universal binding energy relationship" (UBER) [169, 172]. It is obvious that with this procedure all the information about the ideal toughness of the system is lost.

3.5.2 Results

Work of separation as function of the H concentration

First we calculated the work of separation as function of the H content in the $\Sigma 5$ GB. The obtained results are shown in Fig. 3.13. According with the results obtained in Sec. 3.4, we considered a maximum of four H atoms at the GB. The obtained curve is linear over the range considered in agreement with previous findings for Fe and Cu [163]. Our results indicate that the work of separation is reduced up to almost 50% by the segregation of H.
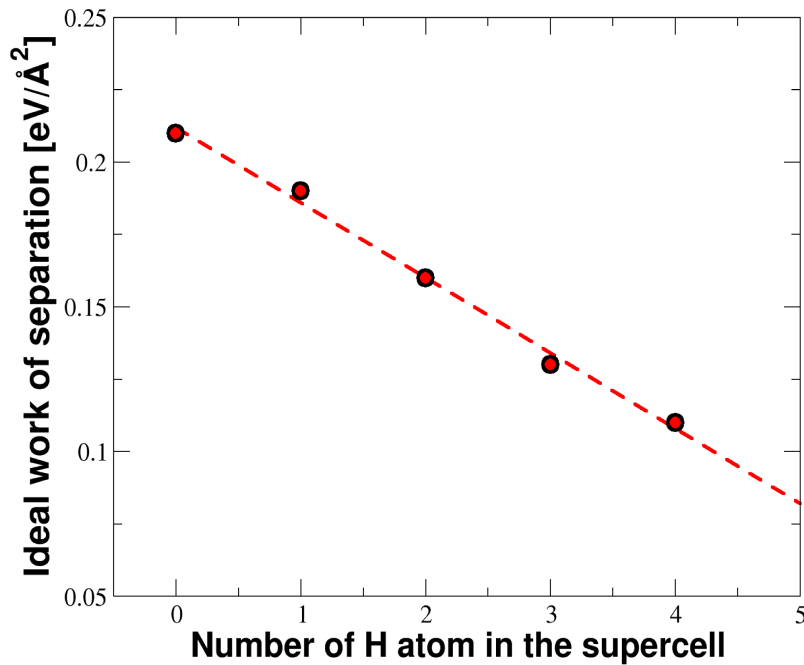

FIGURE 3.13: Ideal work of separation for different numbers of H atoms segregated in the considered supercell, red circles. The linear dependency of the W_{sep} on the H content is highlighted by the red dashed line

Computational tensile test: size dependency

To show that the reduction in the maximum strain energy is a size independent quantity, we performed CTT calculations using the two supercells with different sizes. The first supercell is the one used in Sec. 3.4, and the second is a supercell where the number of atomic planes in the z direction is doubled, while the dimensions orthogonal to z is kept fixed, Fig. 3.14. The strain energies normalized by the number of planes along z for these two system are shown in Fig 3.14. Up to the critical point the two curves are essentially indistinguishable. This indicates that the strain energy scales with the number of planes. Therefore, if the same supercell for a GB with and without H is used the ratio of the strain energies is size independent.
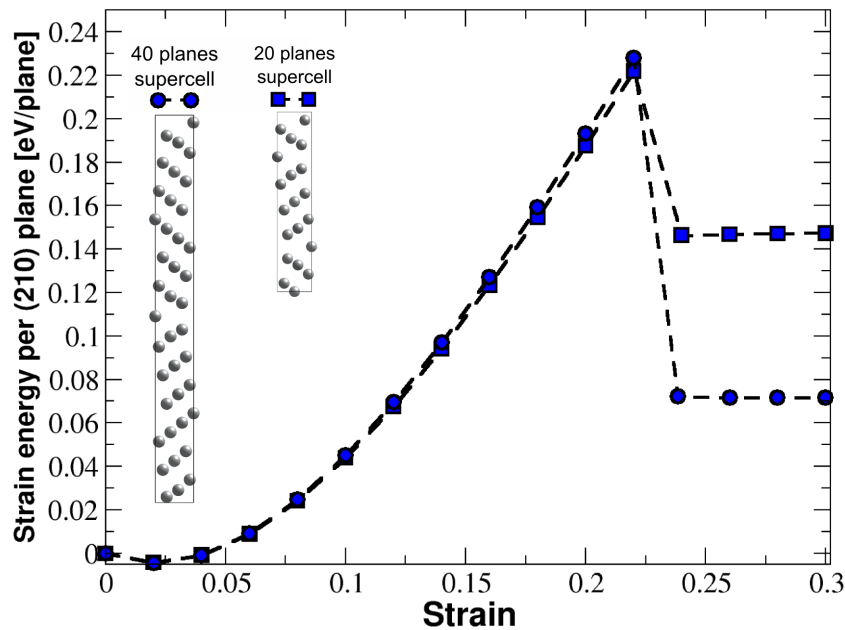

FIGURE 3.14: Strain energy per (210) planes. The two used supercell are also reported.

Note that after the fracture the two curves are not equivalent because the energy plateaus correspond to the work of separation (multiplied by the interface area) which does not scale as the number of planes since it is a size independent quantity.

Computational tensile test: one and two H cases

Using the smaller supercell, we performed tensile tests of the configurations containing one and two H atoms, Fig. 3.8. The strain energies as function of strain are shown in Fig. 3.15. For comparison the results obtained for the clean GB are also reported. The results indicate that when H atoms are segregated the maximum
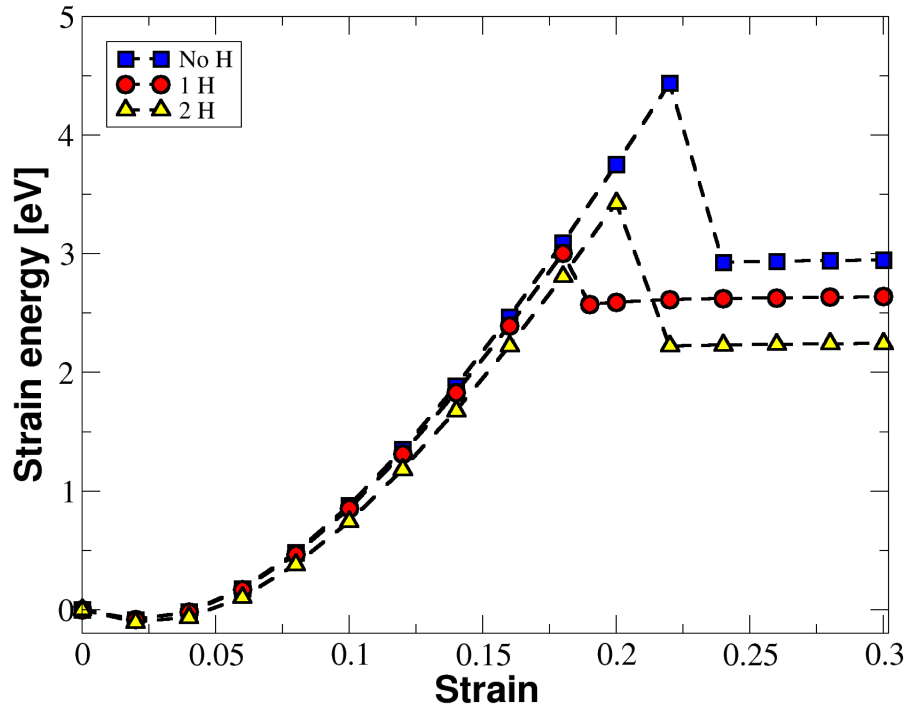
FIGURE 3.15: Strain energy for the GB with: no H (blue squares), one H (red circles), and two H (yellow trinagles).

strain energy is reduced as expected. But surprisingly the reduction is higher for one H than for two H at the GB. This results is consistent with the reduction of ideal tensile strength, maximum stress, as one can see see in the stress-strain curves displayed in Fig 3.16.

3.5.3 Discussion

The ideal work of separation was calculated for the Σ5 STGB with various H contents. The results indicate that it is reduced by the presence of H and that the magnitude of this reduction depends linearly on the H content. For the maximum amount of H considered (4 H atoms in the considered supercell) the reduction of
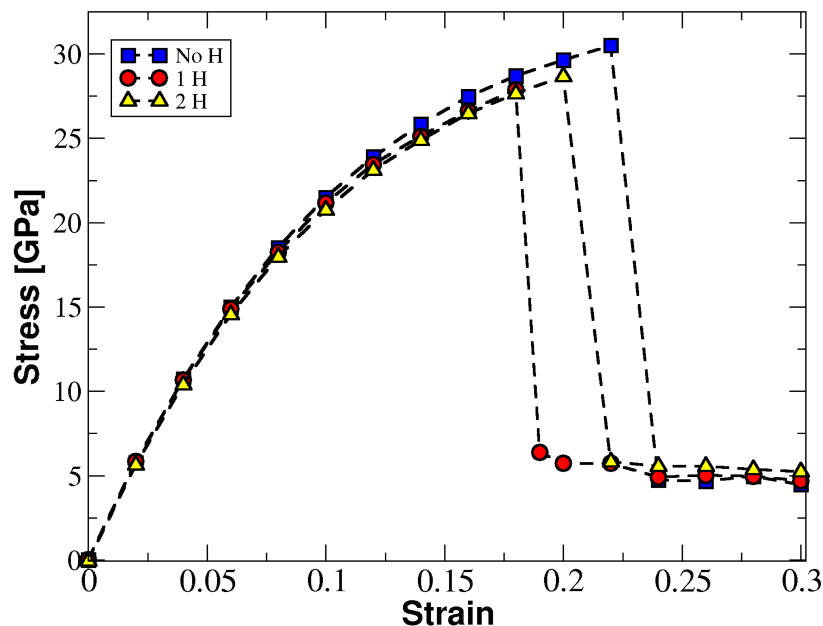
FIGURE 3.16: Stress-strain curves for the GB with: no H (blue squares), one H (red circles), and two H (yellow trinagles)

the work of separation is of almost 50% with respect to the clean case. This reduction is remarkably high and corresponds to a reduction of about 70% of the Griffith parameter. Based on Griffith fracture criterion, Shen et al. [133] have estimated that for the same reduction of the work of separation crack propagating along GBs in Al without dislocation emission are expected. However, to have such an amount of H segregated at the stacking fault it requires a bulk H concentration of about 2000-3000 atomic ppm is required. Such a concentration is reachable only in extreme experimental conditions [124, 126]. But it is unlikely in technological applications, where the typical bulk H concentration is at most few hundreds of atomic ppm. In this case the reduction of the work of separation is about 10-15% which is not enough to cause purely brittle fracture. Nevertheless, as we already pointed out, other factors such as enhanced H diffusion at GB or plasticity can have a critical impact on the H concentration at GBs. Based on these results, we can only conclude that a pure brittle crack growth along an open-structure GBs is not unreasonable, and that this hypothesis can be confirmed only by a more precise estimation of the maximum H content at the GB.

Similar computational studies for other elemental metals and other grain boundary types, report similar conclusions. Dadfarnia et al. [35] reported a reduction of 15% of the work of separation due to H for a $\Sigma3(111)$ grain boundary in Fe. Shen et al. [133] found for a $\Sigma9(221)$ GB in Al that the maximum reduction of the

work of separation was at most 25%. Contrarily, Yamaguchi et al. [168] reported a reduction of the work of separation of 40% for a Σ3(111) GB in Fe, and 90% for a Σ5(012) GBs in Al. The results are apparently inconsistent, but one should consider the for both metals, Yamaguchi et al. have considered six times the amount of H used by Dadfarnia et al. and Shen et al.

In addition to the calculation of the work of separation the reduction of ideal toughness and the reduction of ideal strength due to one and two H segregated H were computed by means of computational tensile tests. The obtained results, Fig. 3.15, are rather unexpected. The segregation of one and two H atoms causes an outstanding reduction of the ideal toughness of about 33% and 23 % with respect to the clean GB, respectively. But it is surprising that the reduction is stronger for the configuration with less H atoms. Similar results were found for the ideal tensile strength, which is reduced by 10% and 7% in case of one or two segregated H atoms, respectively. In order to provide an explanation for these observations we analyzed the electron density in the system. We compared the total electron density minus the density of non-interacting H atoms in the cases of no H, one H, and two H. The cross sections along (001) of the obtained densities are reported in Fig. 3.17 for the initial relaxed states (upper panels) and for the critical states just before the fracture (lower panels). Two different color scales have been used, one for the initial state and another for the critical states, this is due to the fact that the density of the critical states is lower since the systems are elongated.

From the plots of the electron density, it is possible to see a reduction of the density between the Ni atoms labeled as "A" and "B", which indicates a softening of the interfacial Ni-Ni bonds. The effects seems to be stronger as more H is segregated. It is also evident, especially from the plot of the electron density of the critical states, that there is a charge accumulation both at the H atom and between H and its neighboring Ni atoms. This is particularly evident from the case of two H at the critical state, where the density is higher at the H-Ni bond than between the neighboring Ni atoms A and B. These observations suggest that there is a redistribution of charge from the Ni-Ni bond to the H and between H and Ni, which indicate the formation of a Ni-H bond. This is in agreement to other theoretical investigations [26, 175], which have found that the H acts as an electron acceptor and binds to the metal atoms. In the light of that, we think that the trends in the reduction of both ideal toughness and ideal tensile strength are due
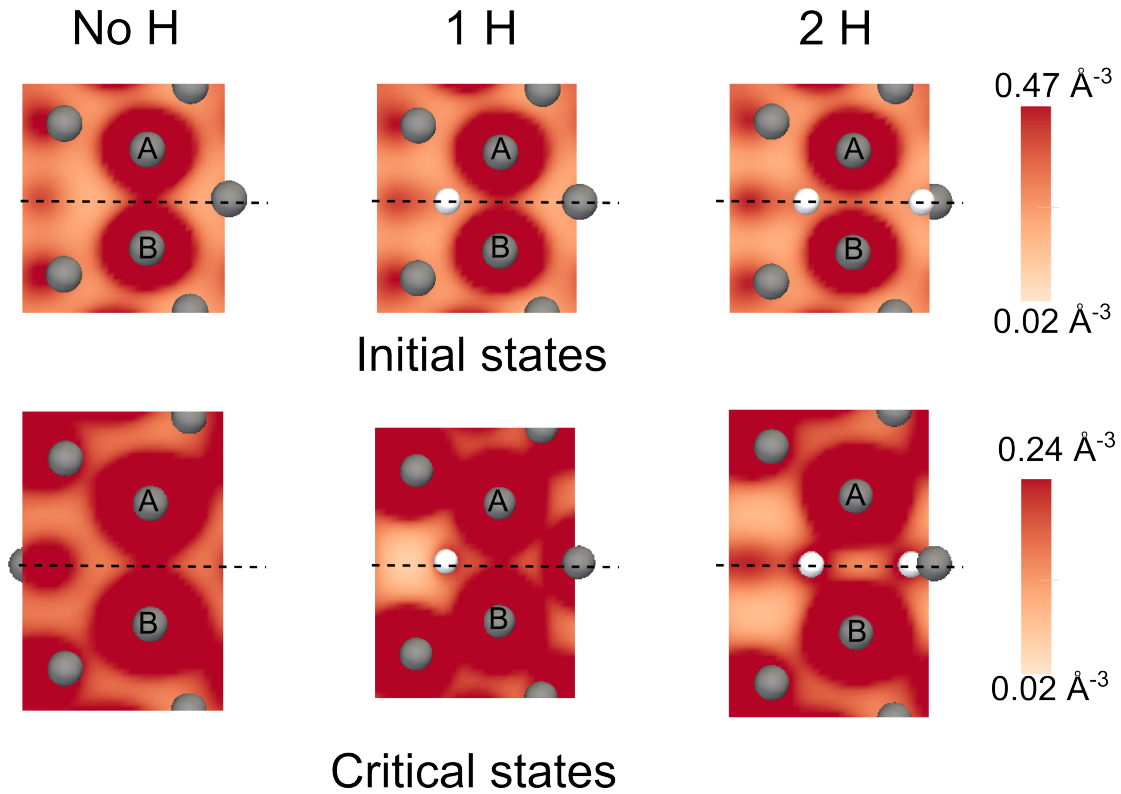
FIGURE 3.17: Cross section along (001) of the total valence electron density minus the density of non-interacring H atoms at Σ5 GB at the plane orthogonal to the GB plane and crossing the Ni atoms labeled as "A" and "B". The upper and the lower panels are for the the inital relaxed and the critical states, respectively. The grey and white spheres indicate the Ni and H atoms, respectively, and the dashed line marks the GB plane. Dark red color indicates regions of highest density.

to competing effects of H on the GB cohesion. On the one hand the H lowers the Ni-Ni bond by drawing electronic charge away, on the other hand it tends to form H-Ni bonds which hold together the two grains. In case of one or two segregated H atoms the first effects is the dominating one, but with two segregated H the bonding effect becomes more important because two H form more bonds which seems to be stronger. Additional investigation are needed to corroborate this suggested explanation

3.6 Conclusions

([121], Sec. 5)

In this chapter we investigated three important aspects of the interaction between H and grain boundaries in Ni: how the transport of H is influenced by the presence of GBs, how much hydrogen can be accumulated at GBs, and how hydrogen atoms influence the cohesion properties of GBs. Two model GBs, $\Sigma3(111)[\bar{1}10]$ and $\Sigma5(210)[001]$, were selected and their interfacial atomic and electronic structures thoroughly analyzed. Based on comparisons with available literature data, we presume that the chosen GBs can be considered as representatives for a larger variety of GB types.

First we have considered H in the dilute limit and investigated both its segregation at various interstitial sites in the vicinity of the GBs and its migration towards and along the GBs. The key results are:

1. The trapping of H and migration depend strongly on the GB character.

2. The $\Sigma3$ STGB does not trap H atoms and acts as a two-dimensional obstacle for H diffusion.

3. The $\Sigma5$ STGB acts as an effective two-dimensional sink for H atoms, but provides fast migration channels along the GB plane where H can diffuse about two orders of magnitude faster than in bulk Ni.

Additionally we emphasized the need for a multiscale simulations in order to describe quantitatively the H diffusion in polycrystalline metals, and we proposed a possible approach to link atomistic data to a continuum (macroscale) description of H diffusion.

In the second part of the chapter we focused on the effects of H on the grain boundary cohesion. To this end, we first estimated the amount of H which can realistically accumulate at GBs. This was done by parametrizing a thermodynamic Langmuir-McLean model with the H segregation energy calculated as function of the H concentration. Since the $\Sigma3$ STGB does not act as a trap for H, in this case we considered only the $\Sigma5$ STGB.

Our results show that under severe experimental conditions (very high bulk concentration of H) a large amount of H can actually segregate at GBs, while in more

realistic conditions the mean interfacial H concentration is noticeably lower.

Once H concentration at GBs is known, it is possible to investigate how this influences the GB cohesion. The calculation of the work of separation reveals that a strong reduction of the GBs cohesion is possible (up to about 50%) just for a high content of H at the GBs. In addition to that, we have performed computational tensile tests for different H concentrations. The results thereof are that the ideal toughness is reduced up to 33% even at very low H concentration. In this case as the concentrations this reduction apparently decreases. This rather surprising phenomenon was related to two different H effects. On the one side H reduces the strength of Ni-Ni bonds by acting as an electron acceptor. On the other side it creates itself relatively strong bonds with the neighboring Ni atoms which tend to keep linked the two grains during the fracture.

In the next chapter we address another type of extended defects, namely titanium carbide precipitates in Fe. This type of defects is considered to be important in case of hydrogen embrittlement of steel, where GBs play a less important role.

Chapter 4

Interaction of H with TiC precipitates in iron

After having considered the interaction of H with grain boundaries, in this chapter we investigate the interaction of H with another type of defects, namely, carbide precipitates in bcc Fe. Such heterogeneous systems are particularly important because they are characteristic elements of the microstructure of steels for which engineering problems caused by H embrittlement are critical.

4.1   Introduction

As already motivated in the introduction of this thesis, there is a growing interest in the use of high strength steels (HSS) for structural applications. HSS have the potential to withstand higher stresses than normal steels, and that allows to reduce the weight of structural components while maintaining the same stiffness and strength. Unfortunately, the susceptibility of a steel to hydrogen embrittlement increases with its strength [10, 11]. Therefore, detailed research on the effect of hydrogen on the mechanical behavior of HSS is necessary.

In case of HSS, HE occurs even at very low H concentrations. It is not uncommon to have perceptible H-induced degradation effects for concentrations of only few tens of atomic ppm. Since such low concentrations are practically unavoidable

during production and service, the most promising strategy to improve the resistance of HSS to HE is to render H innocuous. This can be achieved by introducing effective traps for H [41]. As we have already said, a common characteristic of all proposed HE mechanisms is the need to establish a critical H concentration at the location of damage. This cannot happen if H is not free to diffuse into/through the metal lattice.

Some studies [176, 177] reported that HSS containing large amounts of fine carbide and nitride precipitates have a lower susceptibility to HE. It is assumed that these precipitates produce a number of deep trapping sites for hydrogen [36, 178–180] and hence increase the resistance of the steel against HE [176, 181]. However, there are still open questions regarding the nature of these trapping sites and their effectiveness in immobilizing H. To answer these questions experimentally is rather difficult because the most common techniques, such as thermal desorption spectroscopy [178–180, 182, 183] or permeation [183, 184], are indirect measurements of traps properties. Thus the obtained results require interpretation which is not always straightforward [182, 183, 185]. Atomistic simulations can help to determine the trap characteristics, but there is still a lack of theoretical investigations on this topic. The aim of this work is to contribute to fill this gap. In this chapter, we report our systematic study of the interaction between H and TiC precipitates in Fe. The structure of the chapter is the following. In Sec. 4.2 we present the modeling approach we have used. In Sec. 4.3 we give the computational details. In Sec. 4.4 the obtained results are reported. In Sec. 4.5 the results are discussed in detail and compared with experimental data.

4.2   Theoretical approach

The system consisting of a transition-metal carbide particle in the matrix of bcc Fe is rather complex to model. Both the morphology and the size of transition-metal carbides precipitated in steels can vary significantly depending on composition and manufacturing conditions (e.g., thermal treatment) [36, 178, 179, 186–188]. Furthermore, the carbides are often sub-stoichiometric, containing a large amount of C vacancies. Because of this complexity, simulations of the whole particle at the atomic scale are impracticable. To overcome this problem we therefore considered independently the interaction of H with bulk TiC (both perfect and

with C vacancies) and with various representative interfaces between TiC particle and Fe matrix.

Small TiC nuclei are expected to be fully coherent with the bcc Fe matrix [179]. The preferential growth occurs along the {100} planes of bcc Fe and the particles adopt the so-called Baker-Nutting (B-N) orientation relationship (OR) with $(001)_{\text{Fe}}||(001)_{\text{TiC}}$ and $[100]_{\text{Fe}}||[110]_{\text{TiC}}$ [179]. As the precipitates grow, they take a typical shape of thin platelets where misfit dislocations form on the broad $(001)_{\text{Fe}}/(001)_{\text{TiC}}$ interface when the particle diameter exceeds about 4 nm [178, 179]. The lateral interfaces are often round with a tendency to facet along the $\{100\}_{\text{Fe}}$ and $\{110\}_{\text{Fe}}$ planes. Larger particles become ellipsoidal and form less coherent interfaces due to deviations from the exact B-N OR. A detailed experimental analysis of TiC precipitates in steels can be found in the papers of Wei et al. [178, 179] and references therein.

For our atomistic simulations, the coherent interfaces are the easiest ones to model. They are characterized by a perfect coincidence of atomic planes across the interface, where the eventual lattice mismatch is accommodated by elastic expansion/compression of one or both phases. These systems can be therefore represented by relatively small, periodically repeated supercell models (see below).

In the case of semicoherent interfaces, the elastic energy needed to make the interface coherent becomes prohibitively large and it is more favorable to form an array of misfit dislocations to release the accumulated elastic stress. The spacing between the misfit dislocations, which generally depends on the lattice mismatch and elastic properties of the two materials, is typically of the order of several nanometers. This clearly increases enormously the computational costs, since a full model of such a semicoherent interface requires thousands of atoms [189, 190]. Fortunately, the semicoherent interface can be well approximated as being composed of broad coherent regions that are periodically interrupted by relative narrow regions containing the misfit dislocation cores [189], as shown schematically in Fig. 4.1. The atomic structure of a misfit dislocation core can again be represented using a small supercell, albeit in this case the long range elastic strain field of the dislocation is neglected.
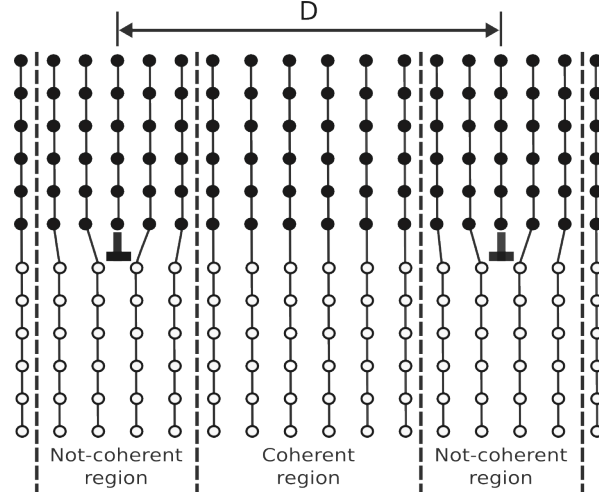
FIGURE 4.1: Schematic representation of the semicoherent interface

In the case of general interfaces [127], here also referred to as incoherent interfaces, i.e., interfaces with more distorted atomic structures that lacks a well-defined periodicity, the variability of possible supercell models is large. In this work, we investigated the $(110)_{\text{Fe}}/(001)_{\text{TiC}}$ interface as well as several defective interfaces (containing C vacancies) as representative models for general (incoherent) interfaces. A detailed description of these interfaces is given in the next section.

To characterize the stability of an interface, it is possible to calculate the interface energy defined as:

$$\gamma_{int} = \left[E_{tot}(Fe_x/Ti_yC_y) - E_{tot}(Fe_x^{bulk}) - E_{tot}(Ti_yC_y^{bulk}) \right]/2A \qquad (4.1)$$

where $E_{tot}(Fe_x/Ti_yC_y)$ is the total energy of supercell containing the investigated interface configuration, while $E_{tot}(Fe_x^{bulk})$ and $E_{tot}(Ti_yC_y^{bulk})$ are the total energies of supercells containing the two bulk phases with the same numbers of atoms as in the interface supercell. A is the interfacial area, and the factor 2 in the denominator takes into account that there are two equivalent interfaces in the supercell.

To characterize the energetics associated with H trapping, we adopt a nomenclature displayed in Fig. 4.2. The solution energy of an isolated interstitial H atom
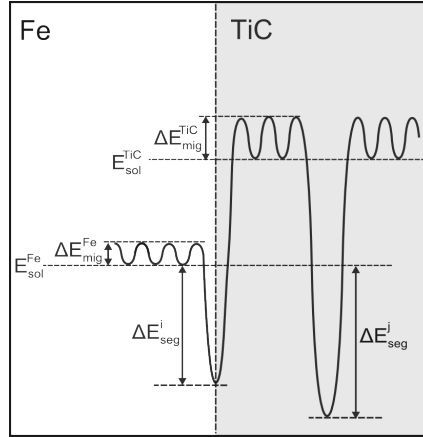
FIGURE 4.2: Schematic picture of energetics associated with H trapping at the Fe/TiC interfaces and in the interior of TiC precipitates.

inside a perfect bulk Fe crystal, E_{sol}^{Fe}, is taken as the zero energy reference state.

The segregation energy of H in a trap i is then given as:

$$\Delta E_{seg}^i = E_{tot}^i(H) - E_{tot}^i(0) - (E_{tot}^{Fe_{bulk}}(H) - E_{tot}^{Fe_{bulk}}(0)) \tag{4.2}$$

where $E_{tot}^i(H)$ and $E_{tot}^i(0)$ are the total energies of the system containing the trap i with and without H, respectively, while $E_{tot}^{Fe_{bulk}}(H)$ and $E_{tot}^{Fe_{bulk}}(0)$ are the total energies of a bulk Fe crystal supercell with and without H, respectively. With this definition, negative values of E_{seg}^i indicate that the considered site is energetically more favorable than H in bulk Fe.

The energy barriers for H migration in Fe and TiC, ΔE_{mig}^{Fe} and ΔE_{mig}^{TiC}, respectively, are considered to be equal to their bulk values (see below), unless noted otherwise.

We can also define a trap escape energy, which is the energy needed for H to escape from a trap i to bulk Fe, either as

$$\Delta E_{esc}^i = E_{seg}^i + \Delta E_{mig}^{Fe} \tag{4.3}$$

if H is trapped at the Fe/TiC interface, or as

$$\Delta E_{esc}^i = E_{seg}^i + E_{sol}^{TiC} + \Delta E_{mig}^{TiC} \tag{4.4}$$

if the considered trap is in the interior of the carbide.

4.3 Computational details

All DFT calculations were carried out using the Vienna Ab-initio Simulation Package (VASP) [142, 143, 191]. The generalized gradient approximation (GGA) in the form given by Perdew, Burke and Ernzerhof [64] was employed for exchange-correlation. Ultrasoft pseudopotentials [144] were used for the core-valence interactions. All calculations were carried out as spin-polarized. Energy cutoffs of 300 eV for the plane-wave basis were found to yield converged total energies within an accuracy of 10^{-5} eV. The Brillouin zone was sampled using Monkhorst-Pack grids with various k-point densities (see below). Atom positions were relaxed until the residual forces acting on the atoms were less than 10^{-3} eV/Å and the total energy was converged to 10^{-5} eV. The DFT calculations for this chapter were done at the computer center of the Karlsruher Institut für Technologie together with Dr. Matous Mrovec. As was shown in Chapter 2, the inclusion of quantum-mechanical effects is crucial for a correct description of H diffusion in bcc Fe. But in the case of H trapping, these effects do not affect significantly the escape rate of H from a trap. From Fig. 4.2 one can see that the energy path to escape a trap is rather similar to that to diffuse in Ni, for which we have shown that quantum-mechanical effects are not critical, see Sec. 2.5.3.

4.4 Results

4.4.1 Bulk phases

The fundamental properties of the individual bulk phases are summarized in Table 4.1. The most stable interstitial sites for dilute hydrogen in bcc iron are the tetrahedral sites (T-sites) [96, 97, 116]. The obtained solution energy of H in a 2x2x2 Fe supercell $Fe_{16}H$ is E_{sol}^{Fe} =0.05 eV. Since its calculation depends on the choice of the H chemical potential, we have set this quantity to zero as reference state for the interface system. The migration barrier for H in bcc Fe has been calculated in Chap. 5 to be ΔE_{mig}^{Fe} =0.09 eV (without quantum corrections, cf. Sec 2.5.2). TiC crystallizes in the cubic NaCl structure which can be seen as an fcc Ti sublattice where every interstitial octahedral site is occupied by a C atom. Consequently, in perfect stoichiometric TiC the interstitial H atoms can only occupy the tetrahedral sites of the fcc Ti sublattice. Our calculated solution energy

	a	B	C_{11}	C_{12}	C_{44}	E_{sol}	ΔE_{mig}
Fe	2.858	175	258	133	94	0.00	0.09
TiC	4.342	248	508	118	168	0.94	0.19

TABLE 4.1: Fundamental properties of the bulk phases: lattice parameter a [Å], elastic constants in GPa (taken from Ref. [186]), and solution and migration energies in eV. Note that the reported migration energy for H in bulk Fe is the classical one (cf. Sec. Sec 2.5.2), and the migration energy for H in bulk TiC is the one for the easiest path
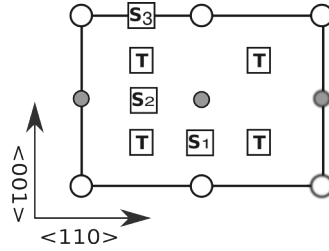

FIGURE 4.3: Atomic structure in the 110 plane of bulk TiC with marked tetrahedral (T) and saddle point (S_{1-3}) sites.

Path	ΔE_{mig}^{TiC} [eV]
S_1	0.53
S_2	0.19
S_3	0.29

TABLE 4.2: Migration energies for H in bulk TiC corresponding to the three saddle points shown in Fig. 4.3

of H in 2x2x2 cubic TiC supercell (Ti$_{32}$C$_{32}$) amounts to E_{sol}^{TiC} =0.94 eV, which is in good agreement with the value of 0.97 eV obtained by Ding et al. [192].

The migration of H between neighboring tetrahedral sites in TiC can proceed via three different saddle point configurations, as illustrated in Fig. 4.3. The shortest pathway, lying along the $< 100 >$ directions, is associated with two migration barriers of 0.19 and 0.29 eV corresponding to saddle points S_2 and S_3, respectively. A much greater migration barrier of 0.53 eV exists for a jump over the saddle point S_1 along the $< 110 >$ direction. Since the path over the saddle point S_2 percolate all the crystal, this value has been chosen as characteristic for the migration of H in bulk TiC.

4.4.2 Coherent and semi-coherent interfaces

Based on experimental observations [36, 179], we focused primarily on the Baker-Nutting OR, (001)$_{Fe}$/(001)$_{TiC}$, for our calculation of the coherent and semi-coherent

interfaces between bcc Fe and TiC phases. Since the lattice parameters of bcc Fe and TiC are different, see Table 4.1, there is a lattice mismatch between the two crystals. This lattice mismatch is accommodated by setting the initial lateral cell vectors of the used supercell to those of a unit cell of TiC, which is the stiffer phase (cf. Table 4.1), in the B-N orientation. Even when the mutual orientation of the two crystals is fixed, there is still one geometrical degree of freedom left, namely, the relative translation of the two crystals parallel and perpendicular to the interface plane.

We investigated three highly symmetric translation states, illustrated in Fig. 4.4, which we designate as (i) Fe-on-C configuration, where the Fe atoms are on top of C atoms; (ii) Fe-on-Ti configuration, where the Fe atoms are on top of Ti atoms; and (iii) bridge configuration, where Fe atoms have two C atoms and two Ti atoms as nearest neighbors.

For the calculations we employed a supercell composed of 5 Fe layers, each containing one Fe atom, and 5 layers of TiC, each containing one C atom and one Ti atom. For this supercell a 10x10x2 k-point mesh was used for the Brillouin-zone integration. The supercells obtained after complete relaxation (cell vectors and atomic positions) are shown in Fig. 4.5 and the obtained geometrical parameters are summarized in Table 4.3.
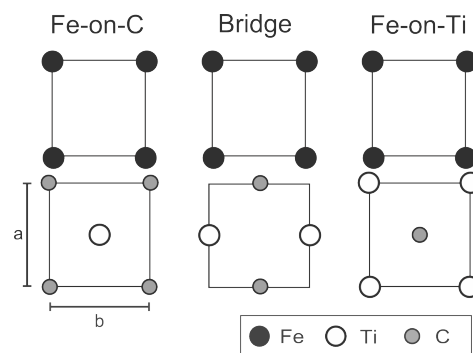
FIGURE 4.4: Schematic representation of three investigated translation state for the $(001)_{Fe}/(001)_{TiC}$ interface obtained by different relative shifts of the two crystals. Top and bottom panels represent the $(001)_{Fe}$ and the $(001)_{TiC}$ interface planes, respectively.

In all three cases, the lattice vectors parallel to the interface are close to that of bulk TiC (3.06 Å). This confirms that the bi-axial stress due to the mismatch is mainly accommodated by the stretching of the Fe matrix, (by about 6.6%). As described in pages 145 and 146 of Ref [193], the lattice mismatch can be used to estimate the distance, $D = 4.6$ nm, between two misfit dislocations (see Fig. 4.1)

FIGURE 4.5: Atomic structure for the supercells representing the three possible configurations of the $(001)_{Fe}/(001)_{TiC}$ interface, see Fig. 4.4, after complete relaxation of all degree of freedom. Black, grey, and white spheres represent Fe, C, and Ti atoms, respectively.
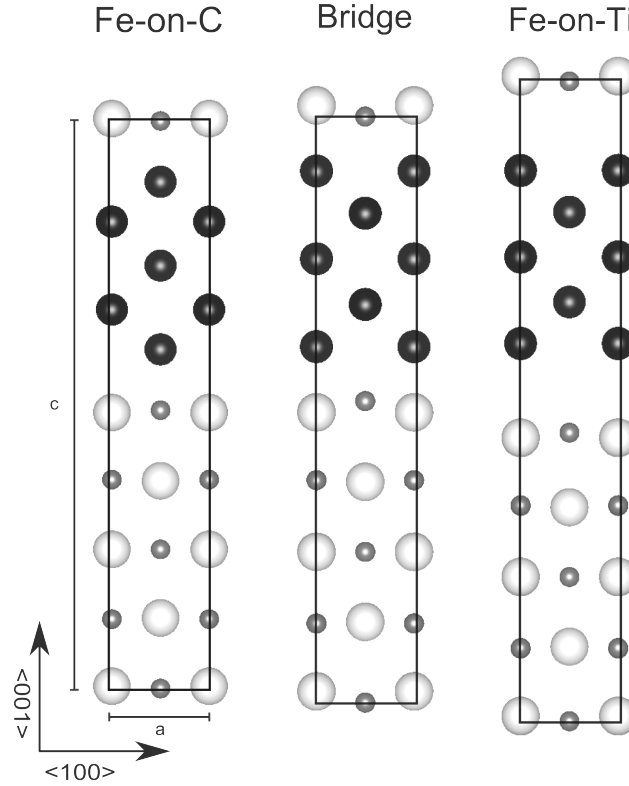
	a [Å]	b [Å]	c [Å]	d_{Fe-Ti} [Å]	γ_{int} [eV/Å^2]
Fe-on-C	3.05	3.05	17.80	1.91	0.16
bridge	3.10	2.98	17.88	1.66	0.34
Fe-on-Ti	3.01	3.01	19.77	2.75	0.57

TABLE 4.3: Supercell dimensions a, b anc c, distance d_{Fe-Ti} along $\langle 100 \rangle$ direction between the Fe and Ti planes across the interface, and interface energy γ_{int}, for the three investigated $(001)_{Fe}/(001)_{TiC}$ configurations.

and a limit for the size of a coherent TiC precipitate.

The calculated interface energies, shown in Table 4.3, indicate that the most stable interface is the Fe-on-C configuration, followed by the bridge and Fe-on-Ti configurations. Therefore, the coherent part of the Fe/TiC interface will most likely correspond to the Fe-on-C configuration. The other two configurations can be related to dislocation cores and their intersections that appear on the semicoherent interface. The dislocation cores consist essentially of an extra Fe plane which will

cause a local shift of Fe with respect to TiC by a half inter-planar spacing along either $\langle 110 \rangle_{Fe}$ or $\langle \bar{1}10 \rangle_{Fe}$ directions. Both these translations result in the bridge configuration which thus resembles the misfit dislocation core. When two perpendicular misfit dislocations along $\langle 110 \rangle_{Fe}$ and $\langle \bar{1}10 \rangle_{Fe}$ intersect, the shifting the two crystals results in the Fe-on-Ti configuration at the intersection of the dislocation cores.

4.4.3 Other interfaces

Experimental studies report that the TiC particles in the Fe matrix can form also interfaces with other ORs, in particular those with $(110)_{Fe}/(001)_{TiC}$ orientation. In this case it is more difficult to find a mutual orientation of the two crystals. We chose the configuration shown in Fig. 4.6. This interface was obtained by
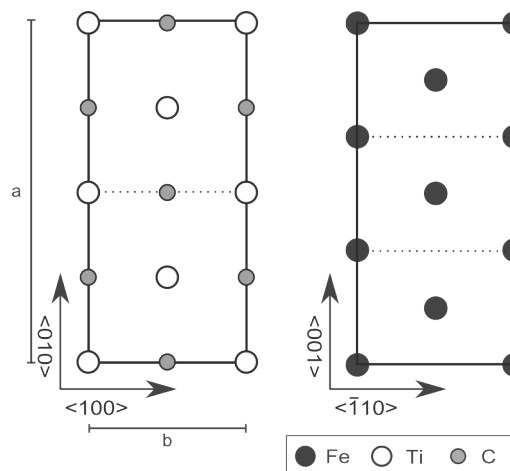
FIGURE 4.6: Schematic representation of the two adjoining Fe and TiC planes across the $(011)_{Fe}/(001)_{TiC}$ interface. Black, grey, and white spheres represent Fe, C, and Ti atoms, respectively.

joining three Fe unit cells with two TiC unit cells. This construction allows for a very small mismatch along the $\langle 010 \rangle_{Fe}$ ($\langle 010 \rangle_{TiC}$) direction of only about 2%, and a still rather small mismatch on the $\langle 1\bar{1}0 \rangle_{Fe}$ ($\langle 100 \rangle_{TiC}$) direction of about 8%. Note that in this case the relative shift of the two crystals with respect to each others by a half Fe inter-planar spacing does not change the interface structure. This interface cannot be considered as coherent because the patterns of atoms at the adjoining planes are very different, cf. Fig. 4.6, and a good match between the two crystals is not possible.

FIGURE 4.7: Atomic structure of the $(011)_{\text{Fe}}/(001)_{\text{TiC}}$ supercell after complete relaxation of all degrees of freedom. Black, grey, and white sphere represent Fe, C, and Ti atoms, respectively.

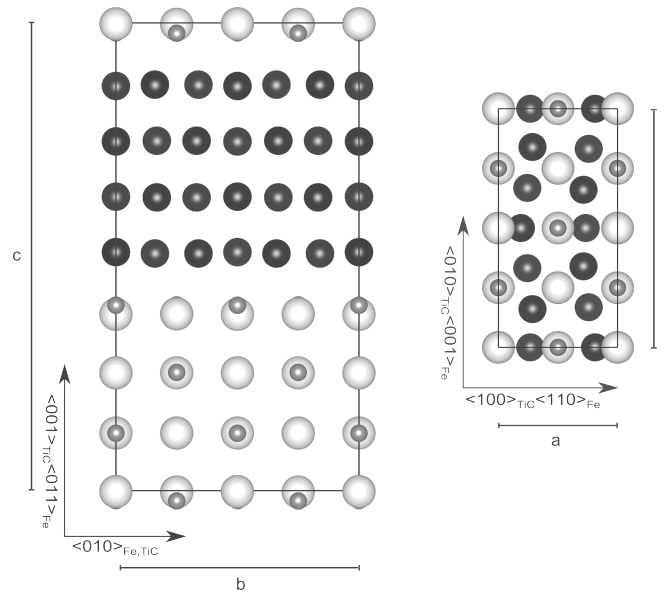The supercell used to model this interface consisted of four Fe planes, each containing 6 Fe atoms, and 4 TiC planes, each containing 4 Ti and 4 C atoms. The Brillouin zone integration was done on a 10x5x2 k-point mesh. As in the case of $(001)_{\text{Fe}}/(001)_{\text{TiC}}$ supercells, we performed a full relaxation of all degrees of freedom. The obtained structure is shown in Fig. 4.7, and the supercell dimensions and the interface energy are listed in table 4.4. From Fig. 4.7 one can see that the poor match between the two interfaces results in a large distortion of the interfacial planes of the two crystals. As in the interface considered in the previous section, the lattice mismatch between the two crystal structures is mainly accommodated by an expansion of the Fe crystal only.

a [Å]	b [Å]	c [Å]	d_{Fe-C} [Å]	d_{Fe-Ti} [Å]	γ_{int} [eV/Å^2]
4.279	8.588	16.558	1.82	2.15	0.15

TABLE 4.4: Supercell dimensions, distances along $\langle 100 \rangle$ direction between the Fe and C planes, and the Fe an Ti planes across the interface, and interface energy, for the investigated $(011)_{\text{Fe}}/(001)_{\text{TiC}}$ interface.

4.4.4 Trapping of H at interfaces

Trapping of H at the Baker-Nutting interface

For all the three possible interface configurations (Fe-on-C, bridge, and Fe-on-Ti) described in Sec. 4.4.2, we identified and characterized the possible trap sites for H. These sites were found by: (i) placing a H atom at different high-symmetry positions at the interface and at octahedral-like and tetrahedral-like sites in the Fe plane closest to the interface, and (ii) performing atomic relaxation of the systems. This procedure allows us to individuate the actually stable sites for H.
All the calculations with H were performed using the same supercells as above for the calculations without H (see Fig. 4.5). Although these supercells are rather small, careful test calculations indicated that they are big enough to avoid serious finite-size effects on the segregation energies.
The found stable sites for H at Fe-on-C, bridge, and Fe-on-Ti configurations are shown in Fig. 4.8. Most of the stable sites are not at the interface plane, but at the Fe plane closest to the interface (these sites are marked with green symbols). Only in the Fe-on-Ti configuration there are two sites at the interface (marked in blue and red). Note that most of the stable sites have similar symmetries as octahedral and tetrahedral sites in bulk Fe. For instance in the Fe-on-C configuration, the sites marked with a triangle resemble tetrahedral sites where one vertex of the Fe tetrahedron is replaced with a Ti atom. Similarly the sites marked with squares, pentagons and diamonds have similar symmetry as the octahedral sites in bulk Fe.
Sites at the Fe plane and at the interface plane are labeled as FP_x^y and IP_x^y, respectively. The subscript x indicates the specific site and the superscript y indicates the type of configuration ("A" for Fe-on-C, "B" for bridge, and "C" for Fe-on-Ti).

For all the stable sites, the segregation energies for H, calculated according to Eq. 4.2, are reported in Table 4.5. For the Fe-on-C configuration, the most stable position is the one labeled as FP_3^A with a segregation energy of 0.32 eV. Since, the calculated segregation energy for an H atom at tetrahedral position in bulk Fe, elastically strained in the same way as in the interface supercell, is 0.18 eV, it is possible to conclude that the segregation energy of H at the interfacial site FP_3^A is due to both the different chemical environment and the elastic strain of the Fe lattice. For the bridge and Fe-on-Ti configurations the most stable sites are the FP_4^B and FP_1^C, respectively.
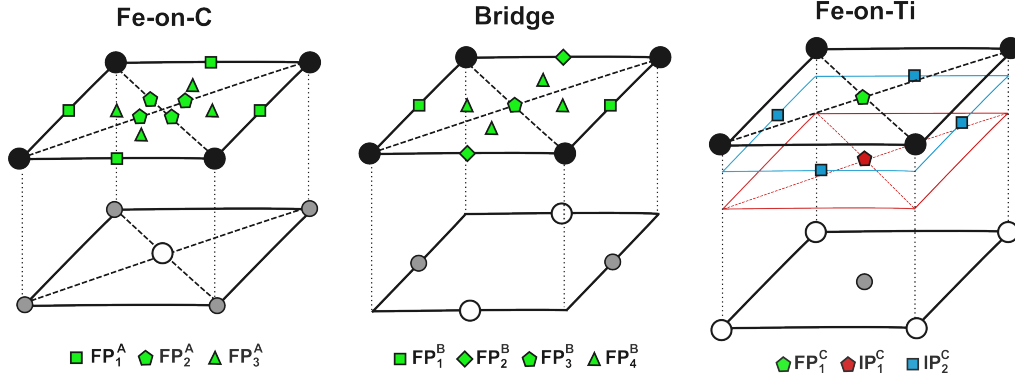
FIGURE 4.8: Schematic representation of the stable positions for H at Fe-on-Ti, bridge, and Fe-on-Ti configurations of the B-N interface. The black, grey, and white circles represent Fe, C, and Ti atoms, respectively. Only one Fe and one TiC planes are displayed.

Fe-on-C (A)		Bridge (B)		Fe-on-Ti (C)	
Site	E_{seg} [eV]	Site	E_{seg} [eV]	Site	E_{seg} [eV]
FP_1^A	-0.30	FP_1^B	-0.23	FP_1^C	-0.50
FP_2^A	-0.16	FP_2^B	-0.20	IP_1^C	-0.42
FP_3^A	-0.32	FP_3^B	-0.08	IP_2^C	-0.40
		FP_4^B	-0.49		

TABLE 4.5: Segregation energies for different stable positions for H at coherent $(001)_{Fe}/(001)_{TiC}$ interface (Fe-on-Ti), and at misfit dislocation cores (Bridge) and their interections (Fe-on-Ti). The label of the sites refers to the positions illustrated in Fig. 4.8

H trapping at $(011)_{Fe}/(001)_{TiC}$

In the case of the $(011)_{Fe}/(001)_{TiC}$ interface, to locate the stable positions for H atoms by symmetry is not straightforward. Because of that we placed an H atom at several different randomly chosen initial positions at the interface plane and relaxed these. In this way three stable positions have been identified. In all cases the H atoms relax through the first Fe layer away from the interface plane. One example structure is shown in Fig. 4.9. The resulting most stable site has a segregation energy of 0.20 eV.

As for the coherent interface we calculated the segregation energy for a H atom in bulk Fe, strained as in the $(011)_{Fe}/(001)_{TiC}$ interface supercell, of 0.14 eV. This

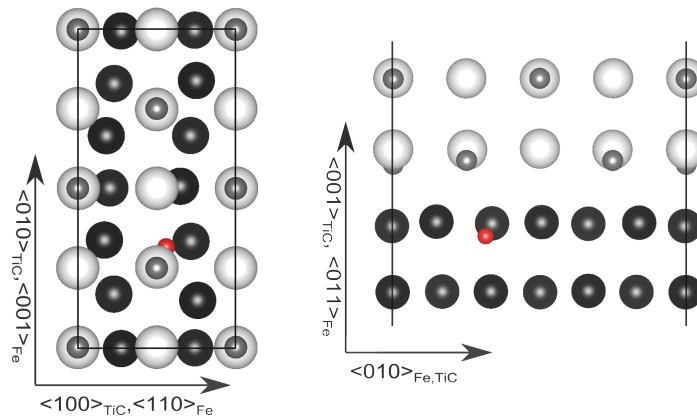indicates that in this case the rather small trapping effect is mainly due to the strain of the Fe lattice.

FIGURE 4.9: One example of the three distinct stable positons for H at the $(110)_{Fe}/(001)_{TiC}$ interface. The H atoms are shown as red sphere. In the left structure only the Fe and TiC planes at the interface are reported.

4.4.5 Interaction of H with C vacancies

Apart from the perfect interfaces, we calculated the trapping properties of C vacancies, at both the $(001)_{Fe}/(001)_{TiC}$ and the $(011)_{Fe}/(001)_{TiC}$ interfaces, and in the interior of the carbide. In all investigated cases the most stable site for H is the center of the C vacancy. This was also found experimentally for TiC [194].

For the $(011)_{Fe}/(001)_{TiC}$ interface, we considered only the most stable the Fe-on-C interface configuration. We investigated three distinct vacancy locations (V_1, V_2, V_3) at different distances from the interface, as illustrated in Fig. 4.10. For these calculations, we employed supercells of the same size in the direction perpendicular to the interface as that in Sec. 4.4.2, but doubled in size along the directions parallel to the interface in order to reduce the interactions between periodic images of the C vacancies and the H atoms.

For the $(011)_{Fe}/(001)_{TiC}$ interface we used the same supercell as in the previous section, and we considered just one vacancy (labeled as V_4) located in the TiC layer directly at the interface.

For both interfaces, the calculated H segregation energies, E_{seg}^{vac}, are listed in Table 4.6. For comparison, we report also the results obtained for a C vacancy in the bulk TiC crystal, using a $Ti_{32}C_{31}$ supercell, V_{bulk}. In this case, we also calculated
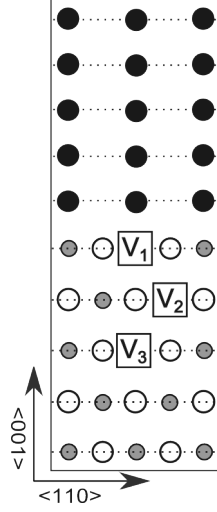
FIGURE 4.10: Illustration of the different C vacancies positions considered in the vicinity of the $(001)_{Fe}/(001)_{TiC}$ coherent interface.

the segregation energy for a C vacancies occupied with two H atoms, V_{bulk}^{2H}.

Site	V_{bulk}	V_{bulk}^{2H}	V_1	V_2	V_3	V_4
E_{seg}^{vac}	-1.02	0.29	-0.49	-0.90	-0.93	-0.92

TABLE 4.6: Segregation energies for H atom at C vacancies at the $(001)_{Fe}/(001)_{TiC}$ and $(110)_{Fe}/(001)_{TiC}$ interfaces, and in bulk TiC (for single and double H occupancy).

Since the amount of C vacancies in TiC can reach up to about 50% (see Sec. 6.1 of Ref. [195]), there is a possibility of an "ordered" distribution of vacancies [196]. Since the calculated migration energy of a C vacancy is very high (4 eV), the vacancies are essentially immobile. Nevertheless, such a high non-stoichiometry may lead to a continuous network of interconnected vacancies, from the interface to the interior of the precipitate. Therefore, we also calculated the energy barrier for H migration between two neighboring vacancies. Our obtained value of 1.19 eV is the same as that reported by Ding et al. [192].

4.4.6 Summary of results

We investigated several distinct H traps associated with TiC precipitates in Fe. These traps include coherent regions as well as misfit dislocation cores at

$(001)_{Fe}/(001)_{TiC}$ and $(011)_{Fe}/(001)_{TiC}$ interfaces, and C vacancies located at the interfaces and in the interior of TiC particles. It is possible to assume that the characteristic segregation energy for each trap source is that of the deepest trap site, i.e., that at reasonable H concentrations only the deepest traps will be occupied. In Table 4.7 we summarize these energies and label the corresponding sites as they will be indicated in the following.

Trap source	Label	E_{seg} [eV]
$(001)_{Fe}/(001)_{TiC}$ coherent int.	$(001)_{int}$	-0.32
$(110)_{Fe}/(001)_{TiC}$ coherent int.	$(110)_{int}$	-0.20
dislocation core at $(001)_{Fe}/(001)_{TiC}$ int.	disl-cores[a]	-0.49
cores intersection at $(001)_{Fe}/(001)_{TiC}$ int.		-0.50
C vacancy at $(001)_{Fe}/(001)_{TiC}$ int.	V-$(001)_{int}$	-0.49
C vacancy at $(110)_{Fe}/(001)_{TiC}$ int.	V-$(110)_{int}$	-0.92
C vacancy in bulk TiC	V_{bulk}	-1.02
2 H in a C vacancy in bulk TiC	V_{bulk}^{2H}	0.29

TABLE 4.7: Characteristic segregation energioes of the investigated traps sources.

[a]Since the segregation energy is almost the same in the following we consider the dislocation cores and their intersections as equal traps sources

4.5 Discussion

4.5.1 Interface structures

For the $(001)_{Fe}/(001)_{TiC}$ interface three different configurations (see Figs. 4.4 and 4.5) were investigated. In all cases, the lattice mismatch between the two crystals is primarily accommodated by a lateral elastic expansion of the Fe crystal (6.6%). These results agree well with those of previous studies by Fors and Wahnström [186], and Kawakami and Matsumiya [197].

The analysis of the interface energies (Table 4.3) reveals that the Fe-on-C configuration is the most stable one. As shown by Fors and Wahnström [186], this is

likely due to strong chemical bonds between Fe and C atoms that are similar to those between Ti and C atoms. Therefore, the interfacial Fe layer acts as a natural extension of the TiC phase. This is not the case for the other two interfaces, and hence those are less stable.

The Fe-on-C configuration has been used to model the coherent interfaces as well as the coherent part of semi-coherent interfaces. The bridge and the Fe-on-Ti configurations correspond to approximate atomic arrangements in a misfit dislocation core and at the intersection of two perpendicular misfit dislocation cores, respectively. By combining the results for the different configurations, it is possible to develop an overall picture of the trapping behavior of H atoms at the semi-coherent interfaces. This requires two main approximations: (i) the semi-coherent interface is considered to be formed by wide section of coherent interface periodically interrupted by narrow misfit dislocation cores, as illustrated in Fig. 4.1, and both regions can be treated separately; (ii) the long-range strain field of the misfit dislocations is neglected and only the dislocation cores and their intersection are considered. These approximations have been proposed and elaborated by the works of, e.g., Benedek et al. [189, 198], Albina et al. [199], Sampath and Janisch [200], and Sawada et al. [190]. In these studies it has been shown that some interface properties, for instance the interface energy, can be estimated as weighted averages of the same properties obtained for different configurations of coherent interfaces, similarly as we did here. This was confirmed by Sawada et al. [190] who performed a direct simulation of a semi-coherent Fe/NbC interface. They found that the local structures of the dislocation cores (and their intersections) indeed resemble well the structure models employed in this work.

From the lattice mismatch between the Fe and TiC at coherent interface, we calculated the maximum size of a fully coherent precipitate to be 4.6 nm. This value corresponds also to the distance between the misfit dislocation in the semi-coherent interface, and agrees well with the experimental value of 4.2 nm reported by Wei and Tsuzaki [178].

Interfaces with the $(011)_{Fe}/(001)_{TiC}$ orientation, were investigated as well. Experimental investigations [178] report that the lateral incoherent sides of the disk-shaped TiC precipitates tend to facet towards the $(011)_{Fe}/(001)_{TiC}$ orientation. In this case, there is no good match between the lattices of the two phases at the interface (cf. Fig. 4.6). This results in a highly distorted semi-coherent interface which cannot be treated as the $(001)_{Fe}/(001)_{TiC}$ semi-coherent interface.

Most likely, it can be seen as a semi-coherent interface where the distortions due to misfit dislocations overlap but the interface is not yet completely incoherent. In this case the obtained interface energy (cf. Table 4.4) is similar to that of the coherent interface. This indicates that the $(011)_{Fe}/(001)_{TiC}$ interface is rather stable and therefore likely to be observed in experimental studies.

4.5.2 Interaction of H with TiC precipitates in Fe

In order to characterize the H trapping properties of TiC precipitates in Fe, we considered both the interfaces and the interior of the precipitate. For each considered case we have obtained a large variety of possible traps. Based on the obtained results, it is possible to construct energy profiles experienced by H atoms around the different types of interfaces (see Fig. 4.11). Note that for each investigated case we assumed that the characteristic segregation energies are those of the deepest traps, as summarized in Table. 4.7.
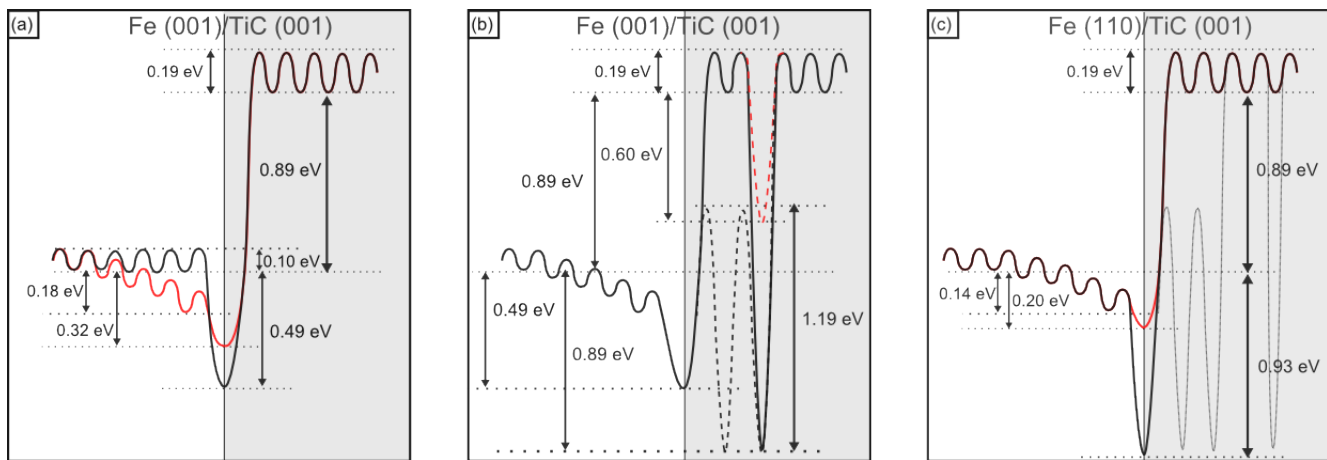
FIGURE 4.11: Energy profiles experienced by an H atoms at: (a) perfect coherent interface (red curve) and dislocation core (black curve); (b) coherent interface with single C vacancies at the interface and in the interior of the carbide (black curve), connected vacancies (dashed black curve), and single C vacancy with double occupancy in the interior of the carbide (red dashed curve); (c) $(110)_{Fe}/(001)_{TiC}$ interface with (black curve) and without (red curve) C vacancies, and with C vacancies in the interior of the carbide (dotted black line).

Fig. 4.11(a) shows the inferred energy profiles across the coherent interface and along the dislocation lines (red and the black curves, respectively). By "dislocation cores" we refer to both dislocation cores and their intersection because they have

almost the same segregation energies for H. Note that according to our calculations about half (0.18 eV) of the segregation energy at the coherent interface is due to the elastic elongation of the Fe crystal. Therefore, we assumed that the energy profile first bends down smoothly to this value as it approaches the interface and then drops down directly at the interface. This does not apply to the case of dislocation cores, where the strain due to the mismatch is released.

The energy profiles in the presence of C vacancies, both at the coherent interface region and in the interior of the precipitate are illustrated in Fig. 4.11(b). The segregation energy for H at the C vacancies at the coherent interface is equal to that for H at the dislocation cores and their intersections, but the energy profile is affected by the elastic expansion of the Fe crystal as in the case of the coherent interface. C vacancies in the interior of the TiC particle provide deep traps. In this case, the trapping effects are enhanced because one should consider that the H needs to pass through the bulk region of TiC in order to leave the precipitate. This entails that it is also more difficult for H to get trapped in these sites. The energy profile in the case of percolating networks of C vacancies is reported in Fig. 4.11(b) as dashed black curve and was estimated from the energy barrier of a H atom migrating between vacancies. In this case, both the trapping depth and the barrier height for H to enter in the traps are markedly reduced. The energy profile resulting from double H occupancy of the C vacancies is shown as the dashed red line. In this case the mutual repulsion between the two H atoms reduces strongly the trapping depth.

In Fig. 4.11(c) the energy profiles around the $(110)_{Fe}/(001)_{TiC}$ interface, both perfect (red dashed curves) and with C vacancies (black full curves), are illustrated. Again, the perfect interface does not offer deep traps while the C vacancies act as strong traps. Since the presence of the interface does not influence much the TiC structure, all results regarding the trapping of H in the interior of the carbide, as presented in Fig. 4.11(b), are valid in this case as well.

Comparison with experiments

Using the DFT data presented in Sec. 4.4, we were able to construct the energy profiles (Fig. 4.11) for various interface configurations. To compare these results with the available experimental data it is useful to relate them with the precipitate size, and to consider the trap escape energy (Eqs. 4.3 and 4.3) instead of the

segregation energy.

Very small precipitates are cube-shaped and all their interfaces are coherent with the $(001)_{Fe}/(001)_{TiC}$ orientation [178]. Because of their small size, we expect them to have a negligible content of C vacancies. Therefore, the only possible trap sites are those due to the coherent interface.

As the precipitate grows, it becomes plate-shaped [178] with two large semi-coherent interfaces with the Backer-Nutting orientation relationship and a narrow lateral interface without strong preferential orientation. Only in few cases [178], the lateral interface is found to be faceted with the $(011)_{Fe}/(001)_{TiC}$ orientation. The C vacancies become more abundant, especially as the particle size increases, i.e., larger volume corresponds to higher probability of having carbon vacancies. From our calculations, the lateral interfaces apparently do not offer deep traps (cf. Fig. 4.11(c)). Moreover since these interfaces are not very extended, they cannot contribute significantly to the trapping. Therefore H atoms should be trapped mainly in the misfit dislocation cores on the large semi-coherent interfaces of the precipitate. This is in agreement with direct experimental observations of deuterium atoms trapped at nano-sized TiC and VC semi-coherent precipitates, performed by Takahashi et al. [37, 201] using atom probe tomography.

Large TiC particles in Fe have an ellipsoidal shape with mostly incoherent interfaces [178]. The size for which the particle becomes incoherent can range from few tens of nanometers to several micrometers depending on the steel composition and manufacturing conditions. Direct first-principles investigations of such incoherent interfaces are not feasible, but some of the obtained results are valid also in this case. In particular, those for the C vacancies in the interior of the TiC particles and for the $(110)_{Fe}/(001)_{TiC}$ interface.

Most of the numerous available experimental studies employ the thermal desorption spectroscopy (TDS). In this experiment, the measured quantity is the desorption activation energy, E_{des}, which does not correspond to the segregation energy but rather to the trap escape energy. Hence, for a quantitative comparison with the experimental results one should consider the trap escape energy, defined in Eqs. 4.3 and 4.4. To obtain the trap escape energy for trap at the coherent interface, both perfect and with vacancies, one should also subtract to the escape energy of Eq. 4.3 the energy gained by the elastic expansion of the Fe matrix, see Fig. 4.11(a). The calculated ΔE_{esc} for the different traps are reported as function of the particle character in Fig. 4.12(a).

In Fig. 4.12(b), the experimental E_{des} are reported as function of the particle size.
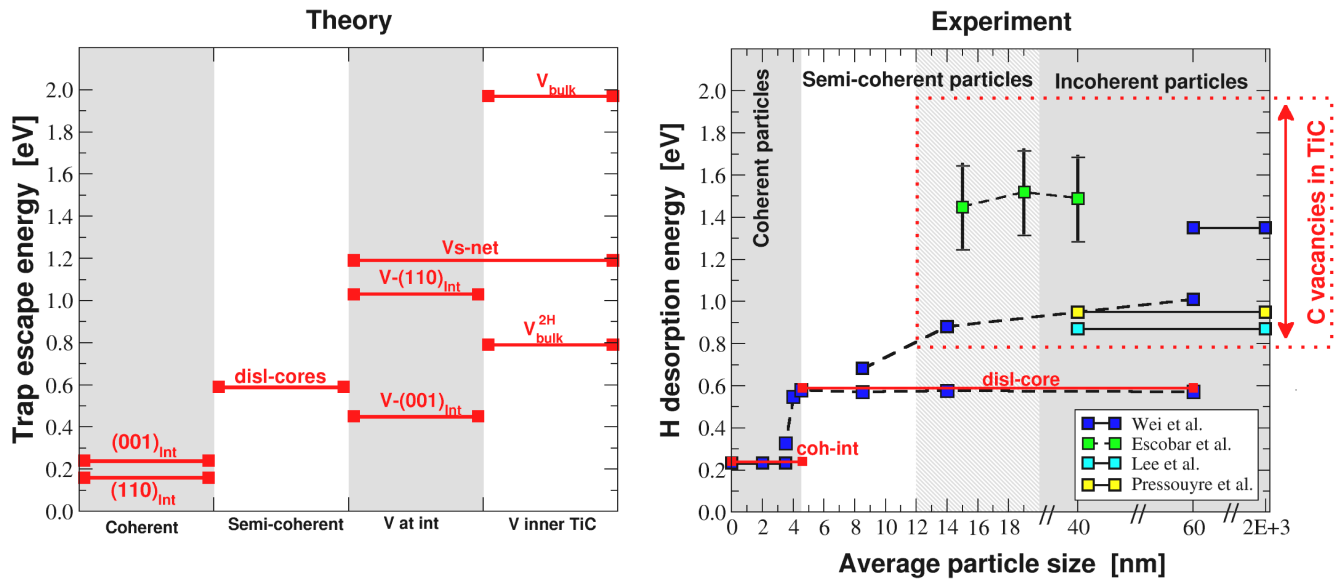
FIGURE 4.12: Left panel: trap escape energies (calculated according to Eqs. 4.3 and 4.4) as function of the source of traps (coherent interface, semi-coherent interface, C vacancies at the interface, and C vacancies inside the TiC precipitate). The labels refer to those in Table. 4.7. In addition the escape energy from a per-coleting network of C vacancies is labeled as "Vs-net". Right panel: H desorption energies from various experimental studies (see the text) as function of the average size of the particles. The left grey region of the plot indicates the size range of coherent TiC particles, the white region indicates the size range of semi-coherent TiC paticles, and most right grey region indicates the size range of incoherent particles. The division between semi-coherent and incoherent particles is not sharp and this is highlited by the grey striped region. Note that since Pressouyre and Bernstein did not perform TDS but they used a permeation technique, the reported energy value is not properly a desorption energy. For comparison the most relevant trap escape energies are marked in red.

The value are obtained by studies of Wei and Tsuzaki [36, 178, 179], Escobar et al. [180], Lee and Lee [202], and Pressouyre and Bernstein [184]. In the studies [36, 178–180] steel samples were lab processed in order to investigate samples with distinguishably different microstructures. In this way, it was possible to link H desorption energies to specific TiC precipitate sizes. In contrast, Lee and Lee [202], and Pressouyre and Bernstein [184], investigated samples containing precipitates with relative large size ranges. This is indicated in Fig. 4.12(b) by the solid horizontal lines spanning the results of this studies.

Comparing Fig. 4.12(a) and 4.12(b), one notices immediately an apparently rather good agreement between some trap escape energies calculated in this work and those reported in the considered experimental investigations. A more detailed comparison reveals a constant desorption energy for very small particles, as Wei

and Tsuzaki report, which can be identified with that from perfectly coherent interfaces, as marked in Fig. 4.12(b) with the full red line labeled coh-Int.

For precipitates larger than about 4 nm, deeper traps are reported which can be naturally associated with the misfit dislocation cores at the semi-coherent interface. Even in this case, despite of the approximation used in the calculations, we get a very good agreement between the experimental and theoretical values (marked in Fig. 4.12(b)).

When the particle size exceeds about 10-14 nm, deeper traps arise and, up to the order of the micrometers, the desorption energies vary in a range from 0.9 to 1.8 eV. In the studies of Wei et al. [36, 178] and Escobar et al. [180], detailed analyses of these traps revealed that it is not possible to charge them with H by cathodic charging at room temperature. It was concluded that H atoms can be absorbed in steel only at high temperature during heat treatment. Furthermore, Wei and Tsuzaki [178] correlated the amount of H segregated in these traps with the volume of the precipitates but not with their surface area. Based on these findings, it is plausible to associate the largest desorption energies in Fig 4.12b with trapping of H atoms in C vacancies inside the precipitate. Neither the reported experimental observations nor our theoretical results allow to identify the precise nature of the trapping mechanism involved. From our results, we can exclude only the role of isolated vacancies in the interior of the carbides, since the trap escape energy seems to be too high. Since the experimental results are rather scattered it is possible that the deep trapping is associated with a collective effect of different traps. In fact, as mentioned in the introduction of this chapter, the reported experimental data are indirect measurements which need interpretations. Such interpretations can be done in different ways and involve several approximations as described in Refs. [182, 183, 185]. The main approximation is that once H is released from its trap, it diffuses out of the material without encountering any further barriers [178–180, 183]. This can be a good approximation for the traps at the interface (the migration energy barrier in bulk Fe is very low, see Sec 2.5.2), but it is more critical for the traps inside the carbides where H atoms have to penetrate through the TiC particle in order to diffuse out of the material.

Note that the work of Pressouyre and Bernstein is the only one (to our knowledge) that reports deep traps (about 0.9 eV) that could become populated at room temperature. They attributed these traps to the TiC/Fe interfaces, but they did not provide any further evidence supporting this hypothesis. According to our results, the only possible trap with such a characteristics is provided by C vacancies at the

$(110)_{Fe}/(001)_{TiC}$ interface.

Like for the results obtained for H interaction with grain boundaries (see Chap. 3) we believe that the results obtained in this chapter are qualitatively valid for other types of carbide precipitate, provided that they have the same rock-salt structure.

4.5.3 Influence of precipitates on the distribution of H

We calculated the segregation energy for various types of traps associated with TiC precipitates in Fe. In this section we want to estimate how these traps influence the H distribution and whether they effectively reduce the amount of H that can be accumulated at relevant trap sites, for instance, at dislocation cores in the Fe matrix. To try a quantitative estimate for this issue is rather difficult, and it is out of the scope of this section which aims to a qualitative estimate only. Itakura et al. [203] investigated the segregation of H at screw dislocations in bcc Fe. They reported a maximum segregation energy of about 0.25 eV. Similar results have been reported by Kimizuka et al. [204]. Based on their results and on the obtained segregation energies at TiC precipitates, it is possible to estimate how the carbides influence the H population at cores of screw dislocations in Fe. We consider three different concentrations, $\rho_1 = 8 \cdot 10^{-6}$ nm^{-3} , $\rho_2 = 10^{-6}$ nm^{-3}, and $\rho_3 = 3 \cdot 10^{-7}$ nm^{-3}) for disk-shaped semicoherent precipitates with a diameter of 15 nm. These values have been inferred from the experimental investigations of Wei and Tsuzaki [178] and Takahashi et al. [37]. Further, we assume that the precipitates are atomically thin, and that the only possible trap sites are provided by the coherent interface regions and by the misfit dislocations cores. By means of the Langmuir-McLean model (Eq 3.9) the occupancy of the traps at the semicoherent interface, the change of H concentration in the bulk Fe due to the carbide, and the resulting change of the H concentration at the cores of Fe screw dislocations can be calculated. Fig. 4.13 shows the ratio of the H occupancy at dislocation cores for systems with and without precipitates as function of the total H bulk concentration.

The results indicate that the effectiveness of the considered traps to reduce the amount of H which can be trapped at dislocation cores is strongly dependent on the precipitate density. For instance, at a reasonable bulk H concentration of 50 atomic ppm, for the precipitate density ρ_1 the dislocation cores are essentially
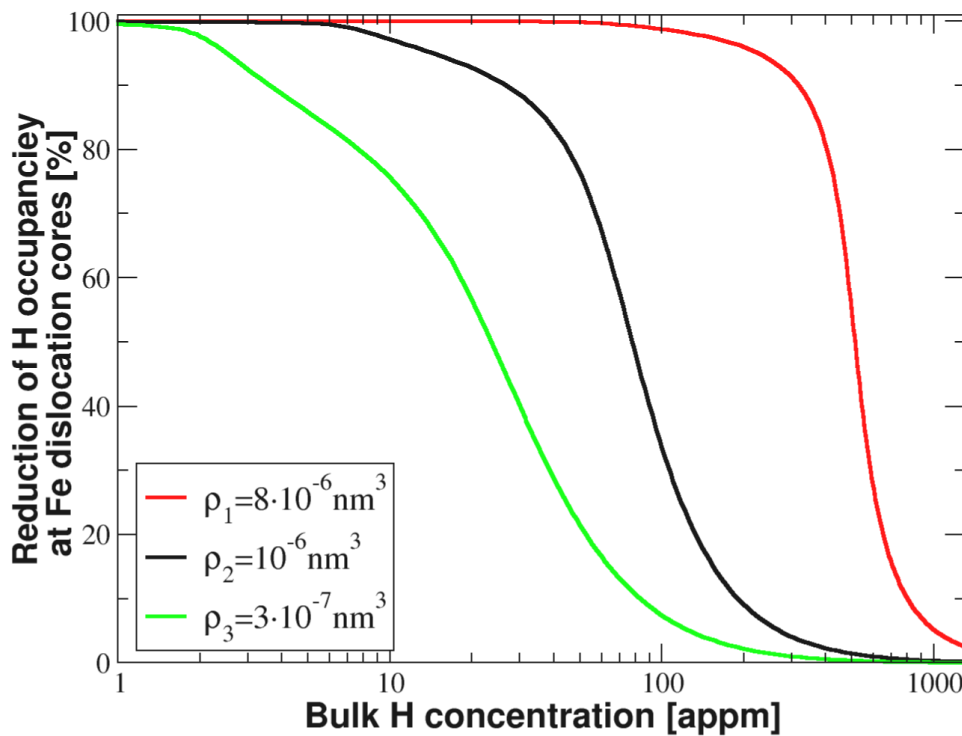
FIGURE 4.13: Reduction of the H occupancy at Fe screw dislocation cores due the presence of different concentrations of semi-coherent carbide precipitates at T=300 K.

unoccupied, while for the density ρ_3 the occupation is reduced by only 20%.

It is important to bear in mind that the presented results have to be considered as rough estimates since effects due to dislocation strain fields and to the presence of other extended traps, such as grain boundaries and other types of dislocations, have not been taken into account. However it has been shown that rather shallow traps can reduce significantly the amount of H at critical sites, provided that the trap density is large enough. Therefore is may not necessary to have very deep traps which immobilize permanently the diffusible H atoms as often assumed in the literature [176, 182, 183].

4.6   Conclusions

In this chapter, the interaction between interstitial H and TiC precipitate in Fe has been investigated in detail. Several types of Fe/TiC interfaces and the interior of the carbide were considered as possible sources of traps for H atoms.

In particular, we have acquired the energetics associated with H trapping for $(001)_{Fe}/(001)_{TiC}$ semicoherent interfaces, $(110)_{Fe}/(001)_{TiC}$ interfaces, C vacancies at these interfaces, and various C vacancy complexes in the interior of the carbides. The key findings can be summarized as:

1. There is no single trapping energy associated with TiC particles but the trapping energies depend sensitively on the trapping site and type of a trap.

2. H trapping at the semicoherent interfaces between TiC particles and Fe matrix is moderate, the trap energy ranges between 0.32 eV for coherent interface segments, and 0.50 eV, for misfit dislocation cores.

3. C vacancies in the interior of TiC are the strongest traps, but their population happens only at very high temperatures.

4. The energy barrier to overcomefor populating C vacancies is reduced in case of carbides with percolating networks of C vacancies, but this requires highly non-stoichiometric carbides.

5. In the case of coherent and semicoherent interfaces, the comparison with available experimental results reveals a very good agreement and contributes to clarify the nature of the experimentally observed trapping behavior.

6. In the case of C vacancies, the spread of trapping energies is in the range of experimental results for the deepest traps, but in this case a quantitative comparison is too difficult.

7. Furthermore, we estimated the reduction of the H population of cores of screw dislocations in Fe due to the presence of semicoherent precipitates. We found that the H content at dislocation cores is significantly reduced only for high concentrations of carbide precipitates.

Chapter 5

Summary and outlook

5.1   Summary

In this thesis several aspects of the interaction of H with atomic and extended extended defects in the microstructure of iron and nickel have been investigated using first-principles approaches.

In Chapter 2, the diffusion coefficients for the migration of H in bcc Fe and fcc Ni were calculated over a wide range of temperatures. By including quantum-mechanical effects, we were able to achieve a high theoretical quality and a very good agreement with experimental studies. To this end we employed and discussed in detail the semi-classical transition state theory and the small-polaron model of Flynn and Stoneham. The main advantages of these two approaches are their computational simplicity and the small number of theoretical input data needed to parametrize them. We found that the inclusion of quantum-mechanical effects is very important for an accurate description of the migration of H in bcc Fe but it is less crucial for fcc Ni. Furthermore our study provides some criteria to predict the influence of quantum-mechanical effects in a given system.

In Chapter 3 we investigated the interaction between H interstitial and grain boundaries in polycrystalline Ni. First we considered the trapping and migration of H at GBs. Our results show a strong dependency on the GB character. GBs with close-packed interface structure, like the investigated $\Sigma 3(111)[\bar{1}10]$, do not trap H and can acts as two-dimensional obstacles for H diffusion. On the other

hand GBs with more open-interface structure, like the Σ5(210)[001], can act as effective two-dimensional sinks for H atoms and provide fast migration channels along the GB plane. In the simulated specific case the diffusivity was enhanced by about two orders of magnitude with respect to the single crystal.

In the following of the chapter we focused on the Σ5 STGB since it has the most interesting characteristics. We estimated how much H can accumulate at this GBs for realistic bulk concentrations of H at finite temperature. This has been done linking DFT results with the Langmuir-McLean model. It was found that in extreme experimental conditions a large amount of H can actually segregate at GBs, while in more realistic conditions the mean GB concentration of H is noticeably lower. For reasonable H concentrations, we investigated the effects of H on the GBs cohesion by calculating the ideal work of separation and performing computational tensile tests. The calculation of the work of separation reveals that a strong reduction of the GBs cohesion is possible (up to about 50 %) in extreme experimental conditions. However, since the cohesion reduction depends strongly on the H concentration at the boundary, it does not seem to be sufficient for pure brittle fracture in realistic conditions. To obtain the work of separation is rather simple, but this quantity is not enough to describe all the aspects of fracture. Computational tensile tests, instead, give more information on the mechanisms of fracture, but they are computationally rather expensive. For this reason, in this thesis we have applied this method to few cases only. The results indicate that there is a strong reduction of the ideal toughness of the Σ5 GB, by about 33% for relatively low H concentration. On the contrary to the work of separation, the reduction of toughness seems to decrease when more H is segregated at the GB. An explanation for this counter-intuitive behavior is given in terms of two concurrent effects of the H atoms in Ni. H reduces the strength of neighboring Ni-Ni bonds by acting as an electron acceptor. But at the same time H creates relatively strong bonds with the neighboring Ni atoms which thus tend to hold together the two grains.

In Chapter 4, the H trapping properties of a TiC precipitate in an Fe metal matrix was investigated. Several types of Fe/TiC heterophase interfaces and the interior of the carbide have been considered as possible locations of traps for H atoms. In particular we acquired the energetics of H trapping for the $(001)_{Fe}/(001)_{TiC}$ semi-coherent interface, the $(110)_{Fe}/(001)_{TiC}$ interface, C vacancies at these interfaces, and C vacancies in the interior of the carbide. Our results show that there is a

broad spectrum of possible traps with various characteristic traps energies. Traps at interfaces are not very strong: the segregation energy ranges from 0.32 eV for coherent interfaces to 0.50 eV for misfit dislocation cores at semicoherent interfaces. C vacancies in the interior of the carbide are rather strong traps, but, since there is a high energy barrier to overcome, their population becomes possible only at very high temperature. This barrier is strongly reduced in case of a percolating network of C vacancies from the interface to the interior of the precipitate, but this requires a highly non-stoichiometric carbide. The feasibility of that calls for an additional investigation. A part from that, we showed also that if the density of traps is high enough, it is not necessary for them to be very deep to have a significant effect.

For all investigated systems, a thorough comparison with experimental and other theoretical studies has been performed. This analysis reveals an overall good agreement and sheds light on various inconsistencies in literature data. In case of H diffusion in Fe we showed that the large scatter in the reported experimental data is related to the Arrhenius-type analysis which is commonly applied for the interpretation of the measured diffusion data, and that their agreement with some theoretical studies, based on a classical description of H diffusion, is most likely fortuitous. Regarding H diffusion at GB, experiments report a similar enhancement of the diffusivity to those that we have found. Furthermore, the comparison with available literature data suggests that the chosen GBs can be considered as characteristic representatives for a larger variety of GBs. Therefore, the markedly different behaviors of the $\Sigma 3$ and $\Sigma 5$ can explain the different fracture modes of a sample containing a high concentration of special GBs and samples with a high concentration of general GBs. In case of Fe/TiC we obtained a good consistency of our theoretical results with the many available experimental data, and our results offer a clear scenario of the atomic trap mechanisms. In this case there are essentially no theoretical data of H segregation at precipitates for comparison. To our knowledge, ours is the first theoretical study which attempts to consider a whole variety of interactions between H and a carbide precipitate in Fe. We hope that this will stimulate further theoretical and experimental efforts do design and develop high-strength steels which are less sensitive to HE by efficiently trapping H in the microstructure.

5.2   Outlook

The work presented in this thesis contributes to a better understanding of the interaction of hydrogen with the microstructure of metals, in particular for what concerns H transport. This field of study is a rather broad one and therefore several extensions, improvements, and generalizations of our results are not only possible but also necessary.

A definitely important generalization of our work will be to consider other metallic systems. The two presented approaches to include quantum-mechanical effects in the description of H diffusion are potentially transferable from the two considered elemental metals to other metals and to more complex microstructural features, for instance studies of H diffusion and trapping at extended defects, such as grain boundaries and dislocation cores. In chapter 3, we proposed that the results obtained for GBs in Ni are qualitatively valid also for GBs in other metals. We supposed that the H diffusion along open-structure GBs is similar for all metals and that the controversies in the literature about the effect of GBs on diffusion of H are more due to the bulk diffusion. If the bulk diffusion is sufficiently fast, the effect of enhanced diffusion along GBs can be neglected, or the trapping may even prevail. Even if the analyzed results from literature seem to confirm this hypothesis, a definite answer to this issue requires further studies. In a similar way, the approach presented in chapter 4 to investigate the H trapping properties of the Fe/TiC system can be transferred easily to other intermetallic alloys and compounds containing carbide or nitride precipitates.

Other potential extensions to this work are more specific to the investigated cases of Fe-H and Ni-H. In chapter 3 a multiscale model for a quantitative description of H diffusion in a polycrystalline material was only proposed. But applications were not yet provided. Nevertheless we believe that this may become one of the most promising approaches to the problem and we hope that the effectiveness of this model will be demonstrated in a future work. In the same chapter we reported our observation of two antithetical effects of atomic H on the cohesion of GBs in Ni. A conclusive confirmation needs definitely an additional effort. Both for the Ni GBs and for the Fe/TiC cases, we showed how atomistic results can be extended to the macroscopic scale by means of thermodynamical models. However in both cases we provided only simplified approaches which need to be extended and refined for a thorough understanding of the investigated problematic issues.

To conclude we want to recall that the interaction of hydrogen with metals is a long standing scientific and technological challenge with still many unsolved problems. We believe that this thesis contributes to answer some of the open questions and we hope that some paths to address other open question have been outlined.

Bibliography

[1] Ogden, J. M. Hydrogen - the fuel of the future? *J. Electrical Electron. Eng. Res.* **1**, 51 (2002).

[2] Mueller-Langer, F., Tzimas, E., Kaltschmitt, M. & Peteves, S. Techno-economic assessment of hydrogen production processes for the hydrogen economy for the short and medium term. *Int. J. Hydrogen Energy* **32**, 3797 (2007).

[3] Marbán, G. & Valdés-Solís, T. Towards the hydrogen economy? *Int. J. Hydrogen Energy* **32**, 1625 (2007).

[4] Ball, M., Wietschel, M. & Rentz, O. Integration of a hydrogen economy into the German energy system: an optimising modelling approach. *Int. J. Hydrogen Energy* **32**, 1355 (2007).

[5] Lauermann, G., Häussinger, P., Lohmüller, R. & Watson, A. M. Hydrogen, 1. Properties and Occurrence. *Ullmann's Encyclopedia of Industrial Chemistry* (2000).

[6] Yang, Z. G., Weil, K. S. & Brady, M. P. Materials in Clean Power Systems: Applications, Status and Challenges. *Int. J. Hydrogen Energy* **32**, 3609 (2007).

[7] Jena, P. Materials for hydrogen storage: Past, present, and future. *J. Phys. Chem. Lett.* **2**, 206 (2011).

[8] Sherif, S. A., Barbir, F. & Veziroglu, T. N. Wind energy and the hydrogen economy—review of the technology. *Sol. Energy* **78**, 647 (2005).

[9] Nanninga, N., Slifka, A., Levy, Y. & White, C. A review of fatigue crack growth for pipeline steels exposed to hydrogen. *J. Res. Nat. Inst. Stand. Technol.* **115**, 437 (2010).

[10] Lynch, S. Failures of Engineering Components Due to Environmentally Assisted Cracking. *J. Fail. Anal. Prev.* **3**, 33 (2003).

[11] Lovicu, G. *et al.* Hydrogen embrittlement of automotive advanced high-strength steels. *Metall. Mater. Trans. A* **43**, 4075 (2012).

[12] CO_2–Bilanz Stahl. Tech. Rep., The Boston Consulting Group, Düsseldorf (2010).

[13] Loidl, M. & Kolk, O. Hydrogen embrittlement in HSSs limits use in lightweight body in white design. *Adv. Mater. Processes* **169**, 22 (2011).

[14] Deville, S. C. Osservazioni sulla permeabilità del platino e del ferro e di altre sostanze ai gas ad alta temperatura. *Il Nuovo Cimento* **18**, 403 (1863).

[15] Graham, T. On the absorption and dialytic separation of gases by colloid septa. *Phil. Trans. R. Soc. Lond.* **156**, 399 (1866).

[16] Johnson, W. H. On some remarkable changes produced in iron and steel by the action of hydrogen and acids. *Nature* **11**, 393 (1875).

[17] Alefeld, G. & Völkl, J. (eds.) *Hydrogen in metals I-Basic properties*, vol. 28 of *Topics in Applied Physics* (Springer-Verlag, 1978).

[18] Alefeld, G. & Völkl, J. (eds.) *Hydrogen in metals II-Application-oriented properties*, vol. 29 of *Topics in Applied Physics* (Springer-Verlag, 1978).

[19] Schlapbach, L. (ed.) *Hydrogen in intermetallic compounds I*, vol. 63 of *Topics in Applied Physics* (Springer-Verlag, 1988).

[20] Schlapbach, L. (ed.) *Hydrogen in intermetallic compounds II*, vol. 64 of *Topics in Applied Physics* (Springer Verlag, 1988).

[21] Wipf, H. (ed.) *Hydrogen in metals III: properties and applications*, vol. 73 of *Topics in Applied Physics* (Springer Verlag, 1997).

[22] Fukai, Y. *The metal-hydrogen system: basic bulk properties* (Springer, 2004).

[23] Robertson, I. M., Birnbaum, H. K. & Sofronis, P. Hydrogen effects on plasticity. In Hirth, J. & Kubin, L. (eds.) *Dislocations in Solids*, vol. 15, chap. 91, 249 (Elsevier, 2009).

[24] Gangloff, R. P. & Somerday, B. P. *Gaseous Hydrogen Embrittlement of Materials in Energy Technologies: Mechanisms, modelling and future developments*, vol. 2 (Elsevier, 2012).

[25] Hoagland, R. G. & Heinisch, H. L. An atomic simulation of the influence of hydrogen on the fracture behavior of nickel. *J. Mater. Res.* **7**, 2080 (1992).

[26] Geng, W., Freeman, A., Wu, R., Geller, C. & Raynolds, J. Embrittling and strengthening effects of hydrogen, boron, and phosphorus on a $\Sigma 5$ nickel grain boundary. *Phys. Rev. B* **60**, 7149 (1999).

[27] Van der Ven, A. & Ceder, G. The thermodynamics of decohesion. *Acta Mater.* **52**, 1223 (2004).

[28] Nagumo, M. Function of hydrogen in embrittlement of high-strength steels. *ISIJ International* **41**, 590 (2001).

[29] Birnbaum, H. K. Mechanical properties of metal hydrides. *J. Less Common Met.* **104**, 31 (1984).

[30] Lynch, S. Hydrogen embrittlement phenomena and mechanisms. *Corros. Rev.* **30**, 105 (2012).

[31] Myers, S. M. *et al.* Hydrogen interactions with defects in crystalline solids. *Rev. Mod. Phys.* **64**, 559 (1992).

[32] Pundt, A. & Kirchheim, R. Hydrogen in Metals: Microstructural Aspects. *Annu. Rev. Mater. Sci.* **36**, 555 (2006).

[33] Robertson, I. M. *et al.* Hydrogen Embrittlement Understood. *Metall. Mater. Trans. A* **46**, 2323 (2015).

[34] Volkl, J. & Alefeld, G. Hydrogen diffusion in metals. In Nowick, A. S. & Burton, J. J. (eds.) *Diffusion in solids: recent developments*, chap. 5, 231 (Academic Press New York, 1975).

[35] Dadfarnia, M. *et al.* Recent advances in the study of structural materials compatibility with hydrogen. *Adv. Mater.* **22**, 1128 (2010).

[36] Wei, F. G. & Tsuzaki, K. Hydrogen absorption of incoherent TiC particles in iron from environment at high temperatures. *Metall. Mater. Trans. A* **35**, 3155 (2004).

[37] Takahashi, J., Kawakami, K., Kobayashi, Y. & Tarui, T. The first direct observation of hydrogen trapping sites in TiC precipitation-hardening steel through atom probe tomography. *Scr. Mater.* **63**, 261 (2010).

[38] Young, G. A. & Scully, J. R. The diffusion and trapping of hydrogen in high purity aluminum. *Acta Mater.* **46**, 6337 (1998).

[39] Oudriss, A. *et al.* Grain size and grain-boundary effects on diffusion and trapping of hydrogen in pure nickel. *Acta Mater.* **60**, 6814 (2012).

[40] Sørensen, M. R., Mishin, Y. & Voter, A. F. Diffusion mechanisms in Cu grain boundaries. *Phys. Rev. B* **62**, 3658 (2000).

[41] Pressouyre, G. M. Trap theory of hydrogen embrittlement. *Acta Metall.* **28**, 895 (1980).

[42] Schaumann, G., Völkl, J. & Alefeld, G. The diffusion coefficients of hydrogen and deuterium in vanadium, niobium, and tantalum by Gorsky effect measurements. *Phys. Stat. Sol.* **42**, 401 (1970).

[43] Hanada, R. On the mobility of hydrogen and deuterium in tantalum between 4.2 and 60 K. *Scr. Metall.* **7**, 681 (1973).

[44] Fritz, J. J., Maria, H. J. & Aston, J. G. Concerning the Feasibility of Nuclear Cooling with Palladium Hydride. *J. Chem. Phys.* **34**, 2185 (1961).

[45] Katzarov, I. H., Pashov, D. L. & Paxton, A. T. Fully quantum mechanical calculation of the diffusivity of hydrogen in iron using the tight-binding approximation and path integral theory. *Phys. Rev. B* **88**, 054107 (2013).

[46] Elsässer, C., Krimmel, H., Fähnle, M., Louie, S. G. & Chan, C. T. Ab initio study of iron and iron hydride: III. Vibrational states of H isotopes in Fe, Cr and Ni. *J. Phys.: Condens. Matter* **10**, 5131 (1998).

[47] Kiuchi, K. & McLellan, R. B. The solubility and diffusivity of hydrogen in well-annealed and deformed iron. *Acta Metall.* **31**, 961 (1983).

[48] Kimizuka, H., Mori, H. & Ogata, S. Effect of temperature on fast hydrogen diffusion in iron: A path-integral quantum dynamics approach. *Phys. Rev. B* **83**, 094110 (2011).

[49] Winzer, N. & Mrovec, M. Multiscale Approaches to Hydrogen-Assisted Degradation of Metals. *JOM* **66**, 1366 (2014).

[50] Winzer, N., Di Stefano, D., Mrovec, M., Katzarov, I. & Paxton, A. Industrially-Relevant Multiscale Modeling of Hydrogen Assisted Degradation. In *International Hydrogen Conference (IHC 2012)* (ASME Press, 2014).

[51] Jothi, S., Croft, T. N. & Brown, S. G. R. , Multiscale multiphysics model for hydrogen embrittlement in polycrystalline nickel. *J. Alloys Compd.* S500 (2014).

[52] Jothi, S., Winzer, N., Croft, T. N. & Brown, S. G. R. Meso-microstructural computational simulation of the hydrogen permeation test to calculate intergranular, grain boundary and effective diffusivities. *J. Alloys Compd.* **645**, S247 (2015).

[53] Pollock, T. M. & Tin, S. Nickel-based superalloys for advanced turbine engines: chemistry, microstructure and properties. *J. Propul. Power* **22**, 361 (2006).

[54] Reese, E. D. *et al.* Hydrogen Embrittlement of Pulse-Plated Nickel. *JOM* **66**, 1368 (2014).

[55] Hirth, J. P. Effects of hydrogen on the properties of iron and steel. *Metall. Trans. A* **11**, 861 (1980).

[56] Martin, R. M. *Electronic structure: basic theory and practical methods* (Cambridge University Press, 2004).

[57] Payne, M. C., Teter, M. P., Allan, D. C., Arias, T. A. & Joannopoulos, J. D. Iterative minimization techniques for ab initio total-energy calculations: molecular dynamics and conjugate gradients. *Rev. Modern Phys.* **64**, 1045 (1992).

[58] Hohenberg, P. & Kohn, W. Inhomogeneous electron gas. *Phys. Rev.* **136**, B864 (1964).

[59] Born, M. & Oppenheimer, R. Zur Quantentheorie der Molekeln. *Ann. Phys.* **389**, 457 (1927).

[60] Foulkes, W. M. C., Mitas, L., Needs, R. J. & Rajagopal, G. Quantum Monte Carlo simulations of solids. *Rev. Mod. Phys.* **73**, 33 (2001).

[61] Slater, J. C. A Simplification of the Hartree-Fock-Method. *Phys. Rev.* **3**, 385 (1951).

[62] Cramer, C. J. *Essentials of Computational Chemistry: Theories and Models*, vol. 108 (John Wiley & Sons, 2002).

[63] W. Kohn, L. J. S. Self-consistent equations including exchange and correlation effects. *Phys. Rev.* **140**, 1133 (1965).

[64] Perdew, J. P., Burke, K. & Ernzerhof, M. Generalized gradient approximation made simple. *Phys. Rev. Lett.* **77**, 3865 (1996).

[65] Becke, A. D. Density-functional thermochemistry. III. The role of exact exchange. *J. Chem. Phys.* **98**, 5648 (1993).

[66] Di Stefano, D., Mrovec, M. & Elsässer, C. First-principles investigation of quantum mechanical effects on the diffusion of hydrogen in iron and nickel. *Phys. Rev. B* **92**, 224301 (2015).

[67] Mehrer, H. *Diffusion in solids: fundamentals, methods, materials, diffusion-controlled processes*, vol. 155 (Springer Science, 2007).

[68] Shaw, D. *Atomic diffusion in semiconductors* (Springer, 2012).

[69] Reed-Hill, R. E. & Abbaschian, R. *Physical metallurgy principles*, chap. 12-15 (Van Nostrand, 1973).

[70] O'Hayre, R. P., Cha, S.-W., Colella, W. & Prinz, F. B. *Fuel cell fundamentals*, chap. 4-5 (John Wiley & Sons, 2006).

[71] Fermann, J. T. & Auerbach, S. Modeling proton mobility in acidic zeolite clusters: II. Room temperature tunneling effects from semiclassical rate theory. *J. Chem. Phys.* **112**, 6787 (2000).

[72] Sholl, D. S. Using density functional theory to study hydrogen diffusion in metals: A brief overview. *J. Alloys Compd.* **446**, 462 (2007).

[73] Emin, D., Baskes, M. I. & Wilson, W. D. Small-polaronic diffusion of light interstitials in bcc metals. *Phys. Rev. Lett.* **42**, 791 (1979).

[74] Flynn, C. & Stoneham, A. Quantum theory of diffusion with application to light interstitials in metals. *Phys. Rev. B* **1**, 3966 (1970).

[75] Fick, A. Über Diffusion. *Ann. Phys.* **94**, 59 (1855).

[76] Crank, J. *The mathematics of diffusion* (Oxford University Press, 1979).

[77] Glicksman, M. E. *Diffusion in solids* (Wiley, 2000).

[78] Messer, R. *et al.* Nuclear Magnetic Resonance Studies of Hydrogen Diffusion, Trapping, and Site Occupation in Metals. *Z. Phys. Chem.* 61 (1986).

[79] Einstein, A. Über die von der molekularkinetischen Theorie der Wärme geforderte Bewegung von in ruhenden Flüssigkeiten suspendierten Teilchen. *Ann. Phys.* **4** (1905).

[80] Von Smoluchowski, M. Zur kinetischen Theorie der Brownschen Molekularbewegung und der Suspensionen. *Ann. Phys.* **326**, 756 (1906).

[81] Eyring, H. The activated complex in chemical reactions. *J. Chem. Phys.* **3**, 107 (1935).

[82] Evans, M. G. & Polanyi, M. Further considerations on the thermodynamics of chemical equilibria and reaction rates. *Trans. Faraday Soc.* **32**, 1333 (1936).

[83] Born, M. & Huang, K. *Dynamical Theory of Crystal Lattices*. International series of monographs on physics (Clarendon Press, 1998).

[84] Henkelman, G., Jóhannesson, G. & Jónsson, H. Methods for finding saddle points and minimum energy paths. In Schwartz, S. D. (ed.) *Theoretical Methods in Condensed Phase Chemistry*, 269 (Springer, 2002).

[85] Henkelman, G., Uberuaga, B. P. & Jónsson, H. Climbing image nudged elastic band method for finding saddle points and minimum energy paths. *J. Chem. Phys.* **113**, 9901 (2000).

[86] Sholl, D. & Steckel, J. A. *Density functional theory: a practical introduction* (John Wiley & Sons, 2011).

[87] Baroni, S., De Gironcoli, S., Dal Corso, A. & Giannozzi, P. Phonons and related crystal properties from density-functional perturbation theory. *Rev. Mod. Phys.* **73**, 515 (2001).

[88] Baird, J. K. & Schwartz, E. M. Isotope effect in hydrogen diffusion in metals. *Z. Phys. Chem.* **211**, 47 (1999).

[89] Sundell, P. G. & Wahnström, G. Self-trapping and diffusion of hydrogen in Nb and Ta from first principles. *Phys. Rev. B* **70**, 224301 (2004).

[90] Sundell, P. G. & Wahnström, G. Activation energies for quantum diffusion of hydrogen in metals and on metal surfaces using delocalized nuclei within the density-functional theory. *Phys. Rev. Lett.* **92**, 155901 (2004).

[91] Hulett, J. R. Deviations from the Arrhenius equation. *Q. Rev. Chem. Soc.* **18**, 227 (1964).

[92] Grabert, H. & Schober, H. R. Theory of tunneling and diffusion of light interstitials in metals. In Wipf, H. (ed.) *Hydrogen in Metals III*, chap. 2, 5 (Springer, 1997).

[93] Seeger, A. Positive muons as light isotopes of hydrogen. In Alefeld, G. & Völkl, J. (eds.) *Hydrogen in Metals I*, chap. 13, 349 (Springer, 1978).

[94] Elsässer, C., Ho, K. M., Chan, C. T. & Fahnle, M. First-principles pseudopotential calculations for hydrogen in 4d transition metals. II. Vibrational states for interstitial hydrogen isotopes. *J. Phys.: Condens. Matter* **4**, 5207 (1992).

[95] Krimmel, H., Schimmele, L., Elsässer, C. & Fähnle, M. Self-trapped hydrogen states in metals determined from quantum mechanical calculations using potentials based on ab initio data: I. Hydrogen isotopes in Pd. *J. Phys.: Condens. Matter* **6**, 7679 (1994).

[96] Jiang, D. E. & Carter, E. A. Diffusion of interstitial hydrogen into and through bcc Fe from first principles. *Phys. Rev. B* **70**, 064102 (2004).

[97] Ramasubramaniam, A., Itakura, M., Ortiz, M. & Carter, E. A. Effect of atomic scale plasticity on hydrogen diffusion in iron: Quantum mechanically informed and on-the-fly kinetic Monte Carlo simulations. *J. Mater. Res.* **23**, 2757 (2008).

[98] Wolverton, C. E., Ozoliņš, V. & Asta, M. Hydrogen in aluminum: First-principles calculations of structure and thermodynamics. *Phys. Rev. B* **69**, 144109 (2004).

[99] Wardle, M. G., Goss, J. P. & Briddon, P. R. First-principles study of the diffusion of hydrogen in ZnO. *Phys. Rev. Lett.* **96**, 205504 (2006).

[100] Kamakoti, P. & Sholl, D. S. A comparison of hydrogen diffusivities in Pd and CuPd alloys using density functional theory. *J. Membr. Sci.* 145 (2003).

[101] Gillan, M. J. The quantum simulation of hydrogen in metals. *Philos. Mag. A* **58**, 257 (1988).

[102] Voth, G. A. Feynman path integral formulation of quantum mechanical transition-state theory. *J. Phys. Chem.* **97**, 8365 (1993).

[103] Yoshikawa, T., Takayanagi, T., Kimizuka, H. & Shiga, M. Quantum–Thermal Crossover of Hydrogen and Tritium Diffusion in α-Iron. *J. Phys. Chem. C* **116**, 23113 (2012).

[104] Ebisuzaki, Y., Kass, W. J. & O'keeffe, M. Isotope effects in the diffusion and solubility of hydrogen in nickel. *J. Chem. Phys.* **46**, 1373 (1967).

[105] Bhatia, B. & Sholl, D. S. Chemisorption and diffusion of hydrogen on surface and subsurface sites of flat and stepped nickel surfaces. *J. Chem. Phys.* **122**, 204707 (2005).

[106] Wimmer, E. *et al.* Temperature-dependent diffusion coefficients from ab initio computations: hydrogen, deuterium, and tritium in nickel. *Phys. Rev. B* **77**, 134305 (2008).

[107] Hayashi, Y., Hagi, H. & Tahara, A. Diffusion Coefficients of Hydrogen and Deuterium in Iron Determined by Permeation with Gas, Ion and Electrochemical Charging. *Z. Phys. Chem.* **164**, 815 (1989).

[108] Beck, W., Bockris, J. O. M., McBreen, J. & Nanis, L. Hydrogen permeation in metals as a function of stress, temperature and dissolved hydrogen concentration. In *Proc. R. Soc. A*, vol. 290, 220 (1966).

[109] Nagano, M., Hayashi, Y., Ohtani, N., Isshiki, M. & Igaki, K. Diffusion of Hydrogen and Deuterium in High Purity Iron between 222 and 322 K. *J. Jpn. Inst. Met.* **22**, 423 (1981).

[110] Oriani, R. A. The diffusion and trapping of hydrogen in steel. *Acta Metall.* **18**, 147 (1970).

[111] Heumann, T. H. & Domke, E. Hydrogen diffusion in zone melted α-iron. *Ber. Bunsen Ges. Phys. Chem.* **76**, 825 (1972).

[112] Elsässer *et al.* Relativistic effects on ground state properties of 4d and 5d transition metals. *J. Phys.: Condens. Matter* **2**, 4371 (1990).

[113] Ho, K. M., Elsässer, C., Chan, C. T. & Fähnle, M. First-principles pseudopotential calculations for hydrogen in 4d transition metals. I. Mixed-basis method for total energies and forces. *J. Phys.: Condens. Matter* **4**, 5189 (1992).

[114] Meyer, B., Hummler, K., Elsässer, C. & Fähnle, M. Reconstruction of the true wavefunctions from the pseudowavefunctions in a crystal and calculation of electric field gradients. *J. Phys.: Condens. Matter* **7**, 9201 (1995).

[115] Lechermann, F., Fähnle, M., Meyer, B. & Elsässer, C. Electronic correlations, magnetism, and structure of Fe-Al subsystems: An LDA+U study. *Phys. Rev. B* **69**, 165116 (2004).

[116] Sánchez, J., Fullea, J., Andrade, C. & De Andres, P. L. Hydrogen in α-iron: Stress and diffusion. *Phys. Rev. B* **78**, 014113 (2008).

[117] Tao, H. J., Ho, K. M. & Zhu, X. Y. Investigation of the electronic structure and phonon anharmonicity in β-and γ-NbH. *Phys. Rev. B* **34**, 8394 (1986).

[118] Elsässer, C., Ho, K. M., Chan, C. T. & Fähnle, M. Vibrational states for hydrogen in palladium. *Phys. Rev. B* **44**, 10377 (1991).

[119] Völkl, J. & Alefeld, G. Diffusion of hydrogen in metals. In Völkl, J. & Alefeld, G. (eds.) *Hydrogen in metals I*, 321 (Springer, 1978).

[120] Katz, L., Guinan, M. & Borg, R. J. Diffusion of H_2, D_2, and T_2 in single-crystal Ni and Cu. *Phys. Rev. B* **4**, 330 (1971).

[121] Di Stefano, D., Mrovec, M. & Elsässer, C. First-principles investigation of hydrogen trapping and diffusion at grain boundaries in nickel. *Acta Mater.* **98**, 306 (2015).

[122] Gangloff, R. P. & Somerday, B. P. (eds.). *Gaseous Hydrogen Embrittlement of Materials in Energy Technologies: Mechanisms, modelling and future developments*, vol. 2, chap. 12 (Elsevier, 2012).

[123] Wang, S. *et al.* Hydrogen-induced intergranular failure of iron. *Acta Mater.* **69**, 275 (2014).

[124] Bechtle, S., Kumar, M., Somerday, B. P., Launey, M. E. & Ritchie, R. O. Grain-boundary engineering markedly reduces susceptibility to intergranular hydrogen embrittlement in metallic materials. *Acta Mater.* **57**, 4148 (2009).

[125] Seita, M., Hanson, J. P., Gradečak, S. & Demkowicz, M. J. The dual role of coherent twin boundaries in hydrogen embrittlement. *Nat. Commun.* **6** (2015).

[126] Martin, M. L., Somerday, B. P., Ritchie, R. O., Sofronis, P. & Robertson, I. M. Hydrogen-induced intergranular failure in nickel revisited. *Acta Mater.* **60**, 2739 (2012).

[127] Sutton, A. & Balluffi, R. *Interfaces in crystalline materials*. Monographs on the physics and chemistry of materials (Clarendon Press, 1995).

[128] Olmsted, D. L., Foiles, S. M. & Holm, E. A. Survey of computed grain boundary properties in face-centered cubic metals: I. Grain boundary energy. *Acta Mater.* **57**, 3694 (2009).

[129] Yamaguchi, M., Shiga, M. & Kaburaki, H. First-principles study on segregation energy and embrittling potency of hydrogen in NiΣ5(012) tilt grain boundary. *J. Phys. Soc. Jpn.* **73**, 441 (2004).

[130] Všianská, M. & Šob, M. The effect of segregated sp-impurities on grain-boundary and surface structure, magnetism and embrittlement in nickel. *Prog. Mater Sci.* **56**, 817 (2011).

[131] Du, Y. A. *et al.* First-principles study on the interaction of H interstitials with grain boundaries in α- and γ-Fe. *Phys. Rev. B* **84**, 144121 (2011).

[132] Pedersen, A. & Jónsson, H. Simulations of hydrogen diffusion at grain boundaries in aluminum. *Acta Mater.* **57**, 4036 (2009).

[133] Shen, X., Tanguy, D. & Connétable, D. Atomistic modelling of hydrogen segregation to the Σ9{2 2 1}[1 1 0] symmetric tilt grain boundary in Al. *Philos. Mag.* **94**, 2247 (2014).

[134] Du, Y. A., Rogal, J. & Drautz, R. Diffusion of hydrogen within idealized grains of bcc Fe: A kinetic Monte Carlo study. *Phys. Rev. B* **86**, 174110 (2012).

[135] Szpunar, B., Lewis, L. J., Swainson, I. & Erb, U. Thermal expansion and hydrogen diffusion in nanocrystalline nickel. *Phys. Rev. B* **60**, 10107 (1999).

[136] Ichitani, K. & Kanno, M. Visualization of hydrogen diffusion path by a high sensitivity hydrogen microprint technique. *Sci. Technol. Adv. Mater.* **4**, 545 (2003).

[137] Ladna, B. & Birnbaum, H. K. SIMS study of hydrogen at the surface and grain boundaries of nickel bicrystals. *Acta Metall.* **35**, 2537 (1987).

[138] Oudriss, A. *et al.* The diffusion and trapping of hydrogen along the grain boundaries in polycrystalline nickel. *Scr. Mater.* **66**, 37 (2012).

[139] von Pezold, J., Lymperakis, L. & Neugebeauer, J. Hydrogen-enhanced local plasticity at dilute bulk H concentrations: The role of H–H interactions and the formation of local hydrides. *Acta Mater.* **59**, 2969 (2011).

[140] Connétable, D., Wang, Y. & Tanguy, D. Segregation of hydrogen to defects in nickel using first-principles calculations: The case of self-interstitials and cavities. *J. Alloys Compd.* **614**, 211 (2014).

[141] Tanguy, D., Wang, Y. & Connétable, D. Stability of vacancy-hydrogen clusters in nickel from first-principles calculations. *Acta Mater.* **78**, 135 (2014).

[142] Kresse, G. & Furthmüller, J. Efficiency of ab-initio total energy calculations for metals and semiconductors using a plane-wave basis set. *Comput. Mater. Sci.* **6**, 15 (1996).

[143] Kresse, G. & Furthmüller, J. Efficient iterative schemes for ab initio total-energy calculations using a plane-wave basis set. *Physical Reviews B* **54**, 11169 (1996).

[144] Vanderbilt, D. Soft self-consistent pseudopotentials in a generalized eigenvalue formalism. *Phys. Rev. B* **41**, 7892 (1990).

[145] Nørskov, J. K. Covalent effects in the effective-medium theory of chemical binding: Hydrogen heats of solution in the 3d metals. *Phys. Rev. B* **26**, 2875 (1982).

[146] Nordlander, P., Norskov, J. K. & Besenbacher, F. Trends in hydrogen heats of solution and vacancy trapping energies in transition metals. *J. Phys. F: Met. Phys.* **16**, 1161 (1986).

[147] Legrand, E. *et al.* Numerical analysis of the influence of scale effects and microstructure on hydrogen diffusion in polycrystalline aggregates. *Comput. Mater. Sci.* **71**, 1 (2013).

[148] Hoch, B. O., Metsue, A., Bouhattate, J. & Feaugas, X. Effects of grain-boundary networks on the macroscopic diffusivity of hydrogen in polycrystalline materials. *Comput. Mater. Sci.* **97**, 276 (2015).

[149] Arantes, D. R., Huang, X. Y., Marte, C. & Kirchheim, R. Hydrogen diffusion and permeation in micro- and nanocrystalline nickel. *Acta Metall. Mater.* **41**, 3215 (1993).

[150] Brass, A. M. & Chanfreau, A. Accelerated diffusion of hydrogen along grain boundaries in nickel. *Acta Mater.* **44**, 3823 (1996).

[151] Skogsrud, J. & Thaulow, C. (2014). Unpublished.

[152] Angelo, J. E., Moody, N. R. & Baskes, M. I. Trapping of hydrogen to lattice defects in nickel. *Modell. Simul. Mater. Sci. Eng.* **3**, 289 (1995).

[153] Hasson, G., Boos, J. Y., Herbeuval, I., Biscondi, M. & Goux, C. Theoretical and experimental determinations of grain boundary structures and energies: Correlation with various experimental results. *Surf. Sci.* **31**, 115 (1972).

[154] Mütschele, T. & Kirchheim, R. Hydrogen as a probe for the average thickness of a grain boundary. *Scr. Metall.* **21**, 1101 (1987).

[155] Björketun, M. E., Sundell, P. G., Wahnström, G. & Engberg, D. A kinetic Monte Carlo study of proton diffusion in disordered perovskite structured lattices based on first-principles calculations. *Solid State Ion.* **176**, 3035 (2005).

[156] Voter, A. F. Introduction to kinetic Monte Carlo method. In Sickafus, K. E., Kotomin, E. A. & Uberuaga, B. P. (eds.) *Radiation Effects in Solids*, chap. 1 (Springer, 2007).

[157] Chatterjee, A. & Vlachos, D. G. An overview of spatial microscopic and accelerated kinetic Monte Carlo methods. *J. Comput.-Aided Mater. Des.* **14**, 253 (2007).

[158] Gilmer, G. H. & Farrell, H. H. Grain-boundary diffusion in thin films: I. The isolated grain boundary. *J. Appl. Phys.* **47**, 3792 (1976).

[159] Chen, Y. & Schuh, C. A. Geometric considerations for diffusion in polycrystalline solids. *J. Appl. Phys.* **101**, 063524 (2007).

[160] Giannozzi, P. *et al.* QUANTUM ESPRESSO: a modular and open-source software project for quantum simulations of materials. *J. Phys.: Condens. Matter* **21**, 395502 (2009).

[161] Nazarov, R., Hickel, T. & Neugebauer, J. First-principles study of the thermodynamics of hydrogen-vacancy interaction in fcc iron. *Phys. Rev. B* **82**, 224104 (2010).

[162] Lejček, P. *Grain boundary segregation in metals*, vol. 136, chap. 4 (Springer, 2010).

[163] Yamaguchi, M. *et al.* First-principles study on the grain boundary embrittlement of metals by solute segregation: Part II. Metal (Fe, Al, Cu)-hydrogen (H) systems. *Metall. Mater. Trans. A* **42**, 330 (2011).

[164] Zheng, H., Rao, B. K., Khanna, S. N. & Jena, P. Electronic structure and binding energies of hydrogen-decorated vacancies in Ni. *Phys. Rev. B* **55**, 4174 (1997).

[165] Kirchheim, R., Somerday, B. & Sofronis, P. Chemomechanical effects on the separation of interfaces occurring during fracture with emphasis on the hydrogen-iron and hydrogen-nickel system. *Acta Mater.* **99**, 87 (2015).

[166] Hofmann, S. & Lejček, P. Solute segregation at grain boundaries. *Interface Sci.* **3**, 241 (1996).

[167] Song, J. & Curtin, W. A. A nanoscale mechanism of hydrogen embrittlement in metals. *Acta Mater.* **59**, 1557 (2011).

[168] Yamaguchi, M. First-principles study on the grain boundary embrittlement of metals by solute segregation: Part I. iron (Fe)-solute (B, C, P, and S) systems. *Metall. Mater. Trans. A* **42**, 319 (2011).

[169] Tahir, A. M., Janisch, R. & Hartmaier, A. Ab initio calculation of traction separation laws for a grain boundary in molybdenum with segregated C impurites. *Modell. Simul. Mater. Sci. Eng.* **21**, 075005 (2013).

[170] Zhang, Y. *et al.* Weakening of an aluminum grain boundary induced by sulfur segregation: A first-principles computational tensile test. *Phys. Rev. B* **75**, 174101 (2007).

[171] Liu, Y. L., Zhou, H. B. & Zhang, Y. Ideal mechanical properties of vanadium by a first-principles computational tensile test. *J. Nucl. Mater.* **416**, 345 (2011).

[172] Jarvis, E. A. A., Hayes, R. L. & Carter, E. A. Effects of oxidation on the nanoscale mechanisms of crack formation in aluminum. *ChemPhysChem* **2**, 55 (2001).

[173] Janisch, R., Ahmed, N. & Hartmaier, A. Ab initio tensile tests of Al bulk crystals and grain boundaries: Universality of mechanical behavior. *Phys. Rev. B* **81**, 184108 (2010).

[174] Hong, T., Smith, J. R., Srolovitz, D. J., Gay, J. G. & Richter, R. Determining ab initio interfacial energetics. *Phys. Rev. B* **45**, 8775 (1992).

[175] Zhong, L., Wu, R., Freeman, A. J. & Olson, G. B. Charge transfer mechanism of hydrogen-induced intergranular embrittlement of iron. *Phys. Rev. B* **62**, 13938 (2000).

[176] Szost, B. A., Vegter, R. H. & Rivera-Díaz-del Castillo, P. E. J. Hydrogen-trapping mechanisms in nanostructured steels. *Metall. Mater. Trans. A* **44**, 4542 (2013).

[177] Yamasaki, S. & Takahashi, T. Evaluation method of delayed fracture property of high strength steels. *Tetsu-to-Hagané* **83**, 454 (1997).

[178] Wei, F. G. & Tsuzaki, K. Quantitative analysis on hydrogen trapping of TiC particles in steel. *Metall. Mater. Trans. A* **37**, 331 (2006).

[179] Wei, F. G., Hara, T. & Tsuzaki, K. Precise determination of the activation energy for desorption of hydrogen in two Ti-added steels by a single thermal-desorption spectrum. *Metall. Mater. Trans. B* **35**, 587 (2004).

[180] Escobar, D. P., Wallaert, E., Duprez, L., Atrens, A. & Verbeken, K. Thermal desorption spectroscopy study of the interaction of hydrogen with TiC precipitates. *Met. Mater. Int.* **19**, 741 (2013).

[181] Michler, T. & Naumann, J. Microstructural aspects upon hydrogen environment embrittlement of various bcc steels. *Int. J. Hydrogen Energy* **35**, 821 (2010).

[182] Song, E. J., Suh, D.-W. & Bhadeshia, H. K. D. H. Theory for hydrogen desorption in ferritic steel. *Comput. Mater. Sci.* **79**, 36 (2013).

[183] Maroef, I., Olson, D. L., Eberhart, M. & Edwards, G. R. Hydrogen trapping in ferritic steel weld metal. *Int. Mater. Rev.* **47**, 191 (2002).

[184] Pressouyre, G. M. & Bernstein, I. M. A quantitative analysis of hydrogen trapping. *Metall. Trans. A* **9**, 1571 (1978).

[185] De Jong, A. M. & Niemantsverdriet, J. W. Thermal desorption analysis: Comparative test of ten commonly applied procedures. *Surf. Sci.* **233**, 355 (1990).

[186] Fors, D. H. & Wahnström, G. Theoretical study of interface structure and energetics in semicoherent Fe (001)/M X (001) systems (M= Sc, Ti, V, Cr, Zr, Nb, Hf, Ta; X= C or N). *Phys. Rev. B* **82**, 195410 (2010).

[187] Gustafson, Å. Coarsening of TiC in austenitic stainless steel—experiments and simulations in comparison. *Mater. Sci. Eng. A* **287**, 52 (2000).

[188] Wallaert, E., Depover, T., Pieters, B., Arafin, M. A. & Verbeken, K. TDS Evaluation of the Hydrogen Trapping Capacity of NbC Precipitates. In *International Hydrogen Conference (IHC 2012)* (ASME Press, 2014).

[189] Benedek, R. *et al.* First principles simulation of a ceramic/metal interface with misfit. *Phys. Rev. Lett.* **84**, 3362 (2000).

[190] Sawada, H., Taniguchi, S., Kawakami, K. & Ozaki, T. First-principles study of interface structure and energy of Fe/NbC. *Modell. Simul. Mater. Sci. Eng.* **21**, 045012 (2013).

[191] Kresse, G. & Hafner, J. Ab initio molecular dynamics for liquid metals. *Phys. Rev. B* **47**, 558 (1993).

[192] Ding, H. *et al.* First-principles study of hydrogen storage in non-stoichiometric TiCx. *J. Alloys Compd.* **551**, 67 (2013).

[193] Porter, D. A. & Easterling, K. E. *Phase Transformation in Metals and Alloys*, chap. 3 (Chapman & Hall, 1992).

[194] Goretzki, H. Neutron Diffraction Studies on Titanium-Carbon and Zirconium-Carbon Alloys. *Phys. Status Solidi B* **20**, K141 (1967).

[195] Pierson, H. O. *Handbook of Refractory Carbides & Nitrides: Properties, Characteristics, Processing and Applications* (William Andrew, 1996).

[196] Xiang, J. *et al.* Spark plasma sintering of the nonstoichiometric ultrafine-grained titanium carbides with nano superstructural domains of the ordered carbon vacancies. *Mater. Chem. Phys.* **130**, 352 (2011).

[197] Kawakami, K. & Matsumiya, T. Numerical analysis of hydrogen trap state by TiC and V4C3 in bcc-Fe. *ISIJ Int.* **52**, 1693 (2012).

[198] Benedek, R., Seidman, D. N. & Woodward, C. The effect of misfit on heterophase interface energies. *J. Phys.: Condens. Matter* **14**, 2877 (2002).

[199] Albina, J. M., Mrovec, M., Meyer, B. & Elsässer, C. A study of the semi-coherent ceramic $SrTiO_3/SrZrO_3$ interface by first-principles DFT calculations. In Gumbsch, P. (ed.) *Proc. Int. Conf. MMM 2006*, 819 (Fraunhofer IRB Verlag, 2006).

[200] Sampath, S. & Janisch, R. Ab initio prediction of the critical thickness of a precipitate. *J. Phys.: Condens. Matter* **25**, 355005 (2013).

[201] Takahashi, J., Kawakami, K. & Tarui, T. Direct observation of hydrogen-trapping sites in vanadium carbide precipitation steel by atom probe tomography. *Scr. Mater.* **67**, 213 (2012).

[202] Lee, H. G. & Lee, J.-Y. Hydrogen trapping by TiC particles in iron. *Acta Metall.* **32**, 131 (1984).

[203] Itakura, M., Kaburaki, H., Yamaguchi, M. & Okita, T. The effect of hydrogen atoms on the screw dislocation mobility in bcc iron: A first-principles study. *Acta Mater.* **61**, 6857 (2013).

[204] Kimizuka, H. & Ogata, S. Slow diffusion of hydrogen at a screw dislocation core in α-iron. *Phys. Rev. B* **84**, 024116 (2011).